Chair of Automation

Master's Thesis

Towards Continuous Railway Monitoring: A Concept for Surface Crack Assessment Based on Surface Acoustic Waves

Sebastian Fichtenbauer, BSc

October 2023

MONTANUNIVERSITÄT LEOBEN
www.unileoben.ac.at

EIDESSTATTLICHE ERKLÄRUNG

Ich erkläre an Eides statt, dass ich diese Arbeit selbständig verfasst, andere als die angegebenen Quellen und Hilfsmittel nicht benutzt, und mich auch sonst keiner unerlaubten Hilfsmittel bedient habe.

Ich erkläre, dass ich die Richtlinien des Senats der Montanuniversität Leoben zu "Gute wissenschaftliche Praxis" gelesen, verstanden und befolgt habe.

Weiters erkläre ich, dass die elektronische und gedruckte Version der eingereichten wissenschaftlichen Abschlussarbeit formal und inhaltlich identisch sind.

Datum 25.10.2023

Sebastian Fichtenbauer

Unterschrift Verfasser/in
Sebastian Fichtenbauer

Dedication

First and foremost, I would like to express my gratitude to Prof. Paul O'Leary for supervising this thesis and for the invaluable insights he shared during our numerous discussions.

I am deeply grateful to the *Materials Center Leoben Forschung GmbH* for offering me the opportunity to undertake this thesis. My profound thanks go to Hans-Peter Gänser for his mentoring and guidance. I truly appreciate his steady support. I also owe a debt of thanks to Mohsen Rezaei and Sven Eck for their precious advice, and to Verena Beckmann and Maximilian Pfeiffer for their diligent assistance with the preparation of the laboratory experiments.

Special acknowledgment goes to *voestalpine Railway Systems GmbH*, and especially to David Künstner, for supplying the rail specimens. My appreciation also goes to Christoph Tuschl from the Chair of Automation, who supported this thesis by characterizing the specimens through thermography.

I cannot thank my parents enough for their unwavering encouragement throughout my studies. Lastly, but by no means least, my gratitude extends to my friends, colleagues, and my girlfriend Karoline for motivating me during challenging times. Their companionship has made my time in Leoben truly memorable.

Acknowledgement:
The author gratefully acknowledges the financial support under the scope of the COMET program within the K2 Center "Integrated Computational Material, Process and Product Engineering (IC-MPPE)" (Project No 886385). This program is supported by the Austrian Federal Ministries for Climate Action, Environment, Energy, Mobility, Innovation and Technology (BMK) and for Labour and Economy (BMAW), represented by the Austrian Research Promotion Agency (FFG), and the federal states of Styria, Upper Austria and Tyrol.

Kurzfassung

Diese Masterarbeit verfolgt einen experimentellen Ansatz, um ein auf akustischen Oberflächenwellen basierendes Sensorkonzept zur Tiefenmessung von Oberflächenrissen zu evaluieren. Der Fokus der vorliegenden Arbeit liegt hierbei auf einer möglichen Anwendung zur Überwachung von Rissen in Schienen. Aktuell ist kein Messverfahren bekannt, das sowohl die Risstiefe sogenannter Head Checks an der Fahrkante der Schiene genau erfassen kann als auch eine permanente Installation der notwendigen Messausrüstung erlaubt. Eine solche Methode verspricht, einen wesentlichen Beitrag zur kontinuierlichen Zustandsüberwachung von Eisenbahninfrastruktur zu leisten und somit zu einem sicheren und kosteneffizienten Betrieb von Schienennetzen beizutragen. Das Hauptziel dieser Masterarbeit besteht darin, zu analysieren, ob die Risstiefe von Head Checks mit akustischen Oberflächenwellen quantitativ bestimmt werden kann. Hierfür wurde der Transmissionskoeffizient als Schlüsselcharakteristikum zur Bewertung der Risstiefe ausgewählt.

Im Rahmen dieser Masterarbeit wurde ein Messaufbau zur experimentellen Bestimmung des Transmissionskoeffizienten entworfen, mit dem Schienenproben mit verschiedenen Head Check Tiefen untersucht wurden. An die Schienenproben angebrachte piezoelektrische Transducer wurden zum Anregen der akustischen Oberflächenwellen verwendet. Ein Laser-Doppler-Vibrometer wurde eingesetzt, um die dadurch hervorgerufenen Schwingungen der Bauteiloberfläche zu messen. Es wurden repräsentative Messsignale im Zeit- und Frequenzbereich analysiert sowie ein Algorithmus entwickelt und implementiert, der zur Extraktion der Amplitude von einfallender und übertragener Oberflächenwelle dient. Basierend auf diesen Werten konnten die Transmissionskoeffizienten berechnet werden. Schließlich konnte durch die hohe Anzahl an durchgeführten Messungen die Bestimmungsgenauigkeit der Transmissionskoeffizienten bewertet werden.

Anhand der erzielten Resultate lässt sich, unter der Voraussetzung von geringer Tiefe der Head Checks und hoher Anregungsfrequenz der akustischen Oberflächenwellen, ein linearer Zusammenhang zwischen Risstiefe und Transmissionskoeffizienten vermuten. Daher erscheint unter diesen Umständen eine Risstiefenbestimmung mit dem Transmissionskoeffizienten machbar. Zusätzlich wurden mögliche Gründe identifiziert, die eine quantitative Bewertung tiefer Head Checks erschweren. Im Hinblick auf eine mögliche Anwendung des evaluierten Sensorkonzepts im Gleis sind jedoch zahlreiche Fragestellungen bezüglich der rauen Umgebungsbedingungen noch zu klären.

Abstract

This master's thesis employs an experimental approach to evaluate the feasibility of a surface acoustic wave (SAW) based monitoring concept for depth assessment of surface cracks. The focus of this work is on a potential application for monitoring of rail cracks. To date, no measurement principle has been found that offers both precise sizing of gauge corner cracks in rails, commonly termed head checks, and compatibility with permanent rail installation. Such a technique holds the potential to be the key to continuous in-situ condition monitoring of railway infrastructure, ensuring a cost-efficient, yet safe operation of rail tracks. The primary objective of this thesis is to determine if surface acoustic waves can be used for a quantitative assessment of head check depth. The SAW transmission coefficient was selected as the representative wave feature for crack examination.

Rail samples that exhibit varying degrees of head check damage were collected. An experimental setup was established to determine the SAW transmission coefficient for different crack depths. A Laser Doppler vibrometer was used to measure the out-of-plane displacement of the propagating SAWs, which were excited by piezoelectric transducers affixed to the rail specimens. Characteristic measurement signals were analyzed in both time and frequency domains. A signal processing algorithm was developed and implemented to extract the amplitudes of the incident and transmitted SAW. Subsequently, the transmission coefficients were calculated from these values. The extensive number of measurements allowed for an evaluation of the statistical scatter of the obtained transmission coefficients.

Based on the obtained results, a linear correlation between head check depth and transmission coefficient is hypothesized for low crack depth and high-frequency surface acoustic waves. Consequently, sizing head checks using the SAW transmission coefficient is deemed potentially feasible under these specific conditions. Moreover, mechanisms impeding a quantitative assessment of deeper head checks have been identified. To apply the evaluated sensor concept in railway tracks, many challenges still need to be overcome, given the prevailing harsh environment.

Contents

Chapter 1
Introduction

This thesis employs an experimental approach to evaluate a sensor concept based on surface acoustic waves for condition monitoring of cracks. Features extracted from measurement signals are correlated with the depth of rail surface cracks.

1.1 Motivation

In recent decades, rails have seen escalating demands due to faster passenger trains and freight trains with higher axle loads. These increased loads have resulted in the formation of previously unseen types of damage on standard rail grades. Among them, especially the so-called head checks cause major concern to railway network operators worldwide. When not detected and removed on time, these surface cracks can even lead to derailment and thereby to devastating accidents, such as the infamous Hatfield rail crash [1, 2]. Therefore, track operators are faced with a decision: either to routinely inspect rails using instrumented vehicles or to adopt a preventive maintenance approach through grinding the rails at regular intervals [2, 3]. In practice, this can lead to the grinding of undamaged rails, given the challenges of predicting crack growth rates [4]. In contrast, condition-based maintenance, which is enabled by continuous condition monitoring of railway assets, offers the dual benefit of reducing downtime and extending asset lifetime, since maintenance actions are executed only as needed. Such targeted monitoring paves the way for efficient maintenance planning and reduces the number of necessary inspections dramatically, leading to potential cost savings [3].

However, many of the relevant parameters in railway condition monitoring cannot be measured directly. This is often due to high equipment costs or the lack of suitable technology [5]. While wayside condition monitoring provides significant advantages by not obstructing the track during the rail inspection process, it is challenging because a permanent installation of the sensing equipment is necessary. In fact, given the complex crack configuration of head checks, no crack monitoring setup that offers both precise sizing and compatibility with permanent rail installation has been found to date.

Nonetheless, surface acoustic waves (SAWs), which belong to the class of ultrasonic testing methods, have recently emerged as an auspicious technique for detecting surface defects. This is because of their propagation characteristics on a structure's surface. They also facilitate the analysis of components with complex geometries. Yichao presents in [6] a concept for assessing rail head surface cracks by means of SAWs. However, the described measurement equipment has to be removed from the rail after the measurement, since the wave generating electromagnetic acoustic transducer (EMAT) is positioned directly on the rail head. Gruber et al. found a qualitative influence of head check damage on the SAW transmission coefficient [3]. Yet, the comb transducers they used are not suitable for a permanent installation. A detailed review of the state-of-the-art in railway condition monitoring is provided in Section 2.3. Moreover, surface acoustic waves also hold promise in detecting and monitoring cracks in other safety-critical engineering components. Previous studies have already examined this technique's capability to gauge crack depths in integral parts of aircraft [7] or in turbine rotors [8, 9].

The primary contribution of this thesis is to evaluate whether a specific feature, namely the SAW transmission coefficient, can be exploited for a quantitative assessment of cracks on the surfaces of geometrically complex components. An experimental approach was taken by investigating six different rail samples with varying crack depths. Measurements were conducted on these rail specimens, simulating a potential permanent sensor installation on actual rails. A signal processing routine was developed to derive the wave amplitudes and, subsequently, the transmission coefficient from the acquired data.

1.2 Structure of the Thesis

As this thesis predominantly adopts an experimental approach, the emphasis is placed on the experimental work. Nevertheless, for the benefit of all readers, the initial chapters discuss fundamental concepts to ensure a basic understanding before delving into the application.

This introduction is followed by a review of the current state-of-the-art in railway condition monitoring. It also outlines prevalent rail damage types and highlights selected non-destructive testing methodologies.

In Chapter 3, the reader is introduced to the fundamental physics of surface acoustic waves, also termed quasi-Rayleigh waves. This chapter closes with a literature-based identification of the most promising wave feature for crack assessment.

Selected signal processing concepts are provided in Chapter 4. In contrast, Chapter 5 focuses on the practical application of signal processing techniques on captured measurement data. The

latter section of this chapter showcases the developed signal processing algorithm, which was implemented in the *Python* programming language.

Chapter 6 begins with an introduction to the laboratory measurement equipment. To eliminate potential biases caused by the used instruments, preliminary measurements were executed. In addition, the wave propagation speed and attenuation over distance were investigated. The design and evaluation of these experiments are detailed.

In Chapter 7, the focus shifts to measurements carried out on the provided rail samples with different crack depths. A rigorous analysis of data obtained from these tests is presented, accompanied by an in-depth description of the experimental setup. Additionally, a comprehensive discussion on the acquired results is undertaken.

Finally, the concluding Chapter 8 synthesizes the key findings and suggests possible directions for forthcoming research in this domain.

Chapter 2
State-of-the-art

This chapter begins with a brief introduction to the most relevant rail damage types. In particular, the damage type of rolling contact fatigue (RCF) is described. Additionally, common techniques for non-destructive evaluation of rail damage are detailed. Finally, an overview of state-of-the-art technologies for railway condition monitoring is provided.

2.1 Types of Rail Damage

In general, the endurance of a rail is primarily determined by three effects: defects, wear, and plastic flow [10]. Although defects can initiate and propagate in a rail for various reasons, the most common cause for cracks in the rail head is rolling contact fatigue (RCF). RCF can manifest in different damage patterns, including head checks and squats. The occurrence of a specific damage pattern depends on the loading conditions and track geometry. In curved tracks, rolling contact fatigue typically leads to surface breaking cracks on the rail's gauge corner. A schematic illustration of these cracks, which are termed head checks, is given in Figure 2.1(a). Head checks are considered as the biggest issue in modern rails [1]. As uncontrolled growth of head checks can eventually result in rail breakage, it is crucial to detect and remove them in time [10]. Brief descriptions of the damage patterns of head checks and squats are provided in the following subsections.

Wear refers to the removal or displacement of material from the rail's running surface due to wheel contact [1]. Although this type of degradation is observed on all rails, in particular sharp curves lead to a higher wear rate because of increased contact forces [10]. Figure 2.1(b) depicts cross-sections of both a new and a worn rail. Wear itself might not directly result in failure. Still, it does contribute to increased contact forces and poor dynamics, which can accelerate crack growth from other rail damage mechanisms [1]. In extreme cases, it can even diminish the rail's stiffness. Another consequence of wear is the development of periodic irregularities on the rail head, referred to as rail corrugations [2]. To reduce wear, harder and, thereby, more wear-resistant rail grades are gaining popularity [1].

A special relationship exists between rail wear and head check growth. While the head checks are growing deeper, wear simultaneously strips material from the rail head. Consequently, this leads to a reduced crack propagation rate compared to a hypothetical scenario without any wear. If the material removal rate is higher than the crack propagation rate, cracks cannot grow at all. Consequently, modern rail grades with increased wear resistance tend to be more susceptible to RCF damage [1].

Plastic flow occurs if the contact stresses exceed the yield strength of the rail material [10]. Therefore, the running band on the rail head is affected and ultimately rail corrugations can develop. However, due to the higher hardness of modern rail grades, plastic flow no longer poses a challenge for track operators [1]. In addition to the most grave types of rail damage introduced in this section, other types of rail defects are also observed [10].

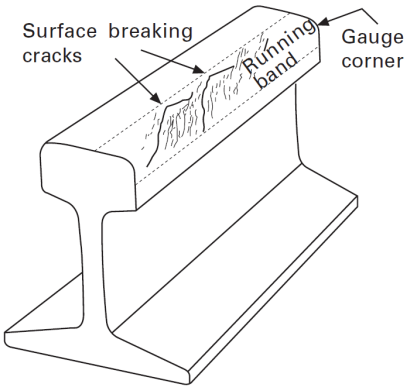

(a) Schematic representation of head checks. These are surface breaking cracks on the rail's gauge corner. Adapted from [1].

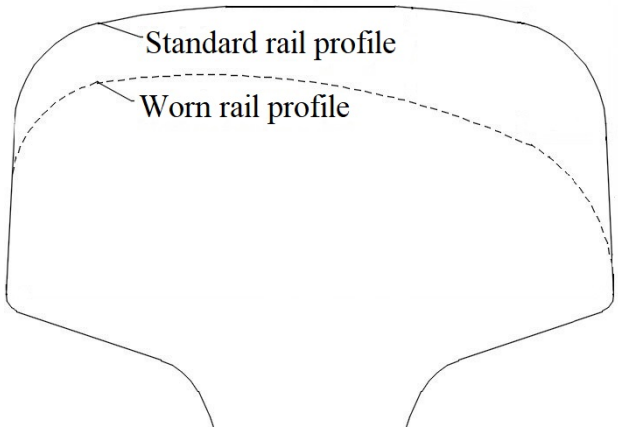

(b) Schematic representation of cross-sections from a new rail and from a rail with vertical and lateral wear. Adapted from [11].

Fig. 2.1: Illustration of selected types of rail damage.

2.1.1 Head Checks

Head checks emerge due to repeated plastic deformation in the rail material. As highlighted in Figure 2.1(a), head checks appear on the outer rail's gauge corner. This is why they are sometimes referred to as gauge corner cracks (GCC). Typically, they evolve in networks and form a continuous head check band [1, 4]. This type of RCF is particularly prevalent in the curved sections, where the wheel contacts the gauge corner of the curve's external rail [12]. This results in a reduction of

wheel/rail contact area. Additionally, in such sections, the lateral force interacts with the longitudinal friction force caused by the train's drive mechanism [4].

Head check growth can be subdivided into three phases. During the first phase, the cracks initiate on the rail head surface. In the following phase, head checks grow at a constant rate under a shallow angle α to the rail surface. After eventually reaching a certain depth, the third phase begins which is characterized by a fast crack growth and a change in the propagation direction. The cracks start to form vertical or horizontal branches [1, 4]. Figure 2.2 gives a schematic illustration of a head check and depicts its geometric parameters. The depth a of a head check is defined as the normal distance between the crack tip and the rail surface.

From a theoretical viewpoint, the crack propagation rate can be calculated based on traffic load, rail grade, curve radius, and wheel/rail profile pairing. However, track operators often do not have access to some of these parameters, such as the wheel/rail profile pairing. Indeed, empirically found head check depths show a substantial deviation from calculated values [4]. As a result, models for predicting head check depth exhibit significant uncertainty. Preventive maintenance action plans are fundamentally influenced by the highest observed crack initiation and propagation rates. Therefore, following a preventive maintenance strategy results in grinding many undamaged rails.

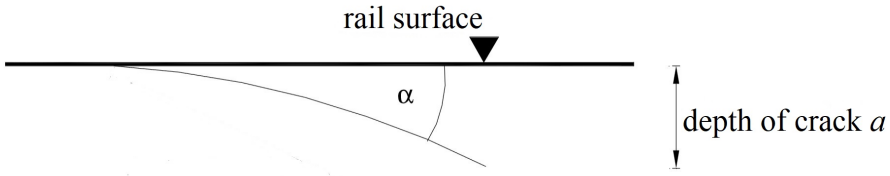

Fig. 2.2: Schematic illustration of a head check and its crack depth a. The depth of a head check is defined as the normal distance between the crack tip and the rail surface. Adapted from [12].

Since head checks typically appear in a continuous band, monitoring selected cross-sections located at predefined hotspots should, in theory, be sufficient to assess the condition of the entire curve. However, sizing the depth of head checks remains a challenging task due to the narrow spacing between cracks. After reaching a certain length, head checks can overlap.

2.1.2 Squats

In contrast to head checks, squats develop on the top of the rail head, where they appear as dark spots. Typically they emerge on tangent tracks or in heat-affected zones close to welded rail joints [13]. Squats either originate from pre-existing head checks or initiate from so-called white etch-

ing layers on the rail head's surface. These layers are hard and brittle and can easily be removed by grinding or milling the affected surface layer [10]. In the initial phase, squats grow at a narrow angle to the surface. After reaching a certain depth, they eventually change their direction of propagation and begin to grow towards the inside of the rail [2].

While squats seldom lead to rail breakage compared to other rail damage types, they are a significant driver for maintenance costs. This is because regular rail grinding or milling is essential to prevent their emergence [2].

2.2 Non-Destructive Testing Techniques for Rails

In general, non-destructive testing techniques are applied before putting safety-relevant structural parts into service or during periodic inspections of these components. Their aim is to detect faults inside a component or on its surface. According to Bargel and Schulze [14], non-destructive testing techniques can be categorized into:

- visual testing;
- electromagnetic testing;
- ultrasonic testing;
- radiographic testing.

However, additional methods for the non-destructive evaluation of materials and structures exist, with some of them currently receiving a lot of scientific attention [13, 15]:

- acoustic emission testing;
- infrared thermography;
- magnetic testing;
- testing using fibre optic sensors.

Recent research highlights the potential of acoustic emission testing [13, 16] and infrared thermography [17] for assessing rail surface cracks. Nonetheless, for years eddy current testing, which belongs to the group of electromagnetic methods, has been successfully applied to detect and characterize flaws in rails [1, 12]. Besides eddy current technology, conventional ultrasonic methods are crucial to verify potential faults [4, 18]. The following subsections provide detailed descriptions of ultrasonic and eddy current testing. A measurement setup for online condition monitoring needs to be suitable for permanent installation. Therefore, it must be emphasized that the standard measurement devices for both conventional ultrasonic testing and eddy current testing do not fulfill this requirement.

2.2.1 Ultrasonic Testing

In conventional ultrasonic testing, two primary methods exist: the pulse-echo method and the pitch-catch method. For the pulse-echo method, only one probe is needed. Typically placed on the workpiece's upper surface, this probe sends ultrasonic pulses and receives reflections from the lower surface or potential flaws. Due to the difference in the time-of-flight, reflections caused by flaws can be distinguished from surface reflections. As ultrasonic waves cannot propagate in air, a liquid couplant is usually used to ensure that the transducer excites ultrasonic waves in the specimen [9, 19].

The pulse-echo method is illustrated for a flawless workpiece and for a workpiece containing a flaw in Figure 2.3(a) and Figure 2.3(b), respectively. In the case of the flawless specimen, its wall thickness can be determined from the transit time of the ultrasonic pulse. As Figure 2.3(b) suggests, the orientation of the flaw is crucial for the intensity of the wave's back-scattering. However, by exciting the ultrasonic wave in a direction that is not perpendicular to the surface, vertical defects can also be detected [19].

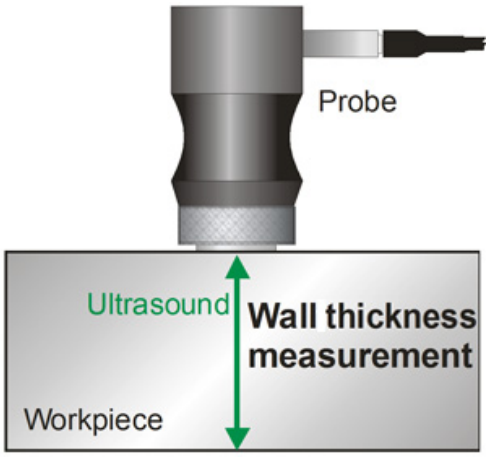

(a) Ultrasonic testing of a flawless workpiece: The ultrasonic wave is reflected at the specimen's lower surface. The wall thickness can be determined from the time-of-flight [20].

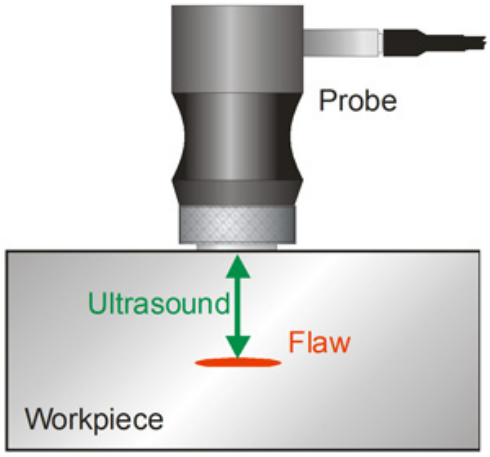

(b) Ultrasonic testing of a workpiece with a flaw: The ultrasonic wave is reflected by the flaw, leading to a shorter time-of-flight compared to the flawless specimen [20].

Fig. 2.3: Pulse-echo method in conventional ultrasonic testing.

In contrast to the pulse-echo setup, the pitch-catch method relies on two transducers. One transducer is placed on the upper surface and the other one is positioned on the lower surface of the specimen. Although the pitch-catch mode facilitates testing of materials with low sound conductivity, it has many disadvantages compared to the pulse-echo setup. For instance, with a pulse-echo setup the actual depth of a flaw can be calculated. Additionally, pulse-echo is more sensitive to small defects. Therefore the pulse-echo setup is preferred in practice [19].

When conventional ultrasonic methods are applied to gauge rail defects, a minimum vertical depth of the defect $a = 3\,\text{mm}$ is required for reliable detection [13]. In contrast to conventional ultrasonic testing, which employs ultrasonic bulk waves, the measurement concept evaluated in this thesis is based on ultrasonic surface waves. These surface acoustic waves (SAWs) allow for an earlier detection of cracks, as the wave's energy is concentrated in the near-surface area. In addition, a SAW can propagate along a curved surface if the curve radius is significantly larger than the wavelength. Moreover, ultrasonic surface waves can also propagate over sharp edges without a phase jump of $\lambda/2$ and without conversion to another wave mode. Still, a smooth surface is a prerequisite for employing SAW measurements [9].

2.2.2 Eddy Current Testing

Eddy current testing is based on the physical phenomenon of electromagnetic induction and can be employed when testing conductive materials. The working principle of this non-destructive testing technique is highlighted in Figure 2.4. A primary coil is driven by an alternating current, which generates a magnetic field. Due to this magnetic field, eddy currents are induced in the close-by specimen and lead to a secondary magnetic field. This secondary magnetic field superposes with the initial magnetic field. The resulting magnetic flux can either be measured with a second coil or with the primary coil by continuously switching between excitation and receive modes. If eddy currents encounter a defect in the specimen, the secondary magnetic field is affected. A change in amplitude or phase of the magnetic field is detected with the measurement equipment and used for a qualitative defect assessment [13].

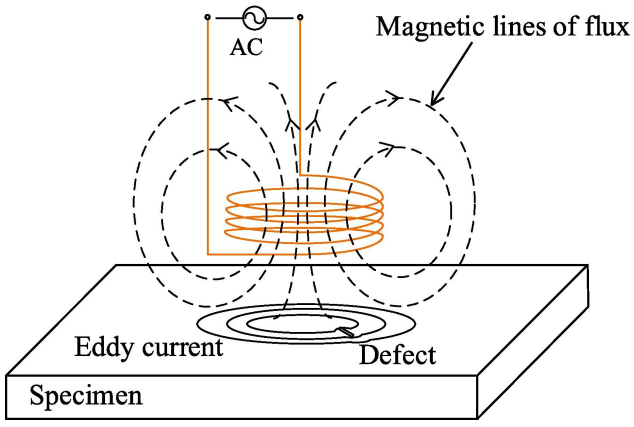

Fig. 2.4: Working principle of eddy current testing. An alternating current in the coil generates a magnetic field. Eddy currents are induced in the specimen by this field and lead to a secondary magnetic field. Defects affect the induced eddy currents [18].

In contrast to conventional ultrasonic testing, the probe does not need to be in contact with the specimen. This allows for an increased inspection speed [13, 18]. Although eddy current testing is

considered to be capable of detecting surface and near-surface flaws [15], a quantitative assessment of the crack depth is hard to obtain. In particular, sizing closely spaced cracks, such as head checks, with high crack depth is a challenging task, leading to an inaccurate measurement of crack depth [13, 19].

Eddy current testing can be carried out manually or automatically. For automatic inspection, typically special measurement trains are used. Nevertheless, also maintenance trains can be instrumented with the corresponding equipment to monitor the grinding process [12].

2.3 State-of-the-art in Condition Monitoring of Railways

In railway condition monitoring, track operators have to choose between two primary approaches: either they deploy instrumented vehicles that routinely survey the entire track network or they install measurement devices at specific spots known to be susceptible to rail damage. This stationary method is often termed wayside condition monitoring [3]. While track operators seek faster inspection methods [16], wayside condition monitoring offers the significant advantage of not obstructing the track during the rail inspection process.

Most condition monitoring applications in the railway industry face the challenge that many parameters cannot be measured directly. This can be due to different reasons, like high implementation costs or the absence of adequate technology [5]. However, Lewis and Olofsson introduce wayside condition monitoring concepts in [1] that were implemented on US railroads as early as 2009. These methods primarily target the detection of damaged wheels. Techniques for monitoring rails are not mentioned. Still, they emphasize that in the future rail condition measurements will aid in the planning of preventive maintenance schedules.

Ngini et al. [5] provide an overview of various concepts for monitoring the structural integrity of rolling stock with track-based sensors. For instance, wheel defects can be detected by measuring the force, which is exerted by the wheel on the rail. Additionally, concepts for identifying track irregularities, for example in the track cross level, with vehicle-based equipment are presented [5]. Recent research underlines the potential of acoustic emission testing for online monitoring of both rolling stock [21] and rails [6, 13]. However, this concept is very prone to unwanted noise. Therefore, sophisticated signal processing algorithms are needed to retrieve reliable information about the asset's condition [13]. In contrast, it has already been demonstrated that ultrasonic surface waves can be used to detect the presence of head checks in rails [3, 6]. Yet, no published studies have confirmed the capability of a wayside condition monitoring concept to quantitatively evaluate head check depth.

Most commercially available track monitoring systems are vehicle-based. The company *Plasser und Theurer*, for example, offers measurement trains with optical or mechanical systems to quantify track gauge and inspect track geometry [22]. Enterprises such as *Vossloh* and *RailMeasurement* produce cars and trolleys which exploit visual techniques to assess the wear of the rail profile [23, 24]. Additionally, these vehicles use eddy current testing to characterize surface defects and in case of *Vossloh* even conventional ultrasonic testing to detect flaws inside the rail.

In contrast, *D-RAIL* presents a sensor system adaptable to any train. They assert that their instruments can detect cyclic faults and even RCF damage. While they have not specified the sensor type, it is inferred that their system primarily uses acceleration data, as the sensors are mounted to structural components of bogies. These acceleration measurements are combined with an accurate GPS-based positioning system [25].

The Austrian firm *voestalpine Railway Systems* provides monitoring technologies for both rolling stock and for railway infrastructure. Their portfolio includes systems to monitor switches and capture environmental data. The required sensors are installed permanently [26].

Chapter 3
Introduction to Ultrasonic Rayleigh Waves

This chapter provides an introduction to the fundamental physics of Rayleigh waves, covering wave velocity and propagation mechanisms. The decay of the Rayleigh wave amplitude is then theoretically derived as a function of the distance from the wave-exciting transducer. Additionally, a review of various ultrasonic wave characteristics for fault detection is given, and the selection of the transmission coefficient as the characteristic wave feature is discussed.

3.1 The Physics of Rayleigh Waves

In solid materials, two types of bulk waves can propagate: longitudinal (pressure) waves and transversal (shear) waves [27]. These modes of wave propagation are typically utilized in conventional ultrasonic testing methods [9]. However, under specific circumstances, surface wave modes such as Rayleigh waves [6] can also exist. These surface acoustic waves (SAWs) offer a special potential for the surface inspection of structural components, as the wave's energy is concentrated in the near-surface area [6, 9]. Several pieces of literature, for instance [27, 28, 29], demonstrate the derivation of the Rayleigh wave equations by the method of potentials, assuming a plane wave and an isotropic medium. While strictly speaking, the Rayleigh wave equations are only valid for an ideal half-space with infinite thickness, quasi-Rayleigh waves can still propagate on a mechanical component's surface as long as the wavelength λ_R is significantly smaller than the thickness t of the component, $\lambda_R \ll t$ [3]. The Rayleigh wave velocity v_R is only dependent on the material properties, including the Poisson's ratio μ, the shear modulus, and the density. It can be calculated using the following equation introduced in [27, 28, 29]:

$$\eta^6 - 8\eta^4 + 8\eta^2(3 - 2\xi^2) + 16(\xi^2 - 1) = 0, \tag{3.1}$$

whereby the dimensionless variables η and ξ have been introduced:

$$\eta = \frac{v_R}{v_T}; \qquad \xi = \frac{v_T}{v_L} = \sqrt{\frac{1 - 2\mu}{2(1 - \mu)}}. \tag{3.2}$$

v_T and v_L denote the velocities of the transversal and longitudinal waves in the examined material, respectively. It can be shown that Equation 3.1 has only one root, since μ only varies in the range from 0 to 0.5 for any real solid material [28]. An approximation of this root is given by [28]:

$$\eta = \frac{0.87 + 1.12\mu}{1 + \mu}. \tag{3.3}$$

An estimation of the Rayleigh wave velocity v_R based on Equation 3.2 and Equation 3.3 yields $v_R = 2991\,\mathrm{m/s}$, with the literature values of $\mu = 0.29$ and $v_T = 3230\,\mathrm{m/s}$ given in [3] and [27], respectively. Moreover, Rayleigh waves are nondispersive, as their velocity is not a function of the acoustic wave's frequency [27].

It can be shown that a Rayleigh wave is basically a linear combination of a pressure and a shear wave [29]. Therefore, a Rayleigh wave propagates by material particles oscillating concurrently in longitudinal and transversal directions. Consequently, a certain particle follows an elliptical motion [27, 28, 29]. The propagation of a plane Rayleigh wave is schematically illustrated in Figure 3.1.

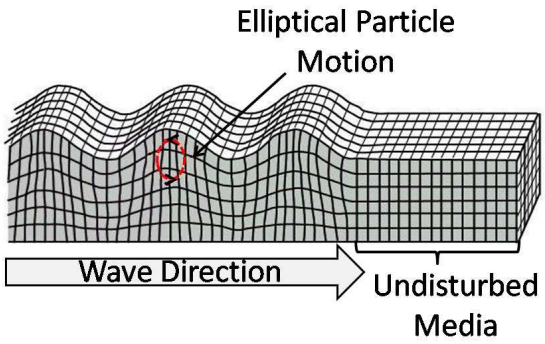

Fig. 3.1: Schematic illustration of the propagation of a plane Rayleigh wave. Material particles follow an elliptical motion as they oscillate in in-plane and in out-of-plane direction [30].

Furthermore, certain texts demonstrate [28, 29] that for a Rayleigh wave propagating in an ideal half-space, the ratio of the in-plane displacement u to the out-of-plane displacement w of a particle u/w at a specific depth is solely dependent on the Poisson's ratio μ of the material. As there is a fixed ratio u/w for a plane surface, the amplitude of the out-of-plane displacement is adequate to determine the amplitude of the SAW. During the experiments conducted in this thesis, presented in Chapters 6 and 7, a Laser Doppler vibrometer (LDV) was used to measure the out-of-plane displacement of the surface caused by the propagating SAW. It is important to note that the ratio u/w may be affected by curved surface geometry. Hence, during the conducted experiments, the SAW amplitude is measured at the plane surfaces of the rail head, maintaining a specific minimum distance from the rail head edges.

3.2 Attenuation of Surface Acoustic Waves

The amplitude of any wave excited by a point source gets attenuated due to purely geometrical reasons, as the wave beam diverges with increasing geometrical distance d from this source. The geometrical amplitude decay of a Rayleigh wave propagating at a plane surface is proportional to $1/\sqrt{k_R d}$, where k_R denotes the wave number of the Rayleigh wave [27, 28]. In contrast to bulk waves, which decay with $1/k_{l,t}d$, the geometrical attenuation of SAWs is lower. k_l and k_t represent the wave numbers of the longitudinal and transversal waves, respectively. This lower geometrical decay enables a measurement over larger distance ranges [9, 28]. The purely geometrical attenuation of a SAW's amplitude $A_G(d)$ can be formalized as a function of distance by

$$A_G(d) = A_{G0}\frac{1}{\sqrt{k_R d}}. \tag{3.4}$$

The constant A_{G0} is computed from the amplitude $A_G(d)$ at a certain position d. It has to be emphasized that Equation 3.4 is only a reasonable model for $d \gg 0$, since a function $f(x)$ of type $f(x) = 1/x \to \infty$ if its argument $x \to 0^+$.

In addition to the geometrical decay, SAWs propagating in steels are attenuated due to physical reasons such as internal absorption or scattering at grain boundaries [9, 28]. As with ultrasonic longitudinal and transversal waves, the sound pressure $P(d)$ of a Rayleigh wave follows an exponential function, when assuming a plane wave that is attenuated through scattering and absorption [9]:

$$P(d) = P_0 \mathrm{e}^{-\alpha d}. \tag{3.5}$$

P_0 denotes the sound pressure of the incident SAW. The attenuation coefficient α can be split into the attenuation coefficient due to absorption α_a and the attenuation coefficient due to scattering α_s: $\alpha = \alpha_a + \alpha_s$. However, for a SAW propagating at the surface of a steel component, the attenuation due to scattering can be neglected if the size of the grains is much smaller than the wavelength of the ultrasonic wave [9]. The examined rail grades satisfy this criterion. The attenuation coefficient due to absorption α_a increases linearly with the excitation frequency of the ultrasonic wave f_x [9]. Since the displacement amplitude $A(d)$ is proportional to $P(d)$ for a specific combination of material and f_x, Equation 3.5 can be rewritten to

$$A_S(d) = A_{S0}\mathrm{e}^{-\alpha d}, \tag{3.6}$$

where A_{S0} denotes the amplitude of the incident SAW. Combining the geometrical decay with the attenuation due to absorption and scattering yields

$$A(d) = A_0\frac{\mathrm{e}^{-\alpha d}}{\sqrt{k_R d}}. \tag{3.7}$$

The final model function for the attenuation of a SAW is obtained by aggregating all constant factors into a single constant C. Consequently, Equation 3.7 results in

$$A(d) = C\frac{\mathrm{e}^{-\alpha d}}{\sqrt{d}}. \tag{3.8}$$

This function is used in Section 6.3 for fitting the attenuation curves.

3.3 Evaluation of Wave Features for Crack Assessment

After the propagation over an open crack, the transmitted SAW still maintains a significant part of the incident wave's energy. However, the crack also causes reflections and mode conversions, which lead to the generation of bulk waves [31]. Besides the loss of energy due to reflection and mode conversion, the transmitted surface wave is also affected in various other ways, depending on the actual configuration of the crack. In previous research, different surface wave features have already been exploited for the assessment of surface defects. Fundamentally, it has to be differentiated between linear and non-linear wave attributes. While linear wave attributes are typically used for the characterization of macro-scale defects, non-linear features are promising for assessing early grades of degradation and micro-scale defects [32, 33, 34].

3.3.1 Linear Wave Features

The most frequently exploited linear wave features for the evaluation of an open structural crack include the transmission and reflection coefficients, the degree of mode conversion, and the delay in the time-of-flight (TOF) [32]. The transmission coefficient C_T is defined as the ratio of the transmitted wave's amplitude to the incident wave's amplitude [28, 35]. Its theoretical trend over the depth d of an open crack normalized by the wavelength of the Rayleigh wave λ_R is depicted in Figure 3.2(a). The transmission coefficients for different angles of incidence between the propagation direction of the SAW and the crack are provided. In any case, the transmission coefficient C_T exhibits an almost linear and monotonic decrease until $a/\lambda_R \approx 0.3$. Consequently, C_T is a bijective function of a/λ for $a/\lambda < 0.3$. Therefore, the transmission coefficient promises a unique and precise determination of the crack depth up to this threshold. Although the coupling conditions may have an impact on the recorded amplitudes [6], this issue is considered minor since the piezoelectric transducers remain attached to the cross-section of the rail during a potential in-track application.

Similarly to the transmission coefficient, the reflection coefficient C_R is given by the ratio of the reflected wave's amplitude to the incident wave's amplitude [28, 35]. The plot of the reflection coefficient across normalized crack depth, which is shown in Figure 3.2(b), reveals a non-monotonic

increase of C_R with a/λ_R. In order to characterize the transformation to bulk waves, both the transmission and the reflection coefficient have to be measured [28].

An open surface crack results in a delay in a SAW's TOF compared to the undamaged specimen. Although this approach can be employed in the characterization of fatigue cracks under tensile load for a wide range of a/λ_R, it is not applicable for partially closed cracks [8]. Consequently, the TOF cannot be used to assess head checks. An evaluation of a crack's impact on a propagating SAW in the frequency domain is put forward in [29] by investigating the shift in the center frequency of the SAW pulse, but only a non-monotonic trend was found.

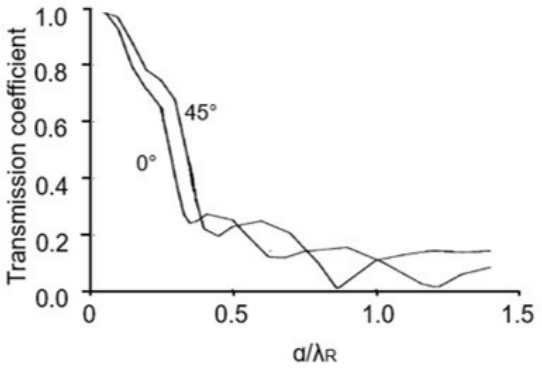

(a) Theoretical trend of the transmission coefficient C_T over normalized crack depth a/λ_R. Different angles of incidence are illustrated. Adapted from [35].

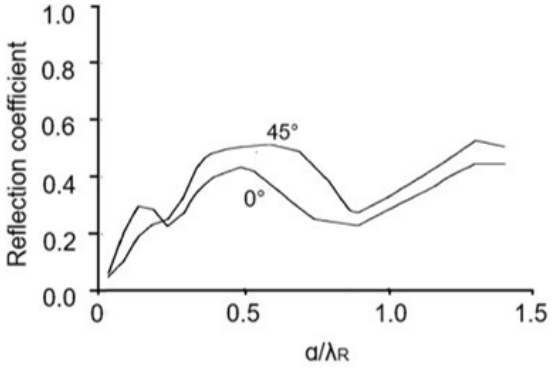

(b) Theoretical trend of the reflection coefficient C_R over normalized crack depth a/λ_R. Different angles of incidence are illustrated. Adapted from [35].

Fig. 3.2: Theoretically computed transmission coefficient C_T and reflection coefficient C_R of a SAW propagating over an ideal surface breaking crack.

3.3.2 Non-linear Wave Features

The mechanical interaction of a SAW with defects in the specimen's microstructure causes a non-linear propagation behavior of the SAW. These defects exhibit a non-linear stress-strain relation and can therefore lead to non-linear ultrasonic phenomena, such as the generation of higher-order and subharmonics [33, 36]. Exploiting the generation of higher-order harmonics offers the potential for assessing micro-scale defects. Non-linear damage indices computed from the amplitude of the second-order harmonic have already been applied in laboratory experiments to evaluate stress corrosion cracks [37] and fatigue damage [32]. When assessing closed cracks, the evaluation of subharmonic amplitude in a phased array setup comprising multiple transducers provides superior performance compared to that of higher-order harmonics. However, for both approaches, high-amplitude ultrasonic waves and therefore high-power signal generators are required [33]. Other

non-linear ultrasonic characteristics, for instance non-linear frequency-mixing, and their application for damage detection are described in [33].

Non-linearity is to a certain extent inevitable in any measurement setup, as noise, coupling media, and the instruments might have non-linear responses. Features like the second-order harmonic amplitude are dependent on the propagation distance of the wave, while these ambient non-linearities are not [36]. Consequently, the non-linearity due to the microstructure can be determined by measuring the second-order harmonic amplitude at different distances or by using different excitation frequencies [37].

3.3.3 Selection of the Wave Feature for the Assessment of Head Check Depth

During the selection of the wave feature to assess head check depth, a simple measurement setup was sought to ensure the evaluation methodology's applicability in the track. Furthermore, the complex crack configuration, caused by partially closed and overlapping cracks, was taken into account. It is an open question whether wave features which have already been deployed for the sizing of open cracks are applicable to head checks given the complex geometry. However, a qualitative effect of partially closed head checks on the transmission coefficient was previously found in [3]. Motivated by this discovery and recognizing the transmission coefficient's simplicity and robustness, this master's thesis examines the potential of the SAW transmission coefficient to quantitatively assess crack depth.

Chapter 4
Selected Concepts of Signal Processing

The aim of this chapter is to introduce the reader to selected principles of signal processing, such as cross-correlation and autocorrelation. These techniques are extensively used in the evaluation of the measurement data characteristics. Furthermore, the Hilbert transform and the so-called analytic signal are presented, since the developed signal processing algorithm relies heavily on these methods. Finally, an introduction to model-based signal processing is provided. The theoretical background of other signal processing concepts relevant for this thesis, including analog-to-digital conversion, digital filters, and the Fourier transform, can be found in [38, 39, 40].

4.1 Cross-Correlation and Autocorrelation

The degree of similarity between signals can be ascertained using the well-established mathematical technique of correlation. The correlation $\rho_{x,y}(\tau)$ of two complex continuous-time signals $x(t)$ and $y(t)$ is defined as

$$\rho_{x,y}(\tau) = \int_{-\infty}^{\infty} x(t+\tau)y^*(t)\,\mathrm{d}t, \tag{4.1}$$

where $y^*(t)$ signifies the complex conjugate of $y(t)$ [38]. Similarly, the correlation between two complex discrete-time signals $x[n]$ and $y[n]$ evaluates to

$$\rho_{x,y}[l] = \sum_{n=-\infty}^{\infty} x[n+l]y^*[n]. \tag{4.2}$$

Again $y^*[n]$ denotes the complex conjugate of $y[n]$. In a visual representation, $x[n]$ undergoes a step-wise shift across $y[n]$, and the overlap is computed at each lag l. If the functions $x[n]$ and $y[n]$ differ from each other, the result of this operation, $\rho_{x,y}[l]$, is termed the cross-correlation function. Conversely, if the functions are identical, the correlation function $\rho_{x,x}[l]$ is designated as the autocorrelation function, signifying that the signal $x[n]$ is correlated with itself [38].

Certain authors [41, 42] introduce a normalization term for the correlation $R_{x,y}[l]$ of power signals, extending Equation 4.2 to

$$R_{x,y}[l] = \lim_{N\to\infty} \frac{1}{2N+1} \sum_{n=-N}^{N} x[n+l]y^*[n]. \tag{4.3}$$

However, for the practical signal analysis detailed in Section 5.1, the definition as per Equation 4.2 will be used, given that all recorded signals share a consistent sample length and frequency.

Autocorrelation stands as a powerful instrument in the analysis of stochastic signals. Techniques akin to deterministic linear systems theory are applicable to the autocorrelation of such random signals. In fact, the autocorrelation signal and the power spectral density (PSD) jointly form a Fourier transform pair, mirroring the relationship between a deterministic signal and its spectrum.

Consequently, the discrete-time Fourier transform ($DTFT$) is used to calculate the PSD [43]. Given a random signal $x[n]$, its PSD $S_{x,x}(f)$ can be computed according to the *Wiener-Khintchine* theorem [41, 43], which is formalized as

$$S_{x,x}(f) = DTFT\{x[n]\} = \sum_{l=-\infty}^{\infty} \rho_{x,x}[l]\mathrm{e}^{-\mathrm{i}2\pi fk}. \tag{4.4}$$

In simple words, the PSD illustrates the contribution of each frequency to the total power of the signal [38].

4.2 Hilbert Transformation and Analytic Signal

Given a signal $x(t)$, its Hilbert transform $h(t)$ is defined as

$$h(t) = x(t) \overset{p.v.}{*} \frac{1}{\pi t} = \frac{1}{\pi} \int_{-\infty}^{\infty} \frac{x(\tau)}{t-\tau}\,\mathrm{d}\tau. \tag{4.5}$$

This convolution integral cannot be computed by conventional means, since $1/\pi t$ exhibits a jump discontinuity at $t = 0$. Hence, $h(t)$ is specified using its Cauchy principal value *p.v.* [44, 45]. Considering the definition in the frequency domain yields

$$H(\omega) = X(\omega)\mathfrak{FT}\left[\frac{1}{\pi t}\right], \tag{4.6}$$

with $\mathfrak{FT}$ denoting the Fourier transform.

It is demonstrated in the related literature, such as [45], that the Fourier transform of the Signum function $\mathrm{sgn}(t)$ evaluates to

$$\mathfrak{FT}[\mathrm{sgn}(t)] = \frac{2}{\mathrm{i}\omega}. \tag{4.7}$$

For a Fourier transform pair $x(t) \longleftrightarrow X(\omega)$, the Duality theorem of the Fourier transform is formalized as $X(t) \longleftrightarrow 2\pi x(-\omega)$ [38, 46]. Applying the Duality theorem to the Fourier transform of the Signum function given in Equation 4.7 leads to

$$\mathfrak{FT}\left[\frac{2}{\mathrm{i}t}\right] = 2\pi \operatorname{sgn}(-\omega) \tag{4.8}$$

and subsequently to

$$\mathfrak{FT}\left[\frac{1}{\pi t}\right] = -\mathrm{i} \operatorname{sgn}(\omega). \tag{4.9}$$

Substituting this result back into Equation 4.6 yields

$$H(\omega) = -\mathrm{i} \operatorname{sgn}(\omega) X(\omega). \tag{4.10}$$

From Equation 4.10, it becomes evident that the Hilbert transform only shifts the phase of the given signal by 90 degrees but does not affect its magnitude. Specifically, for $\omega > 0$, the Hilbert transform $h(t)$ of a signal $x(t)$ leads to a phase delay of 90 degrees, as illustrated in Figure 4.1.

The analytic signal $A(t)$ computed from a real-valued signal $x(t)$ is a complex-valued signal defined to have $x(t)$ and $h(t)$ as its real and imaginary components: $A(t) = x(t) + \mathrm{i}h(t)$ [40]. The value of the absolute magnitude $|A(t)|$ can be calculated using $|A(t)| = \sqrt{x^2(t) + h^2(t)}$. This value provides the so-called instantaneous amplitude, which forms the envelope of $x(t)$ [45]. As shown in Figure 4.1, the instantaneous amplitude $|A(t)|$ of a sinusoidal signal $x(t)$ with a constant amplitude is constant.

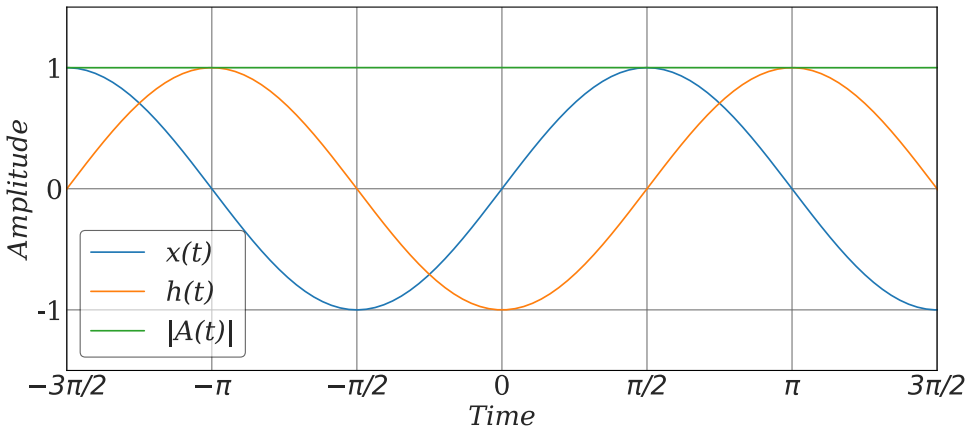

Fig. 4.1: The instantaneous amplitude $|A(t)|$ provides the envelope of a given signal $x(t)$. The Hilbert-transformed signal $h(t)$ has a phase delay of 90 degrees compared to $x(t)$ and forms the imaginary part of the analytic signal $A(t)$.

4.3 Principles of Model-Based Signal Processing

If a signal is predictable, e.g., repeating a measurement multiple times results in exactly the same measurement signal, then the signal is said to be deterministic. However, in reality, most signals obtained from measurements are subject to extraneous variations, such as electronic noise. They are not repeatable as the extraneous variations lead to varying output signals when measuring continuously. These non-repeatable signals are referred to as random signals [43]. While it is not possible to precisely predict random signals, they can be described using statistical parameters [38, 46].

The principal aim of signal processing is to extract the relevant information from a signal and reject the extraneous variations [43]. The required complexity of a signal processing approach is mainly determined by the inherent noise in the measurement signal. A simple approach may be sufficient for signals that are hardly contaminated with noise and therefore have a high signal-to-noise ratio (SNR). However, the lower the SNR of the incident signal, the higher the required complexity of a signal processing approach to achieve a satisfactory SNR of the processed signal. Model-based signal processing is considered to be the most powerful, yet the most complex signal processing strategy. It enables the embedding of a priori knowledge about the physical phenomenon and the measurement principle into the signal processor by the use of mathematical models. An increasing physical understanding of the system under study facilitates the embedding of more accurate models in the signal processor, leading to a higher quality of the signal processing results. Obviously, a correct analytical or numerical model of the physical phenomenon is a prerequisite for employing a model-based approach [43].

The measurement Y_{meas} of the true value S_{true} of a physical quantity with an ideal measurement device is given by [43]

$$Y_{meas} = S_{true} + N_{noise}, \tag{4.11}$$

where the noise N_{noise} may be modeled by a Gaussian distribution with mean $\mu = 0$ and variance $\sigma^2 = R_{nn}$: $N_{noise} \sim \mathcal{N}(0, R_{nn})$. Therefore, the estimation error ($\tilde{S} = S_{true} - \hat{S}$) variance is equal to R_{nn} for the ideal measurement device. $\hat{S}$ represents the estimate of S_{true}.

A more realistic model for the measurement process can be obtained by introducing the measurement system function $C(S_{true})$ [43]:

$$Y_{meas} = C(S_{true}) + N_{noise}, \qquad N_{noise} \sim \mathcal{N}(0, R_{nn}). \tag{4.12}$$

If the measurement is performed with a voltmeter, for example, the measurement can simply be modeled by an amplification gain K, thus resulting in the measurement system function $C(S_{true}) = KS_{true}$ [43]. The associated estimation error variance for this model of a real measurement device may be denoted by $\tilde{R}$.

Ultimately, knowledge about the physical process can be incorporated into the signal processor. In this case, the estimation error variance may be represented by $\tilde{P}$. It is intuitively expected that with increasing model complexity, the estimation error variance will decrease as more aspects of the system under study are included in the model. Indeed, it can be shown mathematically that $\tilde{P} < \tilde{R} < R_{nn}$ [43]. This demonstrates the core concept of model-based signal processing: The more physical knowledge is incorporated through mathematical models, the smaller the error of the estimate $\hat{S}$. The estimation $\hat{S}$ of the true quantity S_{true} from the measured value Y_{meas} based on models for the physical process and the measurement instrument is schematically illustrated in Figure 4.2.

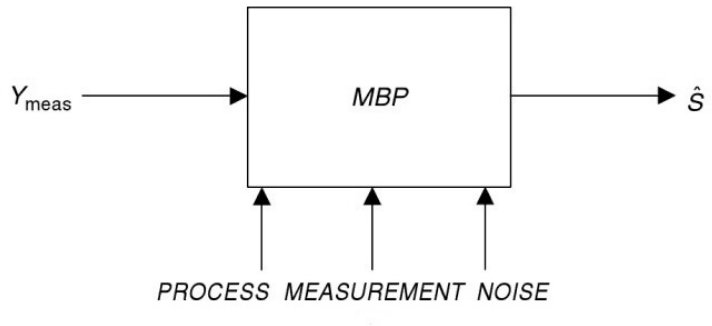

Fig. 4.2: Schematic illustration of a model-based signal processor used to obtain an estimate $\hat{S}$ of the true value S_{true} of a physical quantity based on the measurement Y_{meas}. This signal processor incorporates models for the physical process and the measurement instrument, as well as the associated uncertainties of both. Adapted from [43].

Another significant advantage of model-based signal processing is the ability to integrate parameters that cannot be directly measured as unknown parameters in the model. Given the measurement, the unknown parameters of these adaptive models are then determined by solving the joint estimation problem [47].

A model-based approach for structural health monitoring (SHM) of plate-like structures using Lamb waves is presented in [48]. The proposed method employs adaptive analytical models with crack position and depth as unknown parameters. The Levenberg-Marquardt algorithm [48, 49] is applied to solve the optimization problem. In contrast to plate-like structures, rails have a much more intricate geometry. Wave propagation in rails can only be numerically modeled, e.g., with a finite element model. However, this strategy requires that all relevant material parameters are known in advance to obtain an applicable model [47]. Furthermore, the computational time for complex finite element models is significant. Consequently, the implementation of a model-based signal processing approach is beyond the scope of this thesis due to these challenges.

Chapter 5
Data Characteristics and Applied Signal Processing

The aim of this chapter is to give an overview of the characteristics of the recorded signals. In addition, the signal processing algorithm developed for extracting the surface acoustic wave (SAW) feature from the measurement signals is presented.

5.1 Investigations on the Characteristics of Recorded Signals

In a first step, it was evaluated how the recorded signals change with increasing distance from the piezoelectric transducer that excited the surface acoustic wave. Another focus was on signal quality.

Measurements were conducted on the surface along the rail head. This plane surface ensures a fixed ratio of the surface wave's in-plane and out-of-plane displacement. When generating the SAW, the transducer was driven by a voltage signal composed of five sinusoidal pulses, also referred to as 5-pulse burst, with an excitation frequency of $f_x = 1.0\,\mathrm{MHz}$. A Laser Doppler vibrometer (LDV) was employed to gauge the surface's out-of-plane displacements. Additionally, the distance d_k from the source was adjusted with a precision of $0.1\,\mathrm{mm}$. The exact measurement setup is detailed in Section 6.3.

The signals considered for this investigation are denoted by s_k with $k \in \{1,\ldots,5\}$, as they are recorded at a specific distance d_k from the source. d_k varies in the range from $d_1 = 20\,\mathrm{mm}$ to $d_5 = 100\,\mathrm{mm}$ with steps of $\Delta d_k = 20\,\mathrm{mm}$. Figure 5.1 displays the recorded signals. It is evident that the actual number of peaks in the recorded signals exceeds the number of five. This implies that the surface at a given point continues to oscillate slightly longer due to inertia. As anticipated, the burst's arrival time increases with distance, while the wave amplitude decreases. From Figure 5.1, it becomes also evident that these measurements are affected by noise.

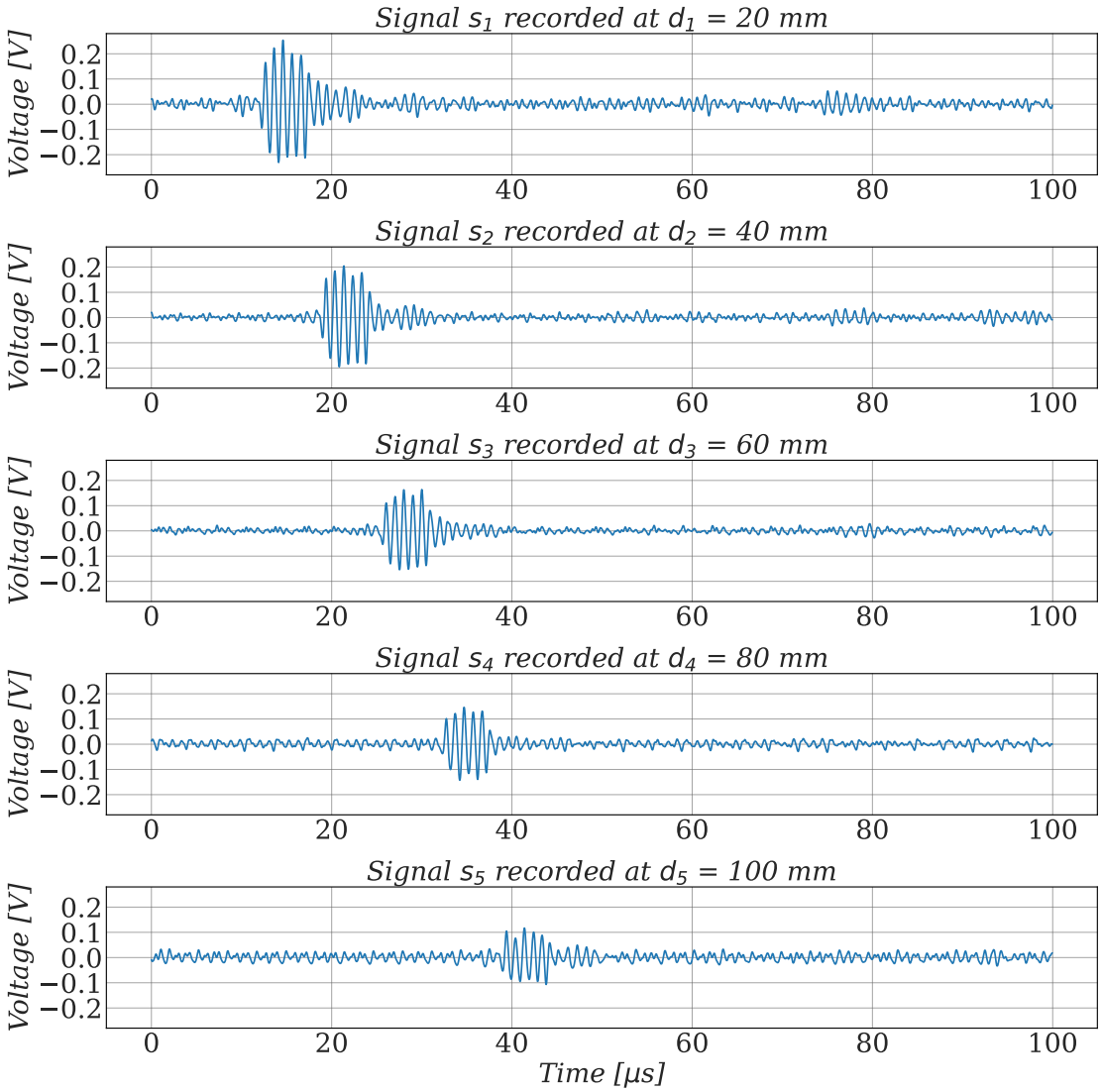

Fig. 5.1: Signals s_k with $k \in \{1,\ldots,5\}$ recorded by a Laser Doppler vibrometer at different distances d_k from the source. d_k varies in the range from $d_1 = 20\,\text{mm}$ to $d_5 = 100\,\text{mm}$ with steps of $\Delta d_k = 20\,\text{mm}$. Measurements were performed on the plane surface along the rail head.

5.1.1 Time Domain Analysis Based on Cross-Correlation

As already mentioned in Section 4.1, cross-correlation is an excellent operation for measuring similarity between two signals. In fact, it can be used to find a given reference signal in a measured signal [38]. The time delay between the investigated signals can be determined by computing cross-correlation. Indeed, the calculation of the surface acoustic wave's velocity, conducted in Section 6.3.1, is based on time delays determined by means of cross-correlation.

Furthermore, cross-correlation can be employed to assess the signal quality, as measurements were captured at different distances from the source. For this purpose, cross-checks of arrival times can be used. The notation ρ_{s_i,s_j} represents the cross-correlation of two signals s_i and s_j. The correlations $\rho_{s_i,s_{i+1}}$ of spatially consecutive signals s_i and s_{i+1} with $i \in \{1,\ldots,4\}$ were computed. Additionally, signal s_1 was selected as the reference and all other signals s_j with $j \in \{2,\ldots,5\}$ were cross-correlated with this reference. The computed cross-correlations are illustrated in Figures 5.2 and 5.3, respectively. The computation was executed with *numpy's correlate* function. The peaks in the correlation signals are indicated by red crosses.

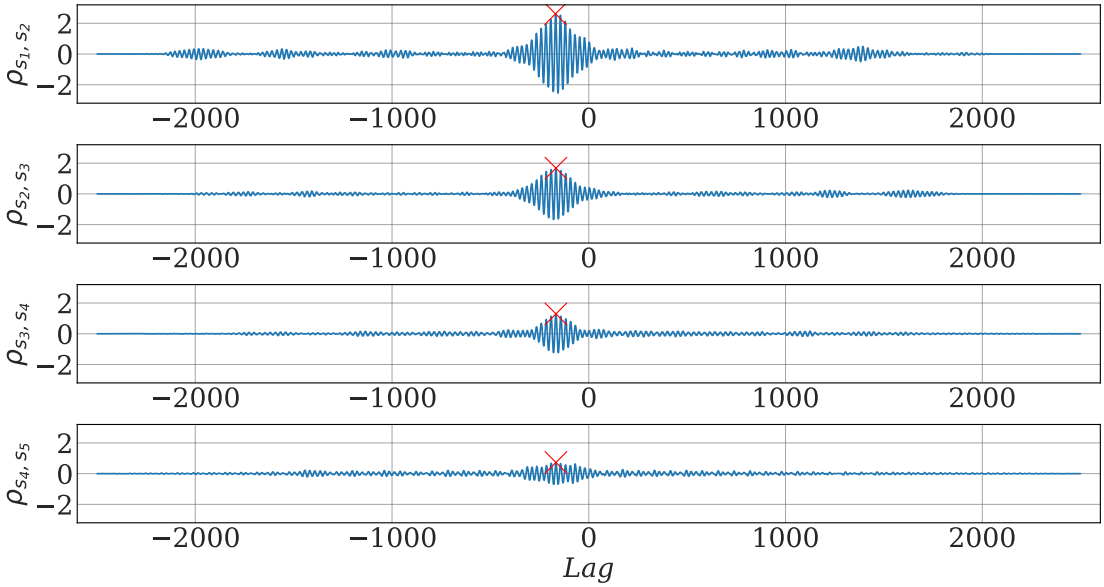

Fig. 5.2: Cross-correlations $\rho_{s_i,s_{i+1}}$ of spatially consecutive signals s_i and s_{i+1}. From top to bottom, i increments by 1, starting with $i = 1$ in the topmost diagram. Peaks are indicated by red crosses. The peaks appear approximately at the same lag across all cross-correlations. Table 5.1 lists the exact lags of the peaks in $\rho_{s_i,s_{i+1}}$ and provides the cumulative sum of these peak lags.

When correlating two ideal 5-pulse burst signals, a correlation signal with 9 peaks is expected. However, as both Figure 5.2 and Figure 5.3 illustrate, the correlation of the measured signals results in more than 9 peaks. This is caused by post-pulse oscillations, but also by systematic patterns in the noise. The surface wave's amplitude decays with distance, due to geometrical and physical reasons. This means that the signal-to-noise ratio (SNR) decreases with increasing distance from the source. Consequently, the peaks in the correlation signal become less distinct as the distance from the source increases.

The geometrical distances between consecutive measurement positions are equal. Therefore, it is anticipated that the peaks in the cross-correlations of spatially consecutive signals consistently appear at the same lag. Moreover, the sum of peak lags from the correlation of spatially consecutive signals is expected to match the position of the peak in the correlation of the reference signal with

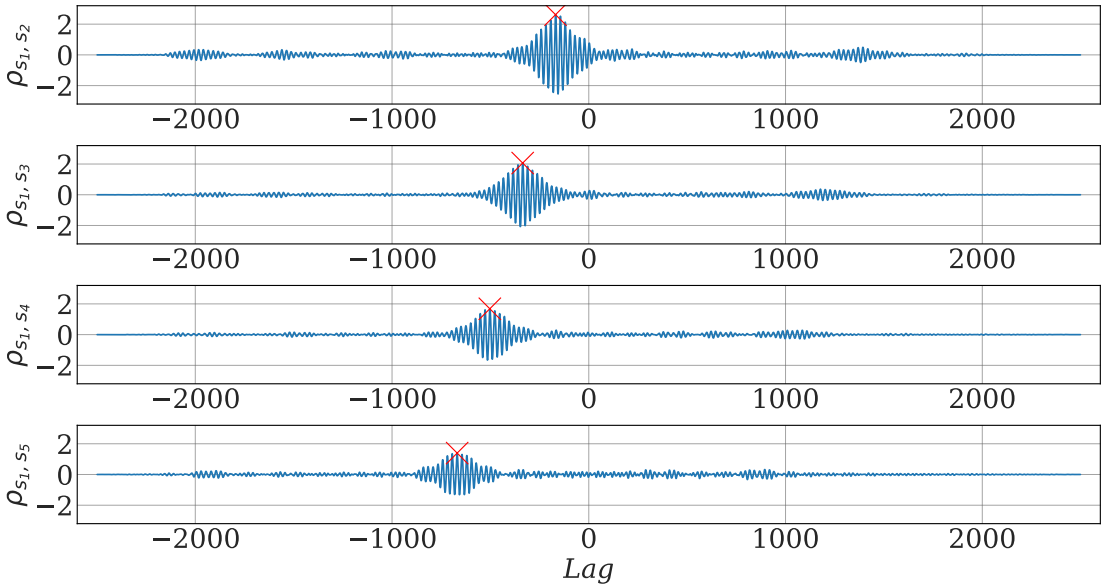

Fig. 5.3: Cross-correlations ρ_{s_1,s_j} of the reference signal s_1 with all other recorded signals s_j. From top to bottom, j increments by 1, starting with $j = 2$ in the topmost diagram. Peaks are indicated by red crosses. The lags of the peaks in ρ_{s_1,s_j} are listed in Table 5.1. These peak lags align with the accumulated peak lags from the cross-correlations $\rho_{s_i,s_{i+1}}$ of spatially consecutive signals, indicating good signal quality.

the last signal considered during the sequential evaluation. For example, it is expected that

$$\arg\max(\rho_{s_1,s_3}) = \arg\max(\rho_{s_1,s_2}) + \arg\max(\rho_{s_2,s_3}). \tag{5.1}$$

The respective lag of the peak for each cross-correlation illustrated in Figure 5.2 and Figure 5.3 is provided in Table 5.1. Additionally, the sum of peak lags obtained from correlating spatially consecutive signals is given. These accumulated peak lags align with the actual peak lag in the correlation calculated with the reference signal. This is regarded as an indicator of good signal quality.

Table 5.1: Lags of peaks in investigated cross-correlations. For the correlation $\rho_{s_i,s_{i+1}}$ of spatially consecutive signals, the actual peak lag and the accumulated peak lags are given. For the correlation ρ_{s_1,s_j} with the reference signal s_1, the actual peak lags are displayed.

i	1	2	3	4
$\arg\max(\rho_{s_i,s_{i+1}})$	-169	-167	-167	-167
$\sum_{n=1}^{i} \arg\max(\rho_{s_n,s_{n+1}})$	-169	-336	-503	-670
$\arg\max(\rho_{s_1,s_{i+1}})$	-169	-336	-503	-669

Autocorrelation is an effective method for analyzing signals in the time domain. It filters out ideal white noise, thereby reducing the inherent randomness in captured signals [43]. For illustration, Figure 5.4 depicts the autocorrelation ρ_{s_1,s_1} of signal s_1. The resulting autocorrelation signal manifests symmetry, exhibiting a prominent peak when the lag l is zero. A subsidiary peak is observed at a lag of $l \approx 1500$. Given a sampling frequency $f_s = 25\,\text{MHz}$, this lag corresponds to a time delay of $\Delta t = 60\,\mu\text{s}$. When observing signal s_1 in Figure 5.1, it becomes evident that a reflection of the surface wave occurs approximately $60\,\mu\text{s}$ after the detection of the actual SAW. Consequently, autocorrelation offers the capability to identify reflections in a given signal.

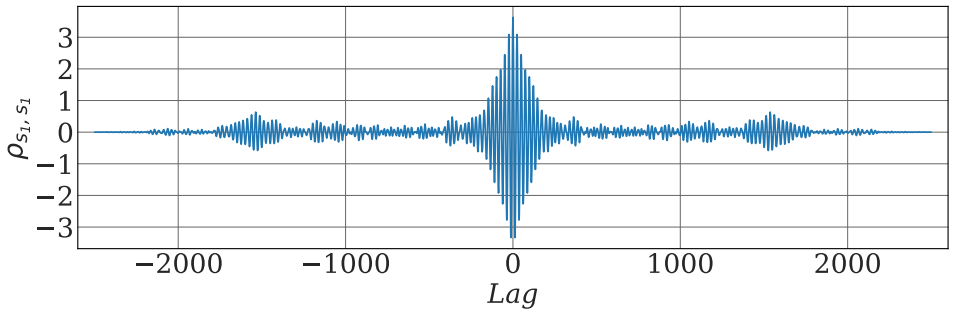

Fig. 5.4: Autocorrelation ρ_{s_1,s_1} of signal s_1. The subsidiary peak at a lag of $l \approx 1500$ is caused by a reflection of the surface acoustic wave. Its lag l aligns with the time delay $\Delta t = 60\,\mu\text{s}$, which is observed in s_1 between the arrival of the actual SAW and its reflection.

5.1.2 Frequency Domain Analysis Based on Power Spectral Density

The power spectral density (PSD) $S_{x,x}$ can be computed from a given autocorrelation signal ρ_{s_x,s_x} by means of the discrete-time Fourier transform [39, 42, 43]. The PSD of each of the signals s_1 to s_5 is illustrated in Figure 5.5. Sometimes the power spectral density is also referred to as the power spectrum.

The observed overall pattern is consistent across all power spectra in Figure 5.5. These spectra exhibit an asymmetric shape. As expected, there is a diminishing power content in the signals as the distance from the wave source increases. Despite a fixed excitation frequency of $f_x = 1.0\,\text{MHz}$, peaks are observed at slightly higher frequencies. One potential cause for the asymmetry could be the system's unknown impulse response. Every linear time-invariant system is completely characterized by its impulse response $h(t)$ [38]. When the frequency domain representation of the system's impulse response, $H(\omega)$, is asymmetric, the resulting output signal $Y(\omega)$ will also be skewed in the frequency domain, even if the input signal $X(\omega)$ is symmetric.

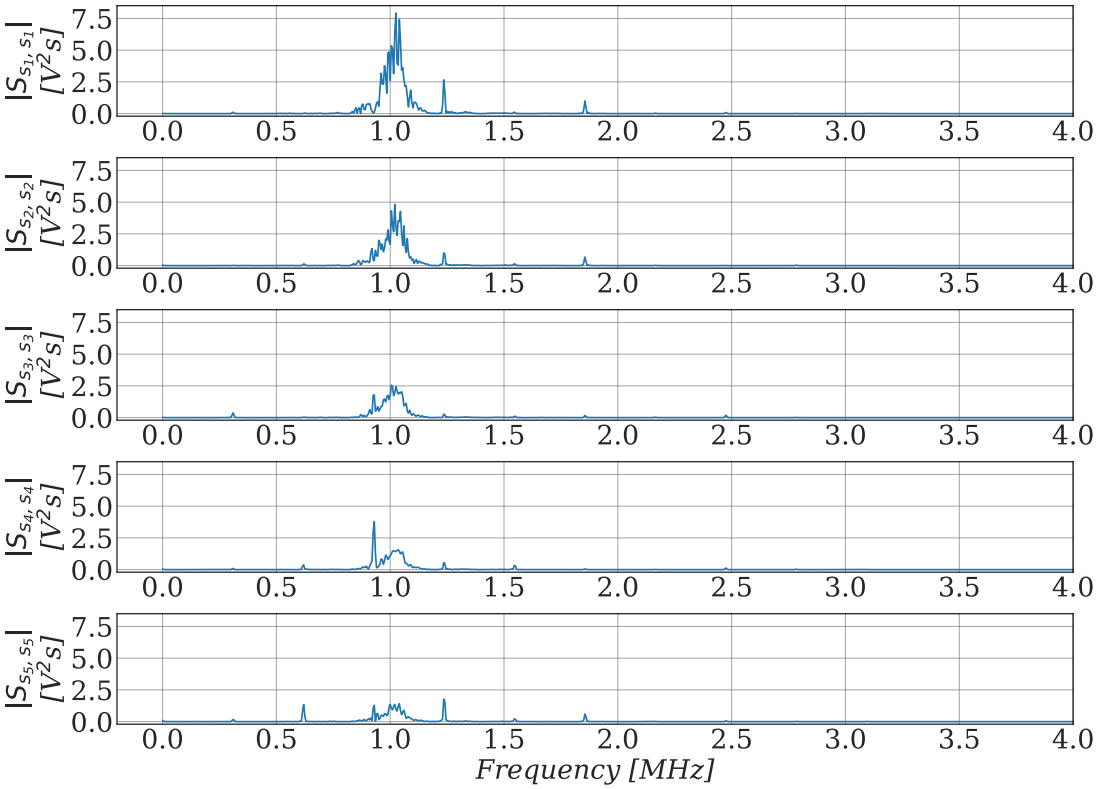

Fig. 5.5: Power spectral densities S_{s_1,s_1} to S_{s_5,s_5} for the investigated signals s_1 to s_5. These spectra exhibit an asymmetric shape. As anticipated, the power content in the signals diminishes with increasing distance from the wave source. Sharp subsidiary peaks are observed. The frequencies at which these peaks occur are consistent across all PSDs.

Additionally, subsidiary peaks can be identified in each signal's PSD. Notably, these peaks emerge at similar frequencies across all spectra. This observation suggests that every captured signal is superimposed with systematic disturbances occurring at certain specific frequencies. Although they have a small power content compared to the main peak at the excitation frequency, these subsidiary peaks were examined more thoroughly.

Specific segments of the signals s_3, s_4, and s_5 were isolated to investigate the power spectrum of their noise. Only those parts of the measurement signals recorded at time $t > 50\,\mu$s were taken into account. The PSD was recalculated for these cropped measurements, with the outcomes for the signals s_3 to s_5 depicted in Figure 5.6. Signals s_1 and s_2 were excluded from the analysis, because they contain reflections of the actual surface wave.

Instead of being evenly distributed, the power in the noise is concentrated at certain frequencies. In fact, all peaks in the power spectra displayed in Figure 5.6 align with a frequency of $f = 0.31\,$MHz or its integer multiples. The spectrogram of signal s_5 is presented in Figure 5.7 to further underscore the dominance of these frequencies.

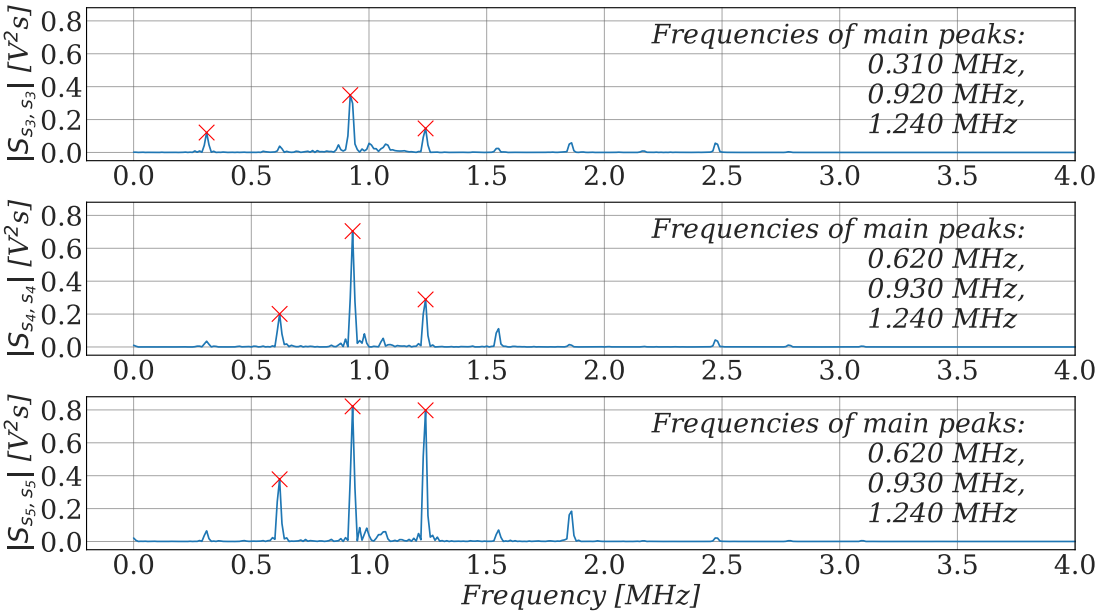

Fig. 5.6: Power spectral densities of segments from signals s_3 to s_5 to illustrate the power content of recorded noise. Peaks are indicated by red crosses; the respective frequencies are printed in the plots. The frequencies of the peaks in the background noise align with a frequency of $f = 0.31\,\mathrm{MHz}$ or its integer multiples. This suggests that every captured signal is superimposed with systematic perturbations occurring at particular frequencies.

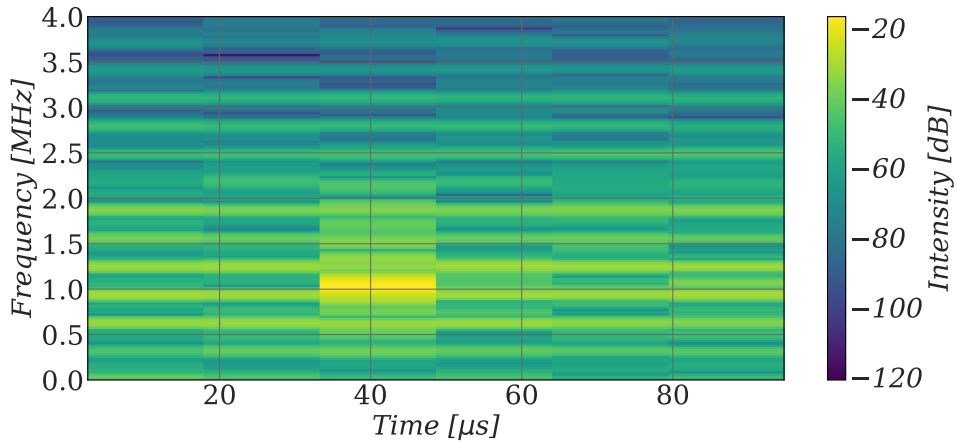

Fig. 5.7: Spectrogram of signal s_5. This visualization provides insight into how the spectrum evolves with time. The power content corresponding to frequencies that are integer multiples of $f = 0.31\,\mathrm{MHz}$ remains almost constant over time. This finding supports the hypothesis that all recorded signals contain systematic disturbances. Additionally, the arrival of the actual SAW burst with excitation frequency $f_x = 1.0\,\mathrm{MHz}$ at a time $t \approx 40\,\mu\mathrm{s}$ is clearly visible.

The spectrogram is calculated using the short-time Fourier transform (STFT) and reveals how the power spectrum changes over time. There is an inherent trade-off between time and frequency resolution; greater time resolution results in diminished frequency resolution, and vice versa. The spectrogram depicted in Figure 5.7 clearly indicates that the power content corresponding to frequencies that are integer multiples of $f = 0.31\,\mathrm{MHz}$ remains almost constant over time. This finding supports the hypothesis that all recorded signals contain systematic disturbances. Additionally, the arrival of the actual SAW burst with the excitation frequency $f_x = 1.0\,\mathrm{MHz}$ at a time $t \approx 40\,\mu\mathrm{s}$ is clearly visible in the spectrogram.

The PSD of the recorded signal still shows spikes at multiples of $f = 0.31\,\mathrm{MHz}$ even if no cables are connected to the measurement device and a measurement is initiated. This suggests that the origin of these disturbances lies within the device itself, eliminating acoustic reflections on the rail surface as a potential cause. Presumably, electromagnetic interference is the reason, although this theory is not conclusively verified in this thesis. Given their consistent presence across all measurements, a strategy to address these systematic disturbances has been defined.

5.2 Processing of Recorded Signals

Since all recorded measurement signals contain unwanted disturbances at certain characteristic frequencies, it was necessary to remove them from the signal. Thus, a digital bandpass filter was used during the processing of the signals. Although the application of a comb filter would be an alternative for diminishing systematic disturbances, a bandpass filter also reduces stochastic noise. Moreover, when choosing the excitation frequencies for the sent SAW, it was ensured that they did not overlap with the frequencies of the disturbances. In fact, for the experiments examining the influence of head check depth on the SAW transmission coefficient, the excitation frequency of the generated burst signals was varied in a range from $f_x = 0.7\,\mathrm{MHz}$ to $f_x = 1.9\,\mathrm{MHz}$ with steps of $\Delta f_x = 0.3\,\mathrm{MHz}$. A thorough description of the experimental setup is presented in Chapter 7.

The intent of this section is to provide an insight into the design and testing of the desired filter. Additionally, the defined signal processing routine is presented. This routine was applied to all measurements recorded during the experiments detailed in Chapter 6 and Chapter 7.

5.2.1 Filter Design

A Bessel-Thomson type filter was selected, because this type of filter is known for its linear phase response [38]. Moreover, these filters have little overshoot. This property was verified by computing the step response of a Bessel-Thomson lowpass filter.

To mitigate the perturbations observed at all harmonics of $f = 0.31\,\text{MHz}$, the bandwidth B of the bandpass filter needs to be $B < 0.31\,\text{MHz}$. Additionally, it must be considered that the lower cutoff frequency f_L and the upper cutoff frequency f_U depend on the excitation frequency of the sent burst signal f_x. These cutoff frequencies can be calculated from f_x by adding constant values Δf_L and Δf_U, respectively. By empirical testing, it was determined that $\Delta f_L = -0.05\,\text{MHz}$ and $\Delta f_U = 0.15\,\text{MHz}$ allow for a maximum bandwidth while still effectively filtering out all perturbations. So, for example, for a burst sent with $f_x = 1.0\,\text{MHz}$ the cutoff frequencies evaluate to $f_L = 0.95\,\text{MHz}$ and $f_U = 1.15\,\text{MHz}$. The constant frequency offsets Δf_L and Δf_U ensure effective filtering regardless of the chosen excitation frequency f_x of the pulse.

Given the filter type and cutoff frequencies, an appropriate filter order was determined. *Python's scipy* package can compute a filter's transfer function using the filter type, cutoff frequencies, and filter order. The frequency responses of Bessel-Thomson bandpass filters of different orders were examined. The frequency responses are shown in Figure 5.8. The frequency response includes both amplitude and phase responses. These characterize the amplitude decay and phase shift introduced by the filter. For a filter order of 1, the bandwidth remains expansive. However, the bandwidth reduces as the filter order increases. It should be noted that the uneven amplitude response in the fifth-order filter is not the result of numerical errors. From observing the phase response, it is evident that the fifth-order filter has the most significant phase shift spread between low and high frequencies.

In the final signal processing algorithm, highlighted in Section 5.2.3, the designed filter is applied forwards and backwards to the signal. Given the impulse response of the filter $h(t)$ and the input signal $x(t)$, the output $y_f(t)$ from the forward filtering procedure can be computed by $y_f(t) = h(t) * x(t)$, with the symbol $*$ denoting the convolution of $h(t)$ and $x(t)$. Reversing $y_f(t)$ yields $y_f^R(t)$, where the superscript R indicates the reversal of the original signal. The final output $y_{fb}(t)$ from applying the filter forwards and backwards is obtained by again reversing the result after the filter is applied on $y_f^R(t)$: $y_{fb}^R(t) = h(t) * y_f^R(t)$. Thereby, the amplitude response is squared and the time delay is canceled out [50, 51]. Thus, the filter's time delay due to its phase response can be neglected. Nonetheless, it must be emphasized that this procedure can only be implemented offline when the signal has been fully captured in advance.

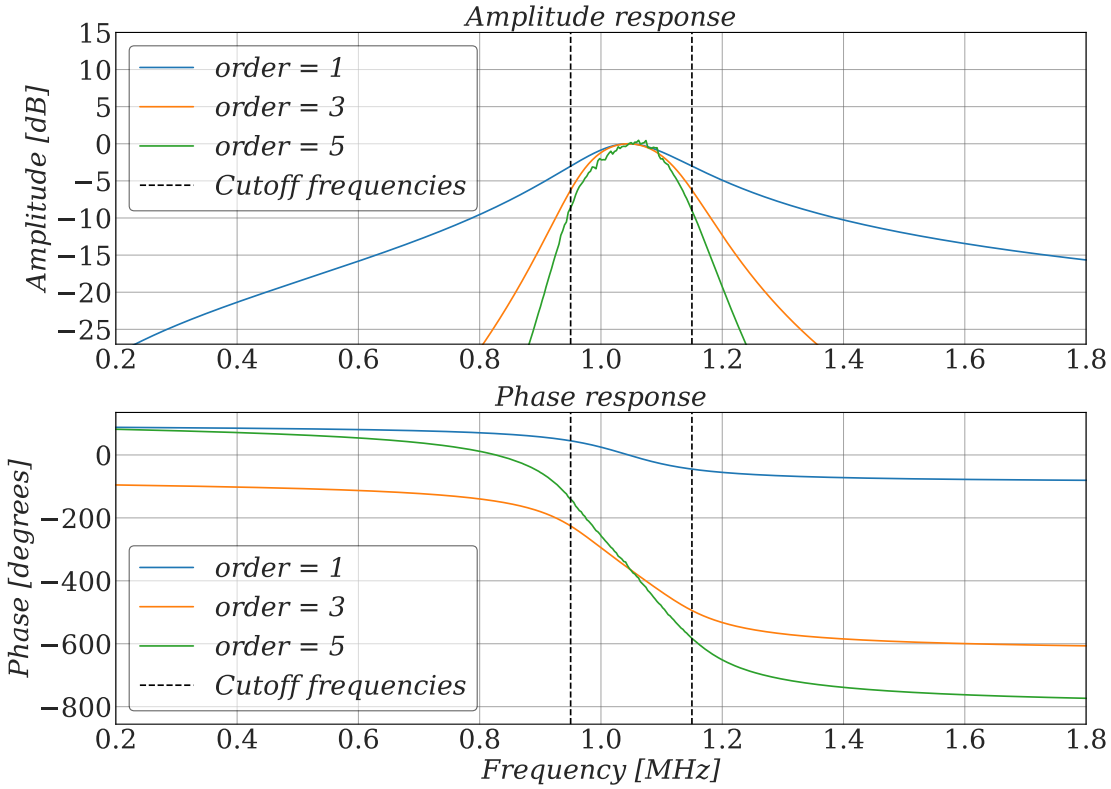

Fig. 5.8: Frequency response for Bessel-Thomson type bandpass filters of different orders with cutoff frequencies of $f_L = 0.95\,\text{MHz}$ and $f_U = 1.15\,\text{MHz}$. The filter's frequency response characterizes its steady state behavior. The bandwidth decreases and the phase delay increases with ascending filter order.

Typically, a filter's steady state behavior is evaluated by determining its frequency response. Yet, when the filter is applied to signals containing sudden changes, the filter's transient behavior plays a vital role. In simple terms, an abrupt variation in a signal represents a transient. Such transients in the input signal disrupt the stable operation of a filter, leading to a transient response in the filter's output [50]. A filter's transient behavior can be assessed by its impulse response or its step response. Figure 5.9 depicts the step responses for Bessel-Thomson bandpass filters of different orders. From this figure, it becomes evident that higher-order filters exhibit a significant time delay. These filters respond slowly when encountering a step function input. Hence, higher-order filters might struggle with rapid amplitude changes in input signals. Furthermore, as seen in Figure 5.9, bandpass filters eliminate long-term trends from signals as their step responses trend towards zero over time.

Setting the filter order to three was considered to be a reasonable trade-off between rise-time and effective removal of unwanted frequencies. This decision completed the filter's definition.

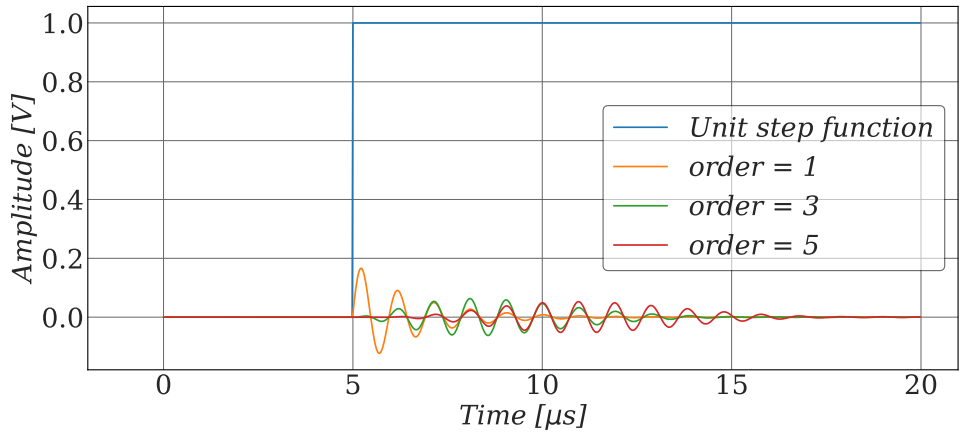

Fig. 5.9: Step response for Bessel-Thomson type bandpass filters of different orders. The filter's step response characterizes its transient behavior. Higher-order filters only respond slowly to transient changes in the input signal.

5.2.2 Testing of the Designed Filter

To test the filter, it was applied to a set of recorded signals, and the resulting filter output was analyzed. These signals stemmed from measurements of the incident wave amplitude, which are presented in Chapter 7. In contrast to the signals showcased in the previous Section 5.1, the experimental setup was different. The Laser Doppler vibrometer still gauged the out-of-plane displacement on the rail head's side, but the piezoelectric transducer was positioned on the rail head's bottom side. For a detailed description of the setup used to generate these signals, please refer to Section 7.1.

The output signal obtained when applying the filter forwards and backwards to a signal with an excitation frequency $f_x = 1.6\,\text{MHz}$ is illustrated in Figure 5.10. This particular excitation frequency was chosen due to its proximity to the systematic disturbance at $f = 1.54\,\text{MHz}$. Both the time domain representation and the PSD of the output and input signals are displayed. The PSD reveals that the filter effectively removes all disturbances, including the one at $f = 1.54\,\text{MHz}$. As a result, the designed filter was regarded as effective in removing disturbances from all recorded signals. Additionally, the time domain representation highlights that the recorded signal's amplitude varies significantly from peak to peak. The bandpass filter stabilizes the output signal's amplitude relative to the input, while it diminishes the amplitude.

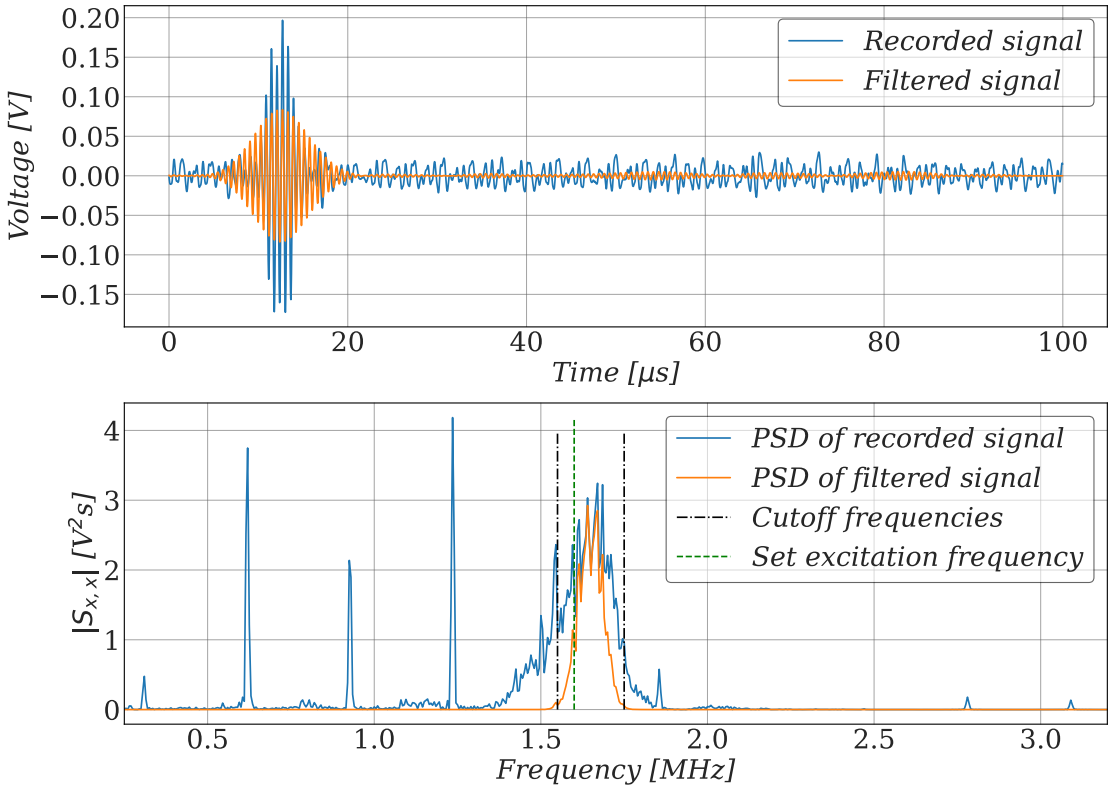

Fig. 5.10: Application of the designed Bessel-Thomson filter to a recorded signal. Results are depicted in both time and frequency domains. The burst's excitation frequency is $f_x = 1.6\,\text{MHz}$. All disturbances, including the one at $f = 1.54\,\text{MHz}$, are effectively eliminated.

5.2.3 Signal Processing Algorithm

This section describes the developed signal processing algorithm. After its implementation in *Python*, the algorithm was applied to most signals recorded during the experimental work of this master's thesis. However, for the wave velocity determination discussed in Section 6.3.1, a strategy based on cross-correlation was employed. Figure 5.11 illustrates the overall working principle of the designed signal processing algorithm. It shows step-by-step how the peak in the instantaneous amplitude is obtained from the raw measurement signal. The main steps are:

1. **Averaging of multiple measurements:** Calculate the average over 32 recorded signals at each point in time to improve the total signal-to-noise ratio (SNR). The measurement device automatically performs this calculation, and only the averaged signal is saved.
2. **Extraction of signal sequence for evaluation:** Discard the first $10\,\mu\text{s}$ of the averaged signal as the receiving channel of the measurement device experiences interference from the sending channel. Additionally, the time channel is capped at $t_{max} = 100\,\mu\text{s}$. This means the last $40\,\mu\text{s}$ of the averaged signal, which typically has a $t_{max} = 150\,\mu\text{s}$, are omitted. This selected signal sequence is referred to as the recorded signal throughout this thesis.

3. **Filtering:** Apply a Bessel-Thomson filter both forwards and backwards to eliminate systematic disturbances and noise.
4. **Calculating instantaneous amplitude:** Determine the analytic signal using the Hilbert transformation. Obtain the instantaneous amplitude from the analytic signal.
5. **Peak detection:** Calculate the expected arrival time interval of the SAW based on the known distance from the source and the identified wave velocity. Detect the peak in the instantaneous amplitude within this interval. Save both the peak amplitude and time for further evaluations.

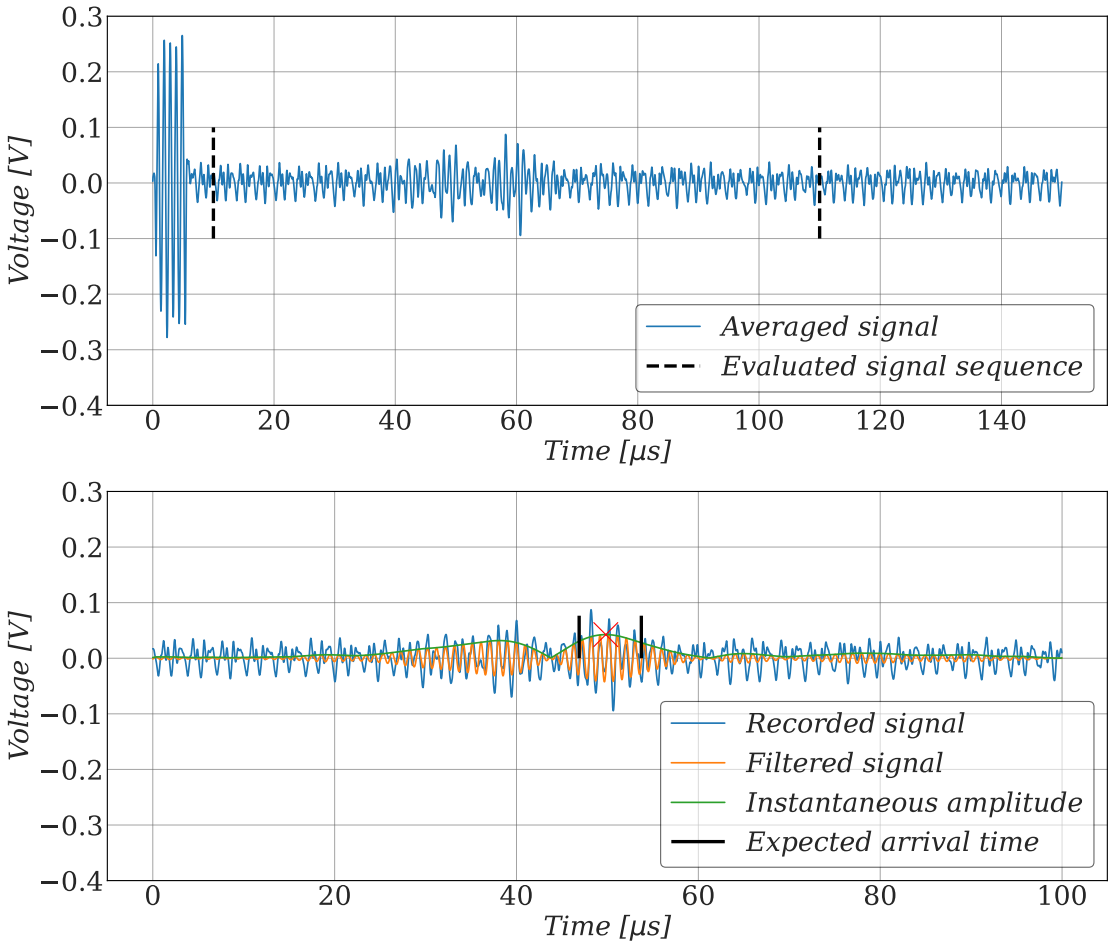

Fig. 5.11: Application of the developed signal processing algorithm to a measurement signal. The top diagram shows the averaged output from the measurement device. Only the relevant segment of this signal, termed the recorded signal, is evaluated. Using the known distance from the source and the wave velocity, an expected arrival time interval is determined. The peak is then detected in the filtered signal's instantaneous amplitude within this interval.

The developed signal processing algorithm is considered capable of extracting the desired feature from recorded signals in a reliable manner. In addition, other approaches for feature extraction were also identified during the design process. For example, the processing of recorded signals

could be based on cross-correlating them with software-generated bursts. The desired amplitude peaks are then detected in the correlation signal. In fact, this approach has the significant advantage that no filter is needed. However, it turned out that the coefficient of variation for the computed peak values is higher for this approach compared to the filter-based procedure. This can be explained by the influence of noise and perturbations. In particular, perturbations that occur at frequencies close to the set excitation frequency are only insufficiently attenuated.

Another potential method for determining a signal's envelope involves quadrature demodulation, also termed I-Q demodulation. Following this approach, the captured signal is simultaneously multiplied with a sinusoidal signal at the known carrier frequency and with its 90-degree phase-shifted counterpart. By employing an appropriate filter to extract the desired frequency components, the in-phase (I) and quadrature (Q) components of the signal are obtained [52, 53]. These components facilitate the calculation of the signal's envelope. Also, in this approach, deliberate filter tuning is necessary to obtain good results.

Chapter 6
Preliminary Investigations

This chapter begins with a brief overview of the laboratory measurement equipment. In addition, the conducted preliminary investigations are presented. Among the most crucial findings during these preliminary investigations was the necessity to gauge the surface acoustic wave (SAW) amplitude at multiple longitudinal positions to mitigate the influence of the rail surface on the signal amplitude. Furthermore, the velocity of the SAW when propagating through the examined rail grade was ascertained, facilitating the calculation of the interval for the expected time of arrival. Moreover, the attenuation of the SAWs was characterized.

6.1 Laboratory Measurement Setup

The measurement equipment that was used during all laboratory experiments consisted of a custom-made signal generation and measurement device, a piezoelectric transducer for exciting surface acoustic waves, and a Laser Doppler vibrometer (LDV) to determine the out-of-plane displacement induced by the propagating SAW. For simplicity, the signal generation and measurement device is hereafter referred to as the measurement device. Coaxial cables with BNC connectors served to connect the measurement device with the transducers and with the LDV. A detailed description of the laboratory measurement setup, illustrated in Figure 6.1, is provided in the following subsections.

6.1.1 Signal Generation and Measurement Device

For all measurements conducted during the experimental work of this thesis, a custom-made signal generation and measurement device was used. At its core is the commercially available USB Oscilloscope *Analog Discovery 2*, which is manufactured by the company *Digilent*. This oscilloscope is displayed in Figure 6.2(a). It features two input channels with a maximum sampling rate of $f_S = 100\,\text{MHz}$, along with a resolution of 14 bits, enabling the simultaneous capture of both the excited and received signals. Additionally, this oscilloscope is equipped with a signal generator

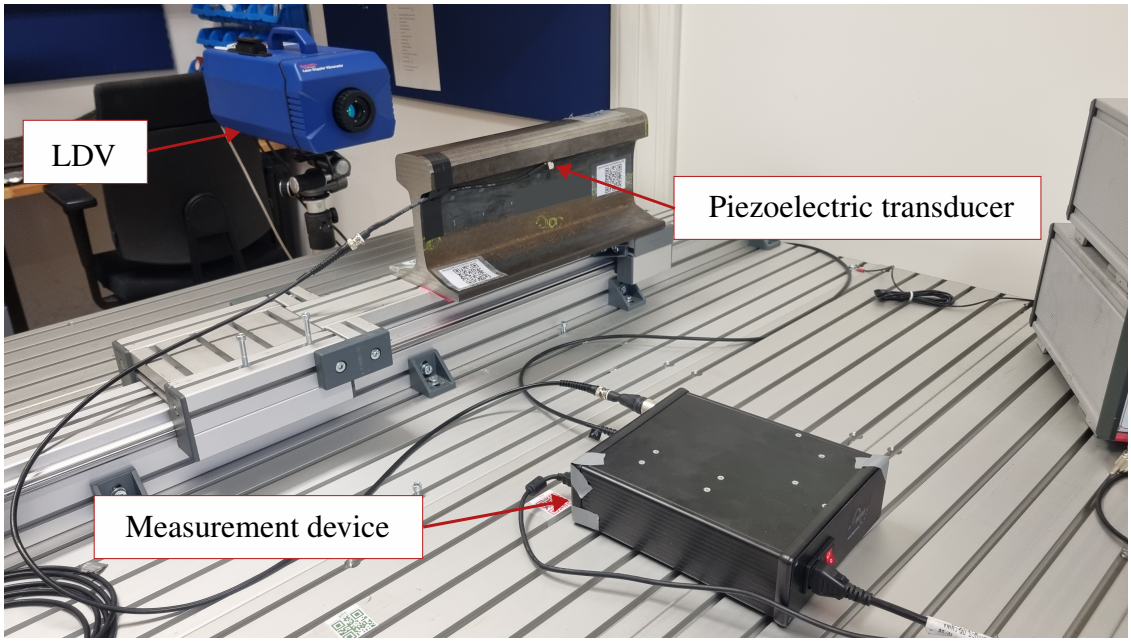

Fig. 6.1: The measurement equipment for the investigations on the influence of the crack depth on the SAW transmission coefficient includes a custom-made signal generation and measurement device, piezoelectric transducers attached to the bottom side of a sample's rail head, and a Laser Doppler vibrometer (LDV) to gauge the out-of-plane displacement.

capable of generating signals of arbitrary form [54]. Besides the oscilloscope, the measurement device incorporates electronic circuits to amplify the sending channel as well as the receiving channels [55]. A schematic overview of the amplification circuits is depicted in Figure 6.2(b).

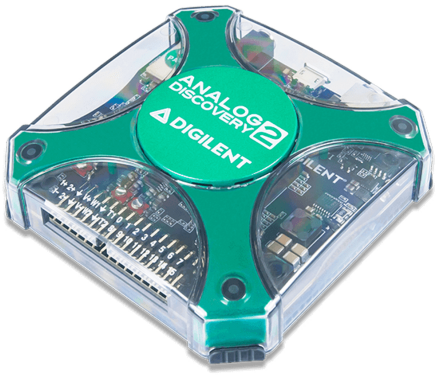

(a) Image of the USB oscilloscope, *Analog Discovery 2*, which forms the core of the measurement device [54].

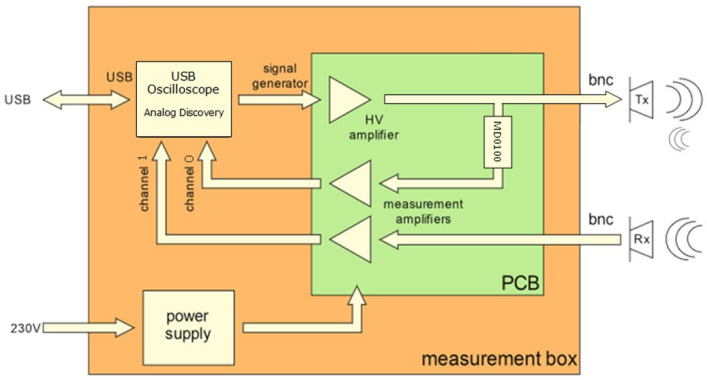

(b) Amplification circuit inside the measurement device. The output signal is amplified by a non-inverting operational amplifier. The receiving circuit consists of a buffer amplifier and an inverting operational amplifier [55].

Fig. 6.2: Employed hardware in the custom-made signal generation and measurement device.

Voltage signals generated with the USB oscilloscope are amplified by a non-inverting operational amplifier. The maximum output voltage of the *Analog Discovery 2* was set to $U = 2.0\,\mathrm{V}$ when performing the measurements. Based on theoretical calculations, a total output gain A of $A = 20.2$ was expected. The experimentally measured gain for an excitation frequency of $f_x = 1.0\,\mathrm{MHz}$ was slightly lower. A changing gain, dependent on the frequency, was recognized. The receiving circuit consists of a buffer amplifier to decouple the signal source from the measurement circuit and an inverting operational amplifier. Its gain was found to be $A = -18$. Amplification of the received signal is necessary since the output voltage of the LDV is very low [55]. However, the actual values of the amplification gains are of minor importance as the transmission coefficient is defined as the ratio of the transmitted wave amplitude to the incident wave amplitude.

The *Analog Discovery 2* has an interface to *Python* for code implementation. As a result, measurements can easily be executed automatically with the measurement device. The collected data is stored in *hdf5* files along with the metadata associated with the measurement. For the experiments presented in the following sections and in Chapter 7, a 5-pulse burst was used to avoid overlapping between surface wave oscillations and bulk wave oscillations. This is a signal consisting of five sinusoidal pulses. It was found that this signal shape offers a reasonable trade-off between high magnitude of excited SAWs in the time domain and a narrow bandwidth in the frequency domain.

6.1.2 Piezoelectric Transducers

The piezoelectric effect describes the electrical field which is generated by certain crystals when mechanical stresses are applied to them. This effect is also reversible as applying a voltage to these crystals causes them to deform. In principle, piezoelectric crystals facilitate the conversion between mechanical and electrical energy. Therefore, piezoelectric transducers can serve both as actuators and sensors [9, 56, 57].

Piezoelectric transducers of type *P-876.SP1*, manufactured by *PI Ceramic*, were employed for all conducted laboratory experiments. These transducers are based on lead zirconate-lead titanate material, a soft piezoceramic that contracts laterally when a voltage is applied [57]. This lateral contraction is highlighted in Figure 6.3. Throughout the experiments presented in this thesis, piezoelectric transducers were solely used to excite SAWs, while an LDV was employed to receive them. In contrast, any potential in-track installation of the measurement equipment would involve a dual-transducer setup to both excite and sense the SAWs.

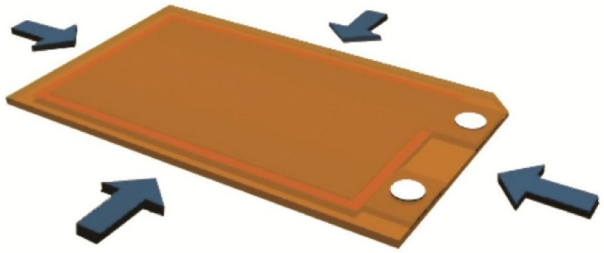

Fig. 6.3: The employed piezoelectric transducers of type *P-876.SP1*, manufactured by *PI Ceramic*, are contracting in lateral direction when a voltage is applied [57].

The piezoelectric transducers were affixed to the rails' surfaces with *HBM Z70* cold curing superglue. This type of adhesive is commonly used in engineering for attaching strain gauges [58]. A setup featuring a piezoelectric crystal oscillating in a lateral direction is elucidated in [9]. The author emphasizes that when coupled through a solid or highly viscous medium, such transducers induce shear bulk waves in addition to SAWs. The practical experience confirms this literature-based expectation. Indeed, it was observed that glued transducers also generate ultrasonic bulk waves in the specimens. The distinction between ultrasonic bulk waves and ultrasonic surface waves in the recorded signals was made based on time-of-flight, considering the different propagation velocities of these wave modes and the fact that bulk waves propagate through the material. Figure 6.4 illustrates a piezoelectric transducer that has been glued to the bottom side of a rail head.

Fig. 6.4: Piezoelectric transducer glued to the bottom side of a laboratory specimen's rail head.

6.1.3 Laser Doppler Vibrometer

A Laser Doppler vibrometer (LDV) relies on a laser beam to measure motions or vibrations such as the displacement caused by a propagating SAW [59]. Its measurement principle is fundamentally based on the physical phenomenon of the Doppler effect. According to the Doppler effect, the frequency of a wave gets shifted if the wave is reflected at a moving target. The shifted frequency

f' of the reflected wave can be calculated for the case of a target which is moving away from the fixed observer with velocity v by

$$f' = \frac{f}{1 + \frac{v}{c}}, \tag{6.1}$$

where the frequency of the incident wave is f. The wave velocity is denoted by c, which is equal to the speed of light in the case of a laser beam. Consequently, the velocity v of the object can be calculated from the measured frequency f', the known excitation frequency f, and the speed of light [56]. Although the frequency shift is marginal, as v is very small compared to the speed of light, it is still significant. Typically, an interferometer is deployed to quantify this minimal shift in practice. This method contrasts in a differential setup the reflected laser beam with an internal laser beam, whose frequency is known, enabling a very precise determination of the frequency shift. LDVs are employed in various engineering applications to gauge motions and vibrations, for example, in the modal analysis of automotive parts [56].

When propagating on a plane surface, a SAW's out-of-plane displacement is proportional to its in-plane displacement [28, 29]. Therefore, it is sufficient to measure only the out-of-plane displacement with an LDV to characterize the wave's amplitude.

For the laboratory experiments, a Laser Doppler vibrometer of type *OptoMET Nova Master* with velocity decoder *D-VD-5N* was used. This device was already shown in Figure 6.1. The LDV assessed the velocity of surface vibrations, induced by the SAW, rather than the actual surface displacement. However, the amplitudes from displacement and velocity deviate from each other by only a constant factor. Subsequently, this factor cancels out during the computation of the transmission coefficient when dividing the amplitude from the transmitted wave by the amplitude of the incident wave. Additionally, measuring the velocity amplitude is more precise, as it is by several orders of magnitude higher than the displacement amplitude. During the executed measurements, the measurement device was sampling from the analog signal output of the LDV. Before starting a new series of measurements, the LDV needs to be refocused.

6.2 Laser Doppler Vibrometer Measurement Error

It was already described in previous research, such as [60], that rail surface characteristics can exert a notable impact on laser-based measurements of the out-of-plane displacement of the surface. During preliminary experiments, two potential sources of systematic measurement errors were identified and investigated. The identified causes are as follows:

1. **Influence of refocusing:** After initial focusing of the LDV on the rail surface, which establishes a baseline signal level, subsequent refocusing at the same position can alter this level, either increasing or decreasing it. These variations were considered as a potential source of systematic measurement errors.

2. **Influence of the rail surface:** It was observed that the rail head outside of nearly all rail samples exhibited a slightly corroded surface. In contrast to the outside of the rail, the rail head's surface on the inside of the rail was still close to the initial as-rolled state. Figures 6.5(a) and 6.5(b), respectively, illustrate the surface on the inside and the outside of the rail head through photographs. The condition of the surface was suspected to influence the amplitude of the detected SAW.

(a) The rail head's surface on the inside of the rail was mostly close to the initial as-rolled state.

(b) The rail head's surface on the outside of the rail was mostly in a slightly corroded state.

Fig. 6.5: Surfaces on the inside and outside of the rail head. Discrepancies in surface conditions were observed across most examined rail specimens.

6.2.1 Influence of Refocusing

To examine the error due to LDV refocusing, SAWs were excited with a piezoelectric transducer affixed to the plane surface on the rail head inside. The LDV was focused on the rail head outside for gauging the surfaces' out-of-plane displacement caused by the propagating SAWs. With an excitation frequency of $f_x = 1.0\,\mathrm{MHz}$, $n = 100$ measurements were executed before the LDV was refocused. The measurement procedure was repeated two more times with another refocusing of the LDV in between. In total, $N = 300$ measurements were conducted to obtain three samples of peaks in the instantaneous signal amplitude, termed S_1, S_2, and S_3. These peak values were extracted from the measurement signals with the signal processing algorithm presented in Section 5.2.3. The histograms of these samples are illustrated in Figures 6.6 to 6.8. These figures also provide statistical parameters of the samples including the sample mean $\bar{x}$, the sample median Mdn, and the standard deviation σ. In addition, the sample mean $\bar{x}$ and median Mdn are indicated by vertical lines. The number of bins k was calculated according to Sturges' rule,

$$k = 1 + 3.322 \log N. \tag{6.2}$$

N is the total number of items in the sample [61]. The range and the bin width were set to be equal for all samples.

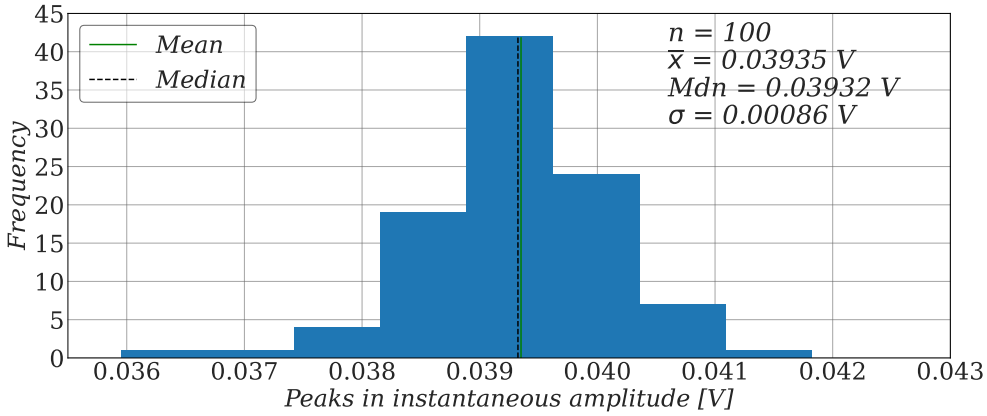

Fig. 6.6: Sample S_1 of peaks in the instantaneous signal amplitude, with statistical parameters including sample mean $\bar{x}$, median Mdn, and standard deviation σ provided. Vertical lines indicate the sample mean $\bar{x}$ and median Mdn.

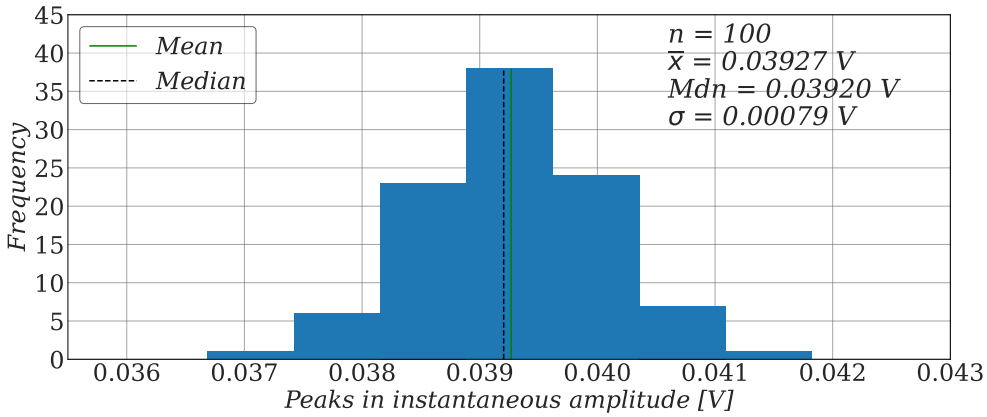

Fig. 6.7: Sample S_2 of peaks in the instantaneous signal amplitude.

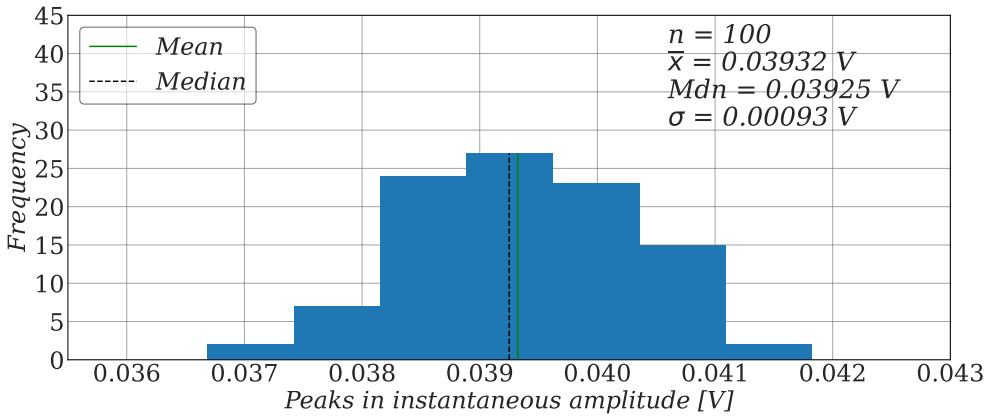

Fig. 6.8: Sample S_3 of peaks in the instantaneous signal amplitude.

As seen in Figures 6.6 to 6.8, $\bar{x}$ and Mdn remain largely unaffected when refocusing the LDV. Moreover, $\bar{x}$ and Mdn do not deviate significantly from each other for each sample. However, the standard deviation σ of the samples and the shape of the obtained frequency distributions vary slightly. To compare the samples, non-parametric statistical tests were applied as they do not presuppose that the samples come from a normal distribution. A Mood's median test was conducted. This test, which does not depend on the variances and shapes of the sampled distributions, is applicable to three samples concurrently [62]. The test hypothesis H_0 is defined as follows: The medians of the distributions from which the samples were drawn are identical [63]. The P-value of the test is provided in Table 6.1. H_0 is not rejected at a significance level $\alpha = 0.05$.

Table 6.1: Results from Mood's median test. H_0: The medians of the distributions from which the samples were drawn are identical. H_0 is not rejected at a significance level $\alpha = 0.05$.

Involved samples	S_1, S_2, S_3
P-value	0.5273

In addition to the median test, a Kruskal-Wallis test was performed to compare not only the medians but the overall distributions of the obtained values. The non-parametric Kruskal-Wallis test is similar to the Mann-Whitney U-test but allows for a comparison of three or more independent samples. Its test hypothesis H_0 states: The samples were drawn from identical distributions [64]. If equal shapes and variances of the sampled distributions are assumed, this test can also be used to test for different medians. Under the presumption of constant variances, the Kruskal-Wallis test has higher statistical power than Mood's median test [63].

The analysis was carried out collectively for all three samples, as well as individually for every possible combination of two samples. Although varying variances can significantly impact the Kruskal-Wallis test, the computed P-value for comparison of all three samples exceeds the P-value

of Mood's median test. In each case, H_0 is not rejected at a significance level $\alpha = 0.05$. The outcomes of the test procedure are summarized in Table 6.2.

Table 6.2: Results from Kruskal-Wallis tests. H_0: The samples were drawn from identical distributions. In each case, H_0 is not rejected at a significance level $\alpha = 0.05$.

Involved samples	S_1, S_2, S_3	S_1, S_2	S_1, S_3	S_2, S_3
P-value	0.7617	0.4430	0.7919	0.6886

To conclude, through the conducted non-parametric tests no statistical evidence was found to suggest that the distributions from which the samples were taken are not identical. Consequently, the supposed influence of LDV refocusing on the signal amplitude was not confirmed.

6.2.2 Influence of the Rail Surface

To examine the surface in initial condition on the inside of the rail head, a piezoelectric transducer was affixed to the plane surface on the rail head outside. The longitudinal reference position, $z = 0.0\,\text{mm}$, was defined to align with the center plane of the piezoelectric transducers. The SAW excited with $f_x = 1.0\,\text{MHz}$ was sensed by the LDV on the rail head inside after its propagation across the rail head. Measurements were performed at several slightly different longitudinal positions by varying z in $z \in \{-2.0\,\text{mm}, -1.0\,\text{mm}, -0.5\,\text{mm}, 0.0\,\text{mm}, 0.5\,\text{mm}, 1.0\,\text{mm}, 2.0\,\text{mm}\}$. At each position $m = 30$ measurements were conducted. The developed signal processing algorithm was applied to extract the peak in the instantaneous amplitude from the measurement raw data. Figure 6.9 depicts the histograms obtained for the selected measurement position. Since the travel distance d_{SAW} of the SAW propagating across the rail head $d_{SAW} > 90\,\text{mm}$, a longitudinal variation of the measurement distance $d = 2\,\text{mm}$ results in $\Delta d_{SAW} \ll 1\,\text{mm}$. Therefore, the increase in d_{SAW} can be neglected.

The bin parameters of the histograms in Figure 6.9 were set to be equal to those of Figure 6.10. It was found that the signal amplitude may deviate significantly from the overall average at certain z-positions. In particular, for measurements at $z = 0.0\,\text{mm}$, amplitude peaks with a considerably reduced mean but increased variance were observed. Moreover, the sample means were slightly higher than the overall average for $z = 0.5\,\text{mm}$ and $z = 1.0\,\text{mm}$. Therefore, the conclusion was drawn that even the rail surface in initial state can have a significant influence on the signal amplitude. Consequently, it is necessary to measure the SAW amplitude at a set of slightly different longitudinal positions to compensate for this influence.

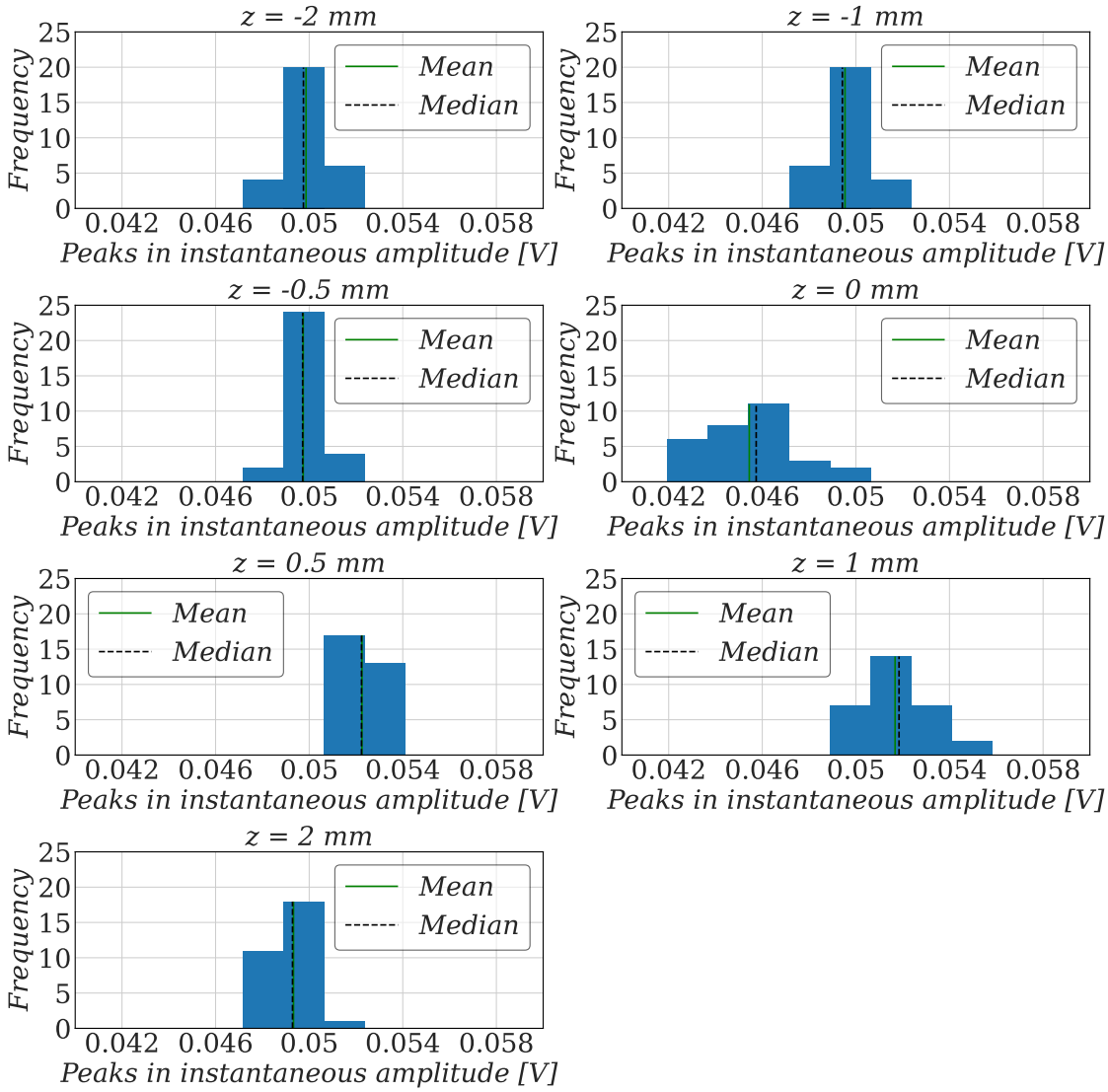

Fig. 6.9: Peaks in the instantaneous amplitudes from measurements at different z-positions on the rail head inside, representing a surface in its initial state, are shown. The SAW bursts were excited at a frequency of $f_x = 1.0\,\text{MHz}$. At each z-position, $n = 30$ measurements were executed. Notably, the amplitudes for $z = 0.0\,\text{mm}$ are significantly lower compared to all other z-positions, while the amplitudes for $z = 0.5\,\text{mm}$ and $z = 1.0\,\text{mm}$ are slightly elevated in contrast to the overall average. These observations underscore that the rail surface can influence the measured SAW amplitude, necessitating measurements at multiple nearby longitudinal positions to mitigate this effect.

To obtain the overall distribution of observed instantaneous amplitude peaks on the inside of the rail head, the results from the individual measurement positions were combined. Figure 6.10 shows the histogram of this collective sample on the rail head inside. Despite the proximity between the mean $\bar{x}$ and the median Mdn, this experimentally determined frequency distribution is evidently asymmetrical, attributed to its extended left tail. Additionally, a Shapiro-Wilk test for normality was performed. The test's P-value, displayed in Figure 6.10, also indicates a deviation from a Gaussian distribution even at significance level $\alpha = 0.01$.

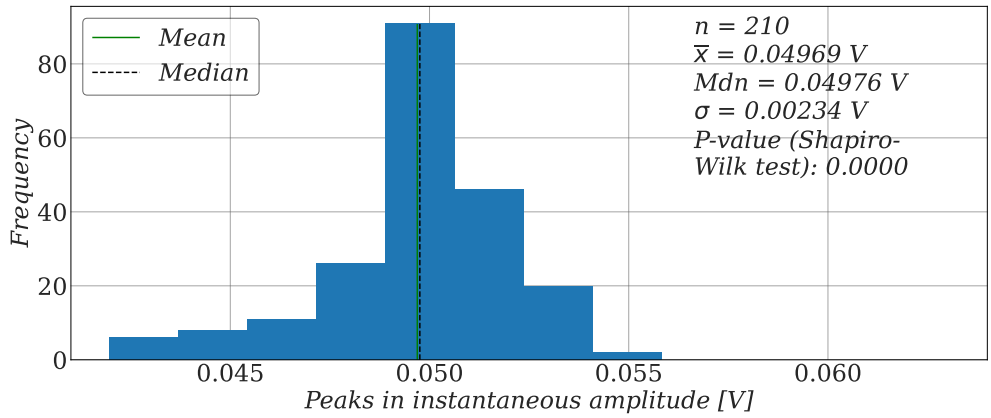

Fig. 6.10: Histogram of instantaneous amplitude peaks obtained from measurements at different z-positions on the rail head inside, representing a surface in its initial state. The SAW bursts were excited at a frequency of $f_x = 1.0\,\mathrm{MHz}$. It is evident from the histogram that the samples were not drawn from a Gaussian distribution. The P-value from a conducted Shapiro-Wilk test for normality, which is provided in the diagram, underlines this conclusion even for $\alpha = 0.01$.

The same procedure as for the surface in the initial state was applied to examine the slightly corroded surface on the rail head outside. Again, the signal amplitude was analyzed with $n = 30$ measurements at each of seven slightly different longitudinal positions. The overall distribution of the observed SAW amplitudes on the surface in slightly corroded state is depicted in Figure 6.11. This frequency distribution deviates only moderately from an ideal Gaussian from a purely visual point of view. In addition, the performed Shapiro-Wilk test reveals that this sample is not significantly different from a normal distribution at significance level $\alpha = 0.05$.

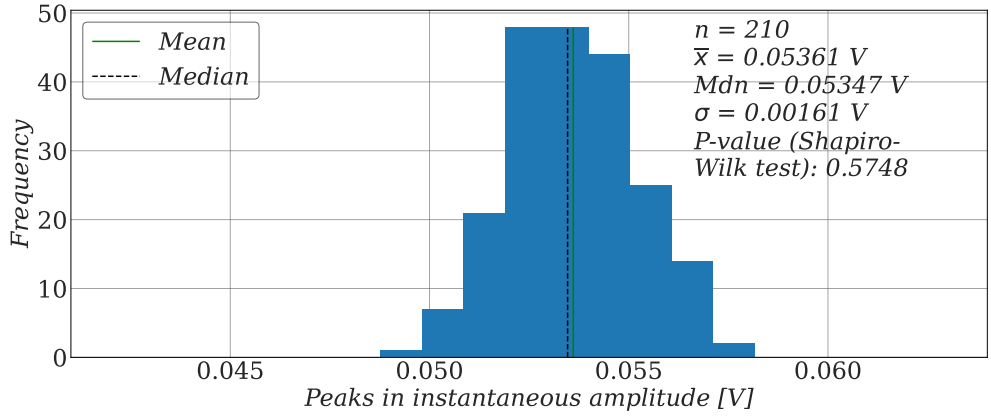

Fig. 6.11: Histogram of instantaneous amplitude peaks obtained from measurements at different z-positions on the rail head outside, representing a surface in a slightly corroded state. The SAW bursts were excited at a frequency of $f_x = 1.0\,\mathrm{MHz}$. From a visual inspection, this frequency distribution only moderately deviates from an ideal Gaussian. The performed Shapiro-Wilk test reveals that this sample is not significantly different from a normal distribution at significance level $\alpha = 0.05$.

While the frequency distribution of signal amplitudes leans towards a normal distribution when measuring the SAW on the slightly corroded surface, the results obtained on the surface in its initial state are clearly not normally distributed. An ideal normal distribution for the measurement results cannot be assumed in all cases. Furthermore, it was noted that measurements at certain exceptional positions on the rail surface can yield extraordinarily high or low SAW amplitudes. Therefore, measuring the SAW amplitude at several nearby positions is necessary to mitigate this effect.

6.3 Velocity and Attenuation of Surface Acoustic Waves Along the Rail Head

To characterize the velocity v and the attenuation behavior of SAWs propagating on the rail heads of the examined rail samples, measurements were conducted at the plane surface along rail head. An additional aim was to compare the inside and the outside of the rail head in terms of SAW velocity and attenuation. Consequently, two piezoelectric transducers were affixed to the head of the rail sample, with one positioned on the plane surface on the inside and the other on the plane surface on the outside of the rail. The SAW amplitude was measured at certain distances d from the edge of the transducers with the LDV. d was varied manually with a hand wheel in the range from $d_{min} = 20\,\text{mm}$ to $d_{max} = 300\,\text{mm}$ with steps of $\Delta d = 20\,\text{mm}$. The analyzed sample was of the same rail grade as the rail samples examined for the evaluation of the SAW transmission coefficient in Chapter 7. Figure 6.12 shows the piezoelectric transducer mounted at the inside of the rail head, with the LDV focused on the initial position $d = 0\,\text{mm}$.

The excitation frequency range was from $f_x = 0.7\,\text{MHz}$ to $f_x = 2.4\,\text{MHz}$, with increments of $\Delta f_x = 0.1\,\text{MHz}$. The entire f_x range was evaluated since the velocity determination is based on the arrival times of the SAW. Therefore, the amplitude height is of minor importance for the velocity determination. However, only measurements with $f_x \in \{0.7\,\text{MHz}, 1.0\,\text{MHz}, 1.3\,\text{MHz}, 1.6\,\text{MHz}, 1.9\,\text{MHz}, 2.2\,\text{MHz}\}$ were taken into account for the characterization of the attenuation curve to avoid interference of the actual signal amplitude with the systematic perturbations described in Section 5.1. For each combination of f_x and d, $n = 3$ measurements were executed. Only for the rail head inside and $d > 180\,\text{mm}$, the number of repetitions was reduced to $n = 2$. The influence of the rail surface was neglected during these preliminary investigations.

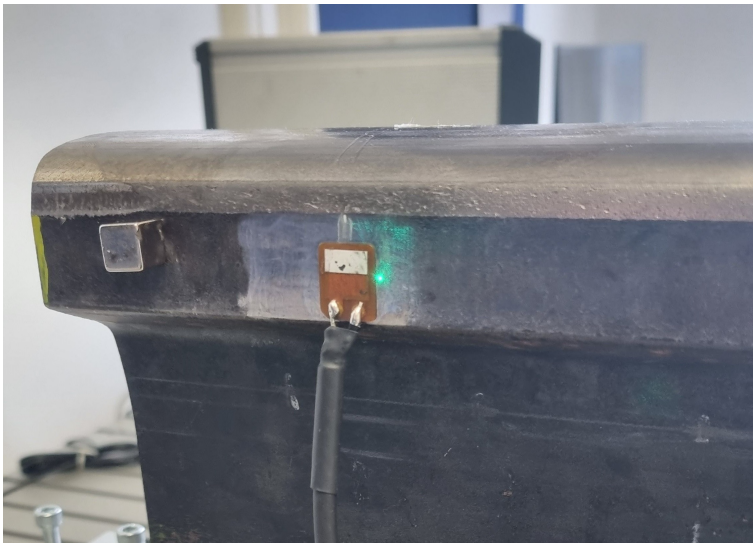

Fig. 6.12: Experimental setup to characterize the velocity v and the attenuation behavior of SAWs propagating on the rail head: The piezoelectric transducer was affixed to the inside of the rail head. A green laser indicates the LDV's sensing position at the time the photograph was captured. The illustrated setup represents a distance d from the edge of the piezoelectric transducer $d = 0\,\text{mm}$. Measurements were performed within the distance range from $d_{min} = 20\,\text{mm}$ to $d_{max} = 300\,\text{mm}$ with increments of $\Delta d = 20\,\text{mm}$.

6.3.1 Velocity Determination

The calculation of the SAW velocity v on the rail head relied on detecting the arrival times of the SAW at specific distances d. To determine the surface waves' arrival times, the cross-correlation of the recorded signals s_i with a software-generated 5-pulse burst termed s_G was computed. This procedure yields more distinct peaks in the correlation signals compared to those obtained by computing the cross-correlation with another measurement signal. Computing the cross-correlation with this ideal sinusoidal signal eliminates most perturbations from the resulting cross-correlation signals. Given the lag of the cross-correlation peak, the time interval of s_i to have the maximum overlap with reference signal s_G can be determined. The arrival time t_i of the SAW burst recorded in signal s_i has been defined to be centered in this interval. Figure 6.13 illustrates this method for extracting the SAW arrival time t_1 from the signal s_1, recorded at a distance $d_1 = 20\,\text{mm}$ from the transducer.

Subsequently, the velocity v of the SAW was computed based on the arrival times t of the SAW at certain distances d from the piezoelectric transducer. In addition, the time offset t_0 was determined. This time offset was caused by delays in the measurement electronics and by the cropping of the recorded signals.

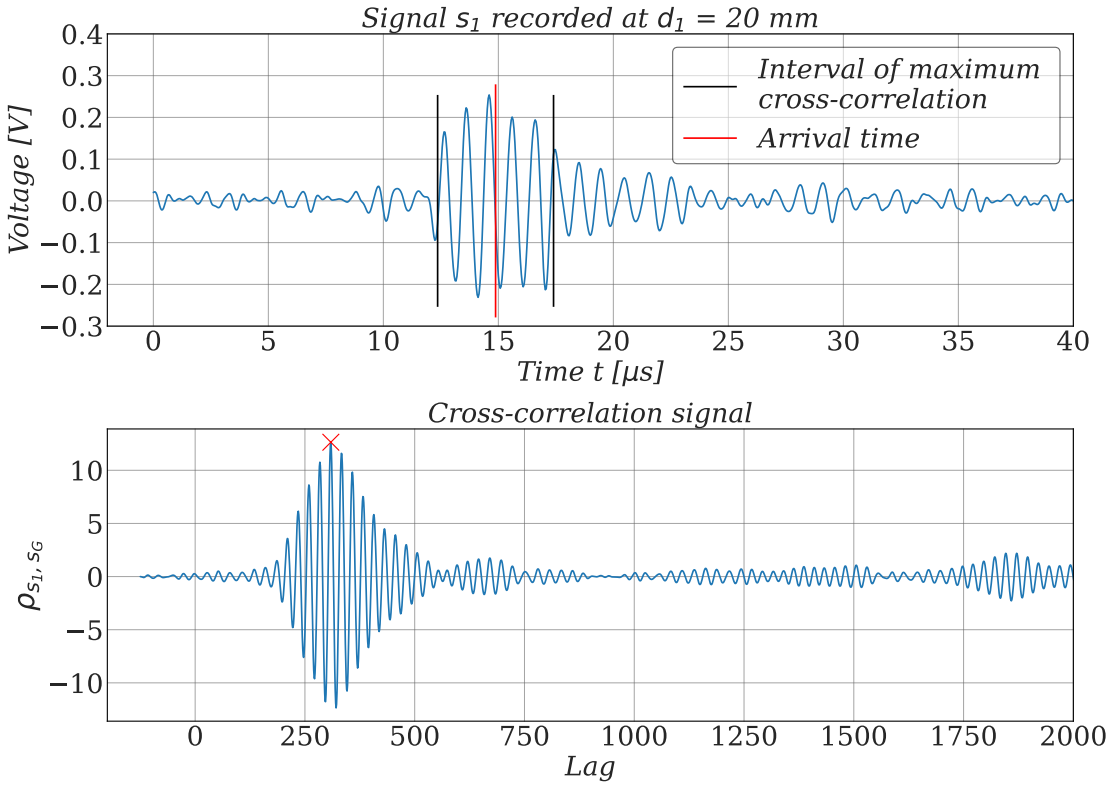

Fig. 6.13: The upper diagram depicts the recorded signal s_1. To determine the SAW's time of arrival in signal s_1, it is cross-correlated with a software-generated signal s_G consisting of five sinusoidal pulses. The cross-correlation signal ρ_{s_1,s_G} is illustrated in the lower chart. A red cross indicates the peak in the cross-correlation signal. The time interval of maximum cross-correlation is computed from this peak. The arrival time of the SAW burst is centered in this interval.

Using this applied procedure, arrival times t_i were identified at fixed distances d_i. As a result, d was regarded as the independent and t as the dependent variable. Therefore, a simple linear regression model was deployed, which is defined as

$$t = \beta_0 + \beta_1 d + \varepsilon. \tag{6.3}$$

In this context, the model parameter β_1 represents the reciprocal value of the velocity, $1/v$. β_0 is the sum of the time offset t_0 and the half duration of the SAW pulse, 0.5 t_{Pulse}, resulting in $\beta_0 = t_0 + 0.5\, t_{Pulse}$. The random error of a certain measurement is denoted by ε. The determined arrival times t of the SAWs with $f_x = 0.8\,\text{MHz}$ have been plotted over the distance d from the piezoelectric transducer in Figure 6.14. In addition, the regression line is illustrated and the computed values for v and t_0 are provided.

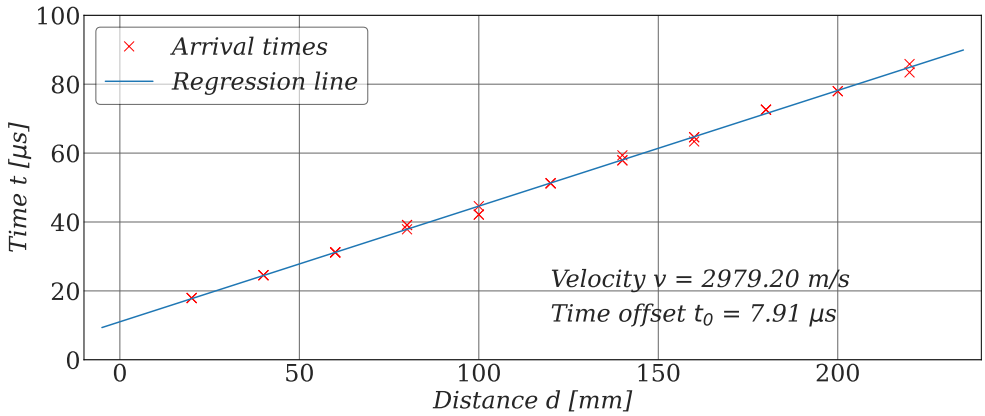

Fig. 6.14: Arrival times t of SAW pulses excited with f_x = 0.8 MHz plotted against the distance d from the exciting piezoelectric transducer on the inside of the rail head. Linear regression was applied to compute the SAW velocity v and the time offset t_0. The slope of the regression line β_1 represents the reciprocal value of the velocity, $1/v$. It is important to note that the intercept β_0 corresponds to the sum of t_0 and the half duration of the SAW pulse, 0.5 t_{Pulse}.

In general, it was observed that bulk wave reflections tend to interfere more significantly with the SAW for low f_x and high d, resulting in a less accurate determination of the arrival times. Consequently, only measurements conducted at $d \leq 220\,\text{mm}$ were considered for the computation of the SAW velocity. Figure 6.15 displays the trend of the Rayleigh wave velocity v across the excitation frequency f_x, while Figure 6.16 depicts the trend of the time offset t_0 across the excitation frequency f_x. These trends were evaluated on both the rail head inside and on the rail head outside. The 95% confidence intervals (CI) on the best fit values of v and t_0 for a certain f_x are displayed.

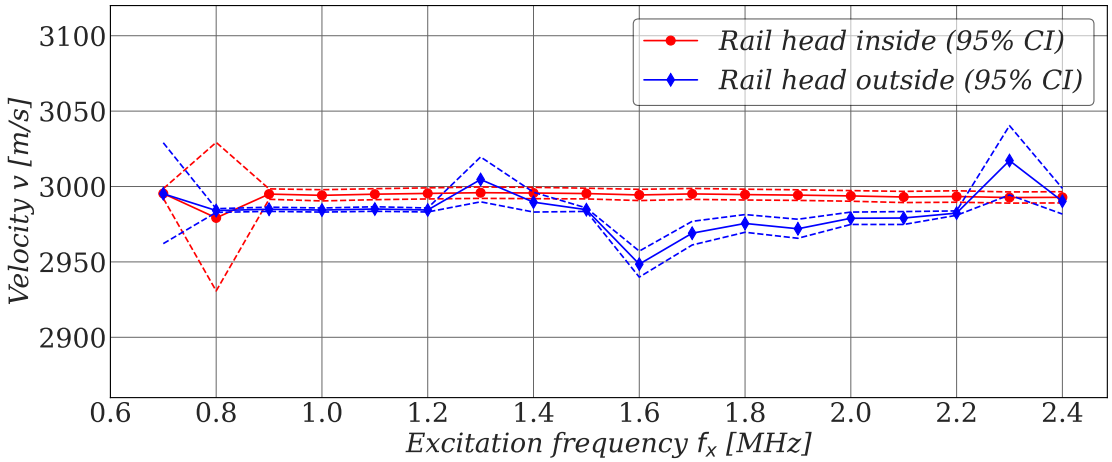

Fig. 6.15: Trend of the SAW velocity v over the excitation frequency f_x on the inside and the outside of the rail head. The 95% confidence intervals (CI) on v for a certain f_x are provided. Although v exhibits unsystematic variations with f_x on the outside of the rail head, the deviation of the highest computed velocity v_{max} from the lowest velocity v_{min} is below 3%.

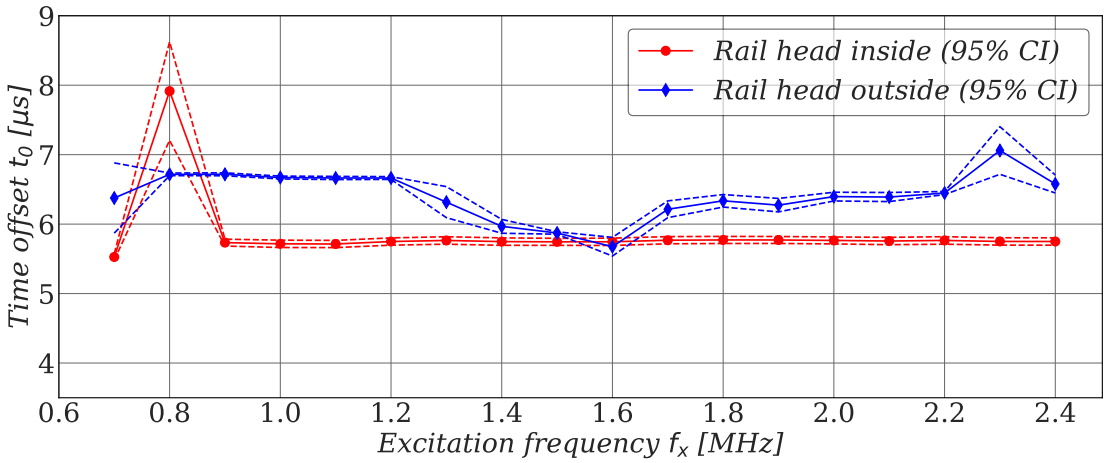

Fig. 6.16: Trend of the time offset t_0 over the excitation frequency f_x on the inside and the outside of the rail head. Different constant time offsets for the inside and the outside can be explained by small variations in the initial measurement position. t_0 exhibits unsystematic variations on the outside of the rail head, similar to the determined trend of the velocity.

Overall, the measured velocities align well with the estimation of the Rayleigh wave velocity computed in Section 3.1. The SAW velocity v is approximately constant on the inside of the rail head for $f_x > 0.8\,\mathrm{MHz}$. This corresponds to the anticipation of a frequency-independent SAW velocity v. Contrary to the inside of the rail head, v exhibits unsystematic variations with f_x on the outside of the rail head. An explanation for this finding still remains to be found. However, the deviation of the highest computed velocity $v_{max} = 3017\,\mathrm{m/s}$ from the lowest velocity $v_{min} = 2948\,\mathrm{m/s}$ is below 3%, which is still regarded as a reasonable precision. These velocities were determined on the outside of the rail head for $f_x = 1.6\,\mathrm{MHz}$ and $f_x = 2.3\,\mathrm{MHz}$, respectively.

As seen in Figure 6.16, an outlier in the time offset t_0 on the rail head inside is identified for $f_x = 0.8\,\mathrm{MHz}$. This can be explained by the fact that the rail surface keeps oscillating for a significantly longer duration at low f_x compared to high f_x. Therefore, less distinct peaks are found in the cross-correlation signal, which affects the accuracy of the determined values for v and t_0. Nonetheless, the time offset t_0 on the inside of the rail head is nearly perfectly constant besides this outlier. Similar to the determined trend of the velocity, a constant offset time t_0 was observed on the rail head outside in the range from $f_x = 0.8\,\mathrm{MHz}$ to $f_x = 1.2\,\mathrm{MHz}$ and from $f_x = 1.7\,\mathrm{MHz}$ to $f_x = 2.2\,\mathrm{MHz}$. These different constant time offsets for the inside and the outside can result from small variations in the initial measurement position. Outside of these f_x ranges, also t_0 on the rail head outside shows unsystematic variations. If the described outlier on the rail head inside is neglected, the maximum deviation Δt_0 is smaller than $1.5\,\mu\mathrm{s}$.

The developed signal processing algorithm presented in Section 5.2.3 relies on a time interval centered at the computed expectation of the arrival time to detect the peaks in the instantaneous amplitude of the SAW. v and t_0 were determined with sufficient precision to guarantee reliable identification of the SAW in the measurement signals.

6.3.2 Fitting the Attenuation Curve

The signals used for the velocity determination were also assessed to characterize the SAW attenuation behavior. In this context, the developed signal processing algorithm was applied to extract the peaks from the instantaneous amplitude of the recorded signals. Given these amplitude peaks of the SAW at specified distances from the transducer, a non-linear least squares fit was employed to approximate these amplitudes with the model function

$$A(d) = C\frac{\mathrm{e}^{-\alpha d}}{\sqrt{d}}, \tag{6.4}$$

as derived in Section 3.2. Figure 6.17 illustrates the peaks obtained in the instantaneous amplitude for $f_x = 1.0\,\mathrm{MHz}$ across the examined distance range, together with the fitted function.

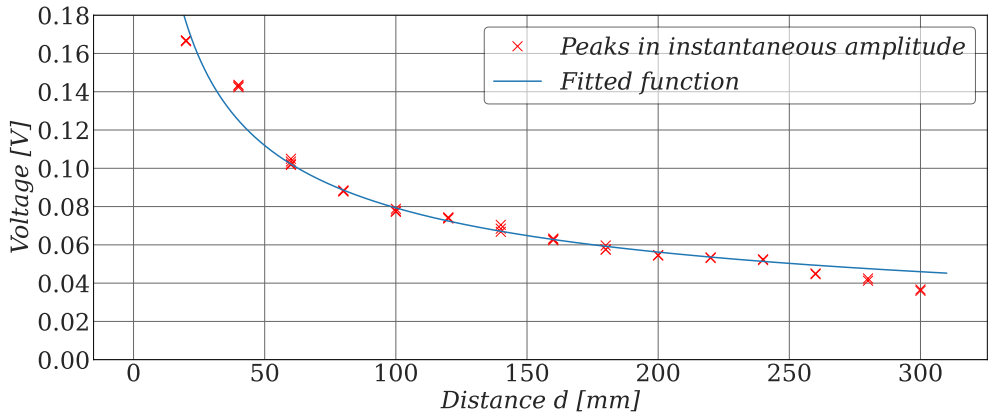

Fig. 6.17: Peaks in the instantaneous amplitude plotted over the distance d from the transducer for the full range of d. The measurements were performed on the rail head inside with $f_x = 1.0\,\mathrm{MHz}$. The function $A(d)$ provided in Equation 6.4 was fitted to these amplitude values. The fitted function deviates significantly from the measured values for $d < 60\,\mathrm{mm}$ and $d > 240\,\mathrm{mm}$.

Figure 6.17 clearly indicates that the fitted function deviates significantly from the measured values for $d < 60\,\mathrm{mm}$ and $d > 240\,\mathrm{mm}$. Potential reasons for this deviation could be the near-field effects for low d or that the employed model was derived for SAWs propagating at an ideal plane surface. As a result, the evaluated distance was limited to the range of $d_{min} = 60\,\mathrm{mm}$ to $d_{max} = 240\,\mathrm{mm}$. However, even when taking only this limited distance range into account, the 95% confidence interval on the model parameter α for the measurements conducted on the rail head inside at $f_x = 1.0\,\mathrm{MHz}$ evaluated to

$$-1.16 \times 10^{-4} mm^{-1} \leq \alpha \leq 1.61 \times 10^{-4} mm^{-1}.$$

Based on this confidence interval, it was concluded that α is poorly conditioned as it is not significantly different from zero. Therefore, the model function was modified by excluding the exponen-

tial term. Additionally, the fixed exponent of d was replaced by a model parameter b to characterize the rate of the amplitude decay. In contrast to a theoretical surface wave propagating at a plane surface where $b = 1/2$, b evaluates for an ideal bulk wave to $b = 1$. The model function ultimately employed is given by

$$A(d) = C\frac{1}{d^b}. \tag{6.5}$$

The final attenuation model function allows for a straightforward interpretation. The model parameter C specifies the initial wave amplitude, since $A(d)$ at $d = 1\,\text{mm}$ evaluates to $A(d = 1) = C$ for any b. Thus C represents the energy of the excited SAW. In addition, for a particular C, the model parameter b determines the rate at which the amplitude of the SAW diminishes as distance d increases. Subsequently, the distance d beyond which the amplitude has been attenuated by a specific percentage is dependent on b. It is important to note that Equation 6.5 is considered as an appropriate model only for $d \gg 0\,\text{mm}$.

Taking the natural logarithm of Equation 6.5 leads to

$$\ln A = \ln C - b \ln d, \tag{6.6}$$

which is basically the same type of mathematical function as the general linear regression model

$$y = \beta_0 + \beta_1 x + \varepsilon. \tag{6.7}$$

Consequently, as a first approximation, the logarithmic attenuation curve can be fitted to the logarithmized peaks in the instantaneous amplitude by employing linear regression. This approach facilitates the simple calculation of confidence intervals for both the regression line and the observation [65, 66]. However, it is important to note that the computed results can only be regarded as an approximation since the assumptions of linear regression analysis, such as independent and identically normally distributed errors, are only partially satisfied [65].

The trend of the peaks in the instantaneous amplitude over distance d for $f_x = 1.0\,\text{MHz}$ is provided in Figure 6.18 as a chart with a logarithmic scale on both axes. In this representation, the obtained signal amplitudes appear to lie on a straight line, thereby enabling the application of linear regression. The computation was performed with *Python's statsmodels* package, which fits the linear model by using the ordinary least squares method. The 95% confidence interval and the 95% prediction interval are illustrated.

Although the function described in Equation 6.5 is regarded as the best conceivable physics-based model for the attenuation of a SAW on a plane surface, slight systematic errors are suspected. For instance, at $d = 120\,\text{mm}$ and $d = 140\,\text{mm}$, five out of six measurement values are significantly higher than the mean of the regression line at the respective d. Systematic errors cannot be excluded as the number n of conducted measurements at each d is not sufficiently high. To characterize the

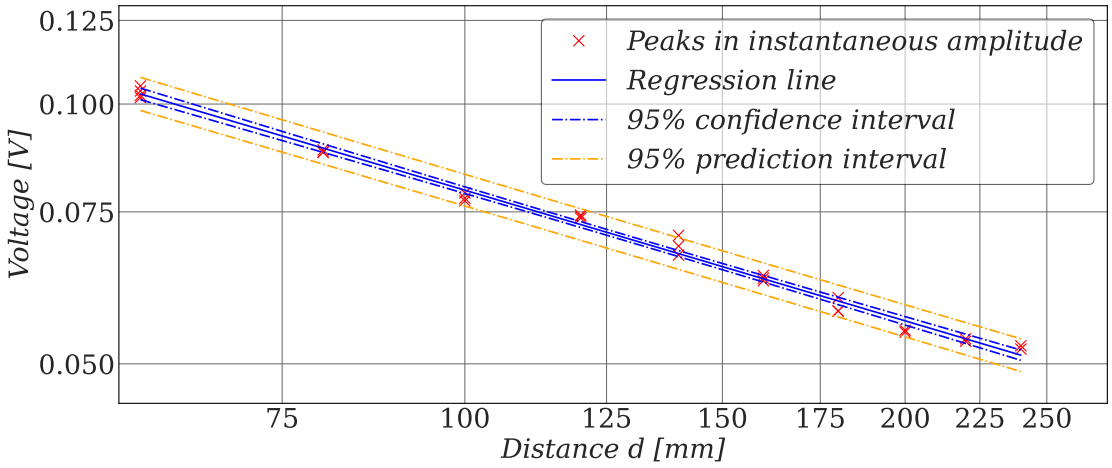

Fig. 6.18: Plot of peaks in the instantaneous amplitude versus distance d for $f_x = 1.0\,\text{MHz}$ with a logarithmic scale on both axes. The model function for attenuation, as described in Equation 6.5, was fitted to the amplitude peaks using linear regression. Both the 95% confidence interval and the 95% prediction interval are illustrated.

mean and the standard deviation at each specific d value, approximately $n \approx 25$ measurements at each measurement position would have been necessary [67]. Nonetheless, the developed model $A(d)$ for the attenuation curve can still be deployed for a qualitative comparison of the attenuation at different excitation frequencies f_x.

6.3.3 Evaluation of the Attenuation Curve

The linear scale fit of the attenuation curve depicted in Figure 6.19 was obtained by taking the antilog of the regression line which had been fitted to the logarithmized signal amplitudes. The same procedure was applied to both the confidence interval and the prediction interval to quantify the uncertainty of the fitted curve.

To investigate the influence of the excitation frequency f_x on the SAW's attenuation, the curve fitting procedure was applied to measurements on the inside and on the outside of the rail head with $f_x \in \{0.7\,\text{MHz}, 1.0\,\text{MHz}, 1.3\,\text{MHz}, 1.6\,\text{MHz}, 1.9\,\text{MHz}, 2.2\,\text{MHz}\}$. The 95% confidence intervals (95% CI) on the parameters C and b of the attenuation model were computed explicitly by means of non-linear fitting with the *lmfit* package. The best fit values of C and the respective 95% CI on C are plotted across the evaluated excitation frequencies f_x in Figure 6.20. It was found that the systematic errors of the model function described in the previous subsection are particularly pronounced for $f_x < 1.0\,\text{MHz}$. This leads to a high uncertainty of the model parameters C and, in particular, b for these f_x.

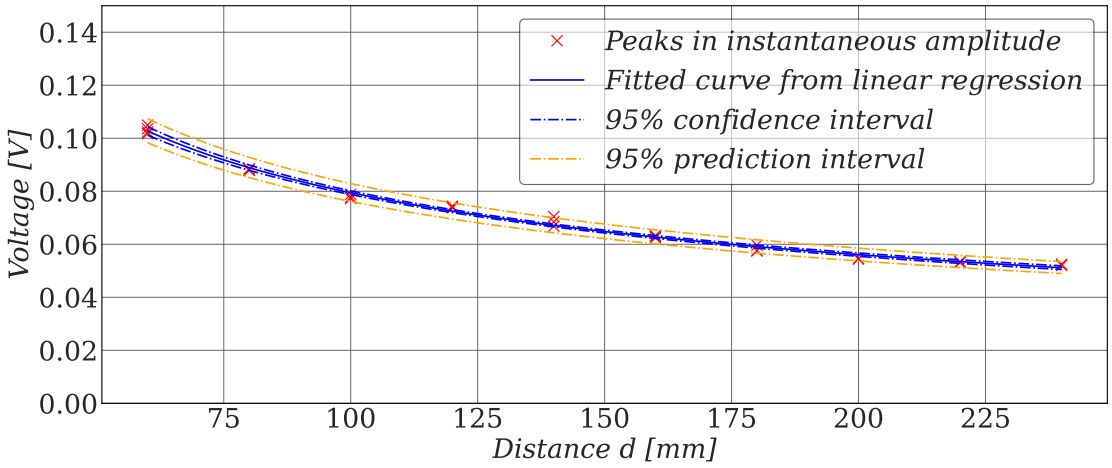

Fig. 6.19: Linear scale plot of peaks in the instantaneous amplitude versus distance d for $f_x = 1.0\,\text{MHz}$. The model function for the attenuation, as described in Equation 6.5, was fitted to the amplitude peaks using linear regression. Both the 95% confidence interval and the 95% prediction interval are illustrated.

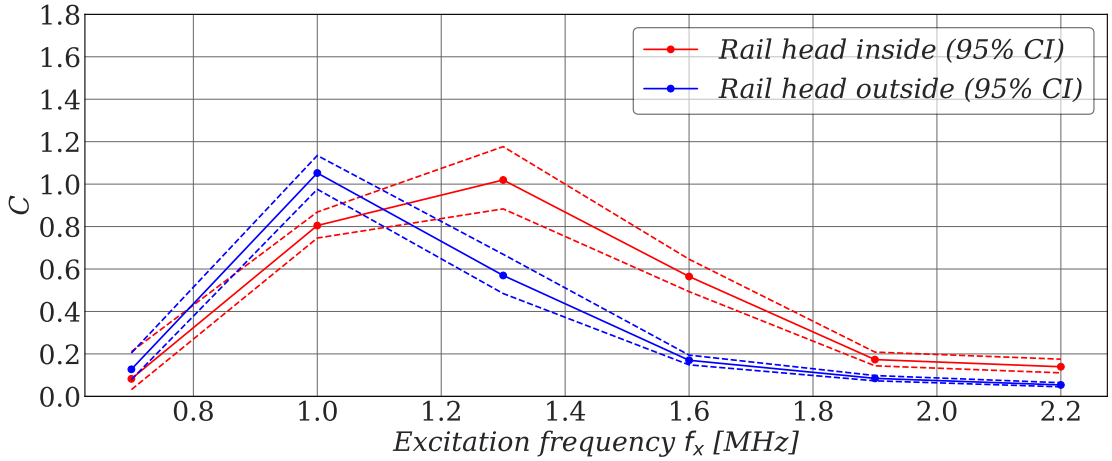

Fig. 6.20: Trend of the model parameter C across the evaluated excitation frequencies f_x. Dots mark the computed values of C. Linear interpolation was applied between these discrete f_x values. The 95% confidence intervals on C are provided. This model parameter represents the initial SAW's amplitude and can therefore be interpreted as the energy input to the system. A maximum is observed in the range from $f_x = 1.0\,\text{MHz}$ to $f_x = 1.3\,\text{MHz}$.

In general, the trend of C over f_x on the inside of the rail head aligns well with the one determined for the rail head outside. The highest amplitude of the initial SAW, which is represented by C, was identified in the range from $f_x = 1.0\,\text{MHz}$ to $f_x = 1.3\,\text{MHz}$. However, the exact location of the maximum can vary from one transducer to another. This difference is presumably caused by the piezoelectric transducers themselves or the glue used for affixing them. C, and thereby the energy of the excited SAW, continuously decreases with f_x for $f_x > 1.3\,\text{MHz}$. Consequently, the excitation frequency f_x cannot be increased arbitrarily with the measurement device and transducers used.

Indeed, the examination of the experiments on the SAW transmission coefficient, presented in Chapter 7, reveals that $f_x \leq 1.6\,\mathrm{MHz}$ is necessary to achieve a sufficiently high signal amplitude at the receiver when measuring across the rail head.

To compare the attenuation of the SAW at different f_x, the model parameter b was normalized with the respective best fit value of C due to the frequency dependency of C. The trend of b/C over f_x is displayed in Figure 6.21. Linear interpolation was applied between the computed values of b/C, which are marked by dots. Additionally, the 95% confidence intervals on b/C are provided.

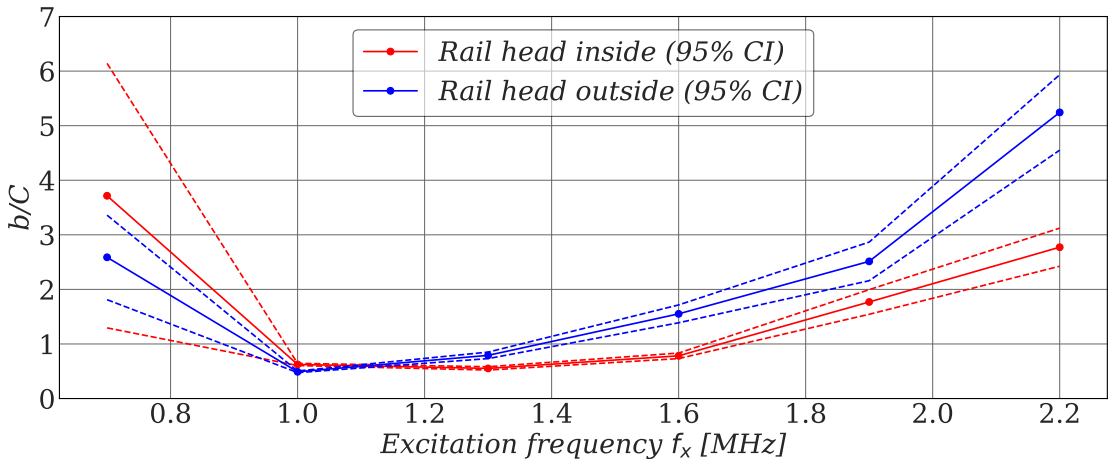

Fig. 6.21: Trend of the model parameter b normalized with the respective best fit value of C across the evaluated excitation frequencies f_x. Dots mark the computed values of b/C. Linear interpolation was applied between these discrete f_x values. The 95% confidence intervals on b/C are provided. This model parameter indicates how fast the amplitude fades with distance. In general, the attenuation of the SAW is increasing with rising f_x. The bulk waves interfere significantly with the SAWs for $f_x = 0.7\,\mathrm{MHz}$, explaining the high uncertainty at this f_x.

As seen in Figure 6.21, b/C shows tremendous uncertainty for $f_x = 0.7\,\mathrm{MHz}$. This is, as already explained, because the used model function exhibits a systematic error for this f_x. Nonetheless, for $f_x \geq 1.0\,\mathrm{MHz}$, b/C smoothly increases with rising f_x, which corresponds well with the frequency dependency of the attenuation described in certain literature, such as [9]. The increased attenuation on the rail head outside is potentially due to the slightly corroded surface on this side of the rail head.

Chapter 7
Experimental Determination of the Transmission Coefficient

This chapter describes the measurements performed to determine the transmission coefficient of the surface acoustic wave (SAW) on the rail samples being examined. This is done for varying head check depth a to investigate the correlation between the SAW transmission coefficient and the head check depth. Based on the obtained results, the SAW transmission coefficient can be potentially employed for quantitative depth assessment of head checks with a depth a up to $a = 590\,\mu\text{m}$. Furthermore, the mechanisms that impede accurate determination of the depth of more pronounced head checks are identified.

7.1 Experimental Setup

Six different rail samples were examined, each of the same pearlitic steel grade and with a length $l = 40\,\text{cm}$. The cross-section of these specimens corresponded to the standard rail profile 60E1 [68]. These rail samples varied only in terms of the number of load cycles N they had been subjected to: $N \in \{20000, 50000, 75000, 125000, 200000, 300000\}$. In Figure 7.1, the rail sample with $N = 125000$ is depicted. The rail specimens were obtained after test runs on a full-scale rail wheel test rig designed to investigate the emergence of head check damage. The loading conditions during the test runs may have varied for each specimen. The test rig design is described in detail in [69].

In the initial stages of a new test run, significant alterations occur in the surface roughness of a rail's running band since the wheel is in contact with this area during the test run. SAWs are known to be sensitive to changes in surface conditions, as evidenced by both the available literature [9] and practical experience. Consequently, a rail sample with $N = 20000$ was used as the undamaged reference instead of an entirely new rail. The specimen with $N = 50000$ exhibited only a few head checks, which were identified by means of thermography. All specimens subjected to $N \geq 75000$ load cycles showed continuous head check bands, which were clearly visible. The head check damage of the specimen with $N = 125000$ is displayed in Figure 7.2.

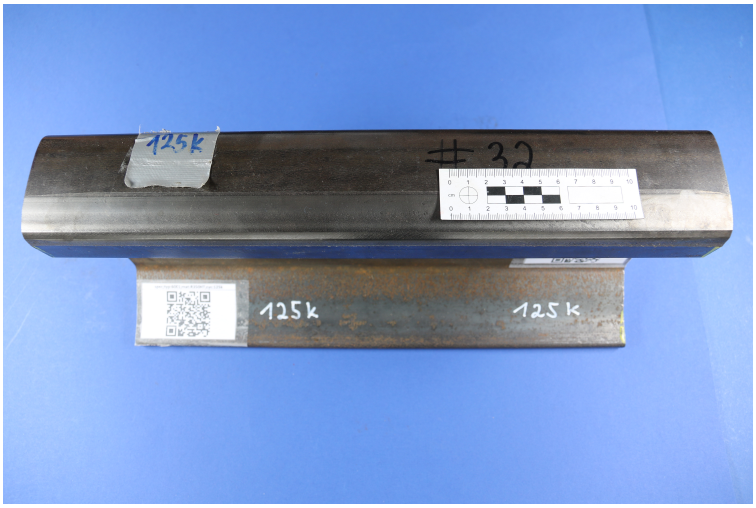

Fig. 7.1: Rail sample subjected to $N = 125000$ load cycles, exhibiting clearly visible head check damage.

The depth of the head checks was determined by metallographic examination after the measurements of the SAW transmission coefficient had been finished. It turned out that a rising number of load cycles N does not necessarily lead to an increase in the maximum crack depth a.

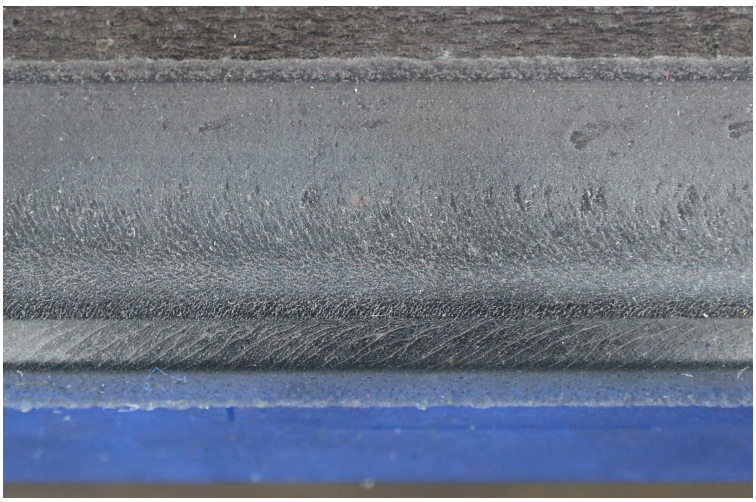

Fig. 7.2: Head check damage on the rail sample subjected to $N = 125000$ load cycles. A continuous head check band was observed.

For surface acoustic waves propagating over a surface breaking crack, the transmission coefficient C_T is defined as

$$C_T = \frac{A_T}{A_I}, \tag{7.1}$$

where A_T and A_I denote the amplitude of the transmitted surface wave and the incident surface wave, respectively [29, 35]. The theoretical trend of the transmission coefficient for an ideal surface breaking crack was already illustrated in Figure 3.2(a) in Section 3.3. It was decided to mea-

sure the amplitude of the transmitted wave with the Laser Doppler vibrometer (LDV), because this was considered as the most reliable method available. Additionally, the amplitude of the incident wave was also gauged with the LDV, as the adhesive and the geometric positioning of the piezoelectric transducer can influence the amplitude of the incident wave. In contrast to these laboratory experiments, one cross-section with permanently installed transducers would experience increasing damage in a possible in-track application. Therefore it has to be emphasized that a slightly varying incident wave amplitude from one transducer to another is not considered as problematic for in-track applications, if the aging process of the adhesive used is well understood.

The piezoelectric transducers were placed on the bottom side of the rail head as the SAW arrives separately from the bulk waves at the measurement positions for this configuration. In contrast to the laboratory setup, the transducers need to be affixed to the rail's web to avoid being destroyed while tamping in a potential in-track application. However, the goal of this thesis was to evaluate the fundamental correlation between the SAW transmission coefficient and the head check depth. Therefore, an installation on the bottom side of the rail head was preferred, since this configuration also leads to an increased signal-to-noise ratio (SNR).

As illustrated in Figure 7.3, the LDV was focused at a vertical distance $d_v = 10\,\text{mm}$ from the lower edge of the rail head when measuring the transmitted wave amplitude. The incident wave amplitude was determined at a vertical distance $d_v = 15\,\text{mm}$ from the lower edge to increase the geometrical distance from the SAW exciting transducer. In both cases, the laser's axis was perpendicular to the rail surface. The surface acoustic wave had to propagate over a distance $d_I = 21\,\text{mm}$ from the transducer's edge to reach the measurement position for the incident wave amplitude. Moreover, the SAW had to travel across the rail head for a distance $d_T = 125\,\text{mm}$ to arrive at the measurement position for the transmitted wave amplitude. The developed signal processing algorithm computes the SAW burst's expected time of arrival based on these geometrical distances.

The transducers were affixed to the inside of the rail head, as seen in Figure 7.3, for the conducted experiments. While it is also possible to position the transducer on the outside of the rail head, this would inevitably result in measuring the amplitude of the transmitted wave only shortly after the SAW has been affected by the head checks. As a result, the influence of the head check near-field may be significant. This theoretical argumentation was confirmed by preliminary measurements, which revealed that this hypothetical setup leads to a substantially wider range for the measured transmission coefficients compared to the employed setup with the transducers on the rail head inside.

At this point, a coordinate system is introduced to provide a precise description of the employed measurement setup. The z-axis aligns with the longitudinal direction of the rail. The position $z = 0$ is defined to coincide with the affixed piezoelectric transducers' center plane. This position is also referred to as the reference position. For most specimens, the transducers were positioned exactly in the longitudinal center plane of the rail itself. Consequently, the rail's longitudinal center plane aligned with $z = 0$ and the distance from the reference position to the left and the right side face of

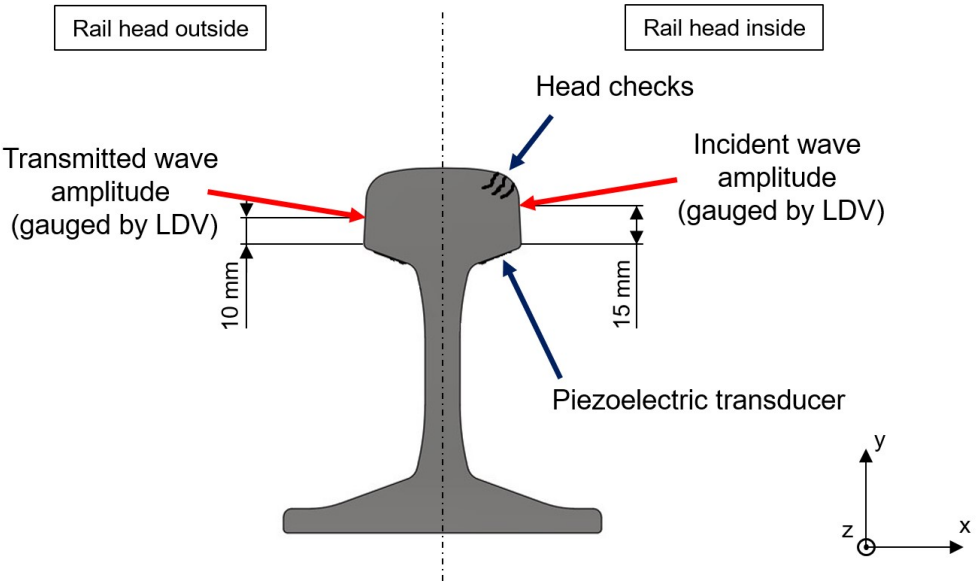

Fig. 7.3: Schematic illustration of the experimental setup for investigating the correlation between the SAW transmission coefficient C_T and the head check depth a. The amplitudes of the incident and the transmitted wave are gauged by the LDV. Measurements were conducted at proximate yet distinct positions along the rail's z-axis to compensate for the influence of the rail surface.

the rail was equal. Only for the rail sample with $N = 50000$, the piezoelectric transducer was not placed in the center plane of the rail, as this specimen did not show a continuous head check band. The transducer was affixed to this rail sample with its center plane having a distance s to the rail's side plane of $s = 52\,\text{mm}$. This position was chosen in order to avoid an overlap of the SAW burst with bulk waves reflected at the rail's side plane.

The amplitude measured at a certain position can be significantly influenced by the surface at this position, as already pointed out in Section 6.2. To compensate for this influence of the surface structure, both the incident wave amplitude and the transmitted wave amplitude were measured at $m = 7$ different, yet close-by, positions. The lateral coordinate z_I of the measurement position was varied in $z_I \in \{-1.0\,\text{mm}, -0.5\,\text{mm}, -0.2\,\text{mm}, 0.0\,\text{mm}, 0.2\,\text{mm}, 0.5\,\text{mm}, 1.0\,\text{mm}\}$ when measuring the incident wave amplitude. z_T was varied in $z_T \in \{-2.0\,\text{mm}, -1.0\,\text{mm}, -0.5\,\text{mm}, 0.0\,\text{mm}, 0.5\,\text{mm}, 1.0\,\text{mm}, 2.0\,\text{mm}\}$ when measuring the transmitted wave amplitude. The x- and y-coordinates of the measurement positions were left unchanged. At each of these $m = 7$ measurement positions, $j = 20$ measurements were conducted for each combination of specimen and excitation frequency f_x. In total, $n = 140$ measurements were performed on each side of the rail head for a given specimen and f_x. Only for the rail sample with a number of load cycles $N = 20000$, the amplitudes were measured at a reduced set of measurement positions: $z_I \in \{-1.0\,\text{mm}, -0.5\,\text{mm}, 0.0\,\text{mm}, 0.5\,\text{mm}, 1.0\,\text{mm}\}$; $z_T := z_I$. Consequently, $n = 100$ measurements were conducted for each f_x on each side of the rail head for this single specimen.

The excited SAW burst consisted of 5 sinusoidal pulses. This voltage signal was generated by the measurement device, described in Section 6.1.1, and excited via the piezoelectric transducers. The excitation frequency of the generated burst signals varied in a range from $f_x = 0.7\,\text{MHz}$ to $f_x = 1.9\,\text{MHz}$ with steps of $\Delta f_x = 0.3\,\text{MHz}$. The measurements were performed sequentially with one LDV. After the measurements of the incident wave amplitude were finished, the specimen was rotated by 180 degrees around its y-axis and the measurements of the transmitted wave amplitude were initiated.

7.2 Evaluation

All recorded measurement signals were processed with the developed signal processing algorithm, which is highlighted in Section 5.2.3. This algorithm extracts the peak in the SAW's instantaneous amplitude from the measurement signals. $n = 140$ measurements were performed for each combination of rail sample and excitation frequency. The histograms of the amplitudes of the incident and transmitted waves are depicted in Figure 7.4 and Figure 7.5, respectively. These distributions of observed values were obtained on the specimen with $N = 75000$ and an excitation frequency $f_x = 1.0\,\text{MHz}$. The bin count was determined using Sturges' rule, as provided in [61]. Further details on its definition can also be found in Section 6.2.1. Moreover, these figures contain statistical parameters of the observed samples, including the sample mean $\bar{x}$, the sample median Mdn, the standard deviation σ, and the coefficient of variation CV, which is computed by $CV = \sigma/\bar{x}$. In addition, the sample mean $\bar{x}$ and median Mdn are indicated by vertical lines. It is preferred to characterize these samples by Mdn rather than $\bar{x}$ as they are non-symmetric and do not follow a Gaussian distribution.

The experimentally determined distribution of the transmitted wave amplitude has a significantly lower median than that of the incident wave. Indeed, only a part of the energy of the incident SAW is transmitted as a SAW when hitting a surface breaking crack [31]. Additionally, the propagation across the rail head results in an attenuated SAW amplitude due to absorption and geometrical decay. Notably, the coefficient of variation CV is substantially higher for the amplitude of the transmitted wave. Presumably, this is due to the slightly corroded state of the surface on the rail head outside.

Determining the empirical distribution of the transmission coefficient, as provided in Equation 7.1, requires dividing the experimentally determined distribution of the transmitted amplitude by that of the incident amplitude. However, from a statistical point of view, even the division of two Gaussian distributions is not a favorable operation, since the calculation of the ratio leads to the heavy-tailed Cauchy distribution if the random variables are uncorrelated and follow a zero-mean Gaussian distribution [70]. If these conditions are not met, the resulting distribution may also have

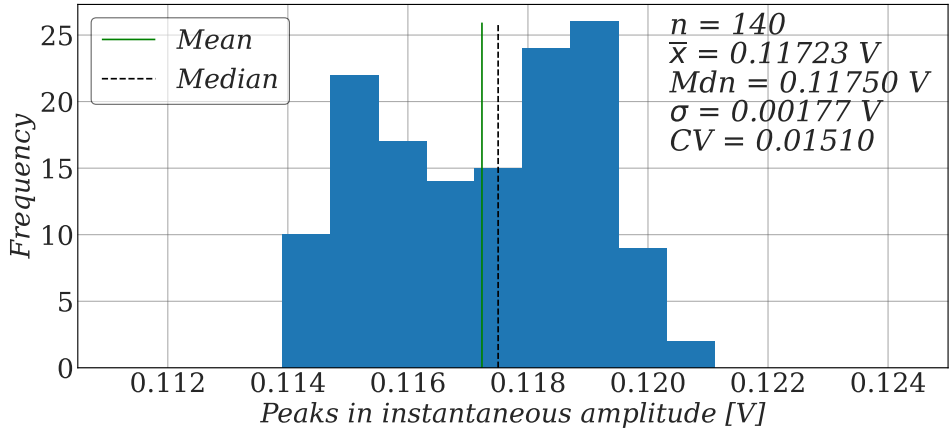

Fig. 7.4: Histogram of the peaks in the instantaneous amplitudes of the incident waves from measurements conducted on the rail specimen with $N = 75000$ at an excitation frequency $f_x = 1.0\,\text{MHz}$. The statistical parameters including the sample mean $\bar{x}$, the sample median Mdn, the standard deviation σ, and the coefficient of variation CV are given. In addition, $\bar{x}$ and Mdn are indicated by vertical lines.

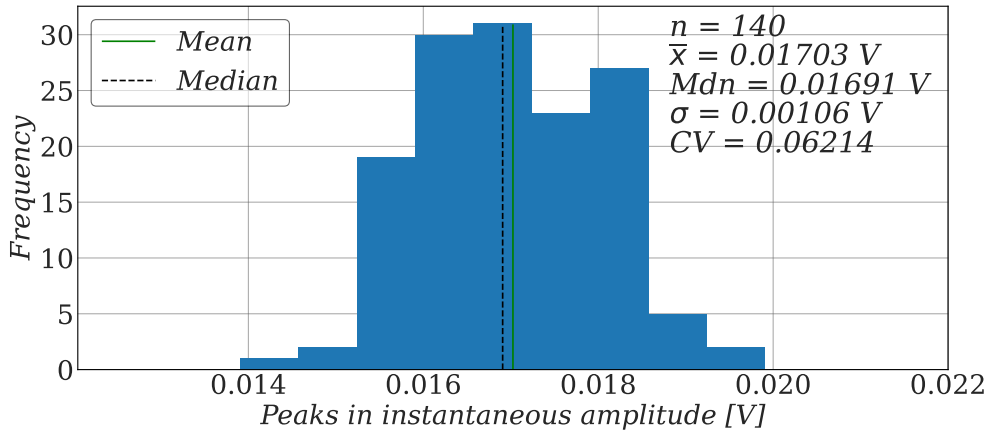

Fig. 7.5: Histogram of the peaks in the instantaneous amplitudes of the transmitted waves from measurements conducted on the rail specimen with $N = 75000$ at an excitation frequency $f_x = 1.0\,\text{MHz}$.

a bimodal and asymmetric shape. In contrast, the result of adding or subtracting two Gaussian distributions is also Gaussian, if the respective random variables are uncorrelated [67, 71, 72].

As Figure 7.4 and Figure 7.5 demonstrate, the distributions of observed values for the incident wave amplitude and the transmitted wave amplitude are not Gaussian. An empirical method was therefore employed, approximating the distribution of the transmission coefficient by individually dividing each obtained value of the transmitted amplitude by each value of the incident amplitude. This methodology aligns with techniques applied in Monte-Carlo simulations [73]. Figure 7.6 showcases the experimentally determined distribution of the transmission coefficient for the

rail specimen with $N = 75000$ and an excitation frequency f_x = 1.0 MHz. Using this procedure, a sample size of $n = 19600$ for the transmission coefficient was achieved. It is noteworthy that the CV is only marginally higher for the computed values of the transmission coefficient compared to the sample of the transmitted wave amplitudes.

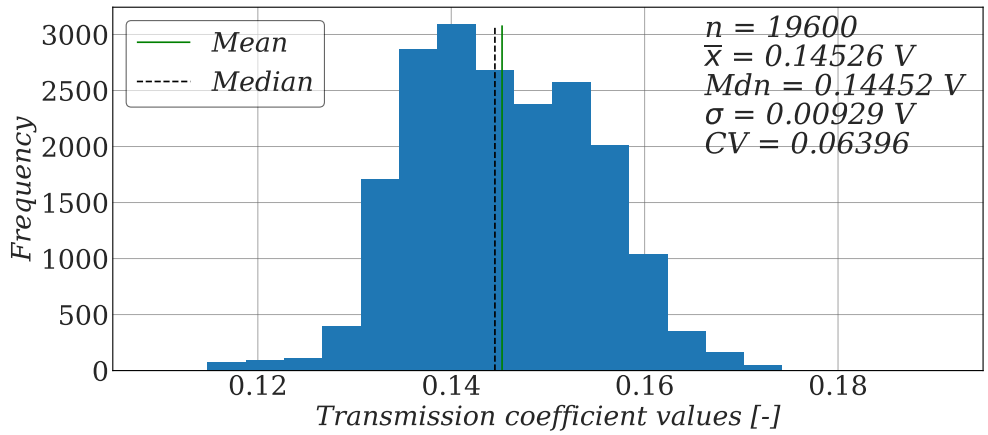

Fig. 7.6: Histogram of the transmission coefficient C_T on the rail specimen with $N = 75000$ at an excitation frequency f_x = 1.0 MHz. This distribution of observed values was obtained by individually dividing each obtained value of the transmitted amplitude by each value of the incident amplitude.

Intrinsic factors, such as internal absorption and diffraction at grain boundaries, in addition to geometrical decay, attenuate the SAW besides the scattering at cracks. This affected the ascertained transmission coefficients as the transmitted wave amplitude was not measured directly after the crack. Consequently, all experimentally determined distributions of the transmission coefficient were normalized using the computed median from the undamaged specimen, which evaluated as $Mdn = 0.4248\,\mathrm{V}$ for the excitation frequency $f_x = 1.0\,\mathrm{MHz}$. This normalization facilitates a comparison between the transmission coefficients obtained at different f_x values. Figure 7.7 displays the histogram depicting the normalized transmission coefficient values observed on the rail specimen subjected to $N = 75000$ load cycles and at an excitation frequency of $f_x = 1.0\,\mathrm{MHz}$.

Following the SAW measurements, the rail samples were subjected to a detailed microstructural examination to determine the maximum depth a of the head checks. Micrographs were captured at the position $z = 0$, which corresponded to the rail sample cross-sections where the SAW transmission coefficients had been measured in advance. Figure 7.8 displays illustrations of the microstructure, captured using an optical microscope. Figure 7.8(a) shows the head check found in the cross-section of the rail sample with a load cycles count of $N = 50000$. This specimen only exhibited a single head check with a depth $a = 394\,\mu\mathrm{m}$. In contrast, the specimen with $N = 300000$

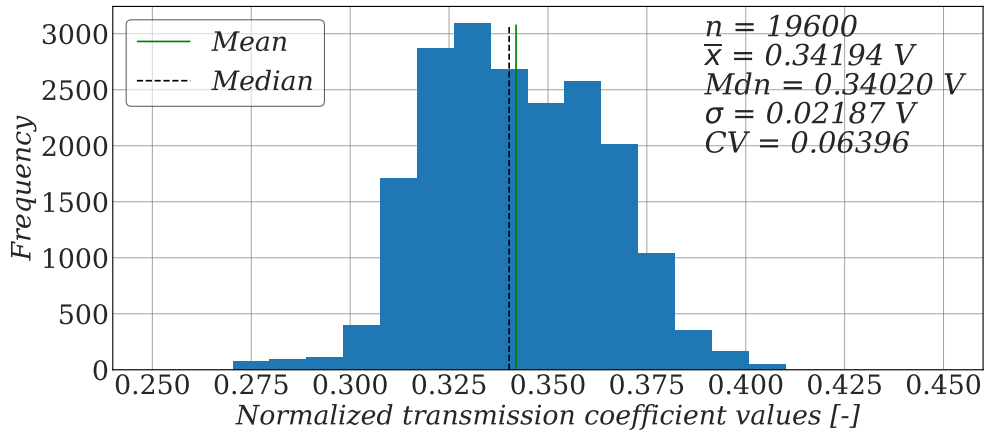

Fig. 7.7: Histogram of the normalized transmission coefficient C_T on the rail specimen with $N = 75000$ at an excitation frequency $f_x = 1.0\,\text{MHz}$.

revealed $k = 3$ cracks in the analyzed cross-section, as shown in Figure 7.8(b), with a maximum crack depth $a = 592\,\mu\text{m}$. All results from the metallographic examination including the maximum crack depth a of the head checks and the number of head checks k are provided in Table 7.1. The specimens are sorted by the number of load cycles N. The specimen with $N = 200000$ exhibited the highest maximum crack depth $a = 852\,\mu\text{m}$. The largest number of cracks, $k = 5$, was identified in the specimens with $N = 75000$ and $N = 125000$.

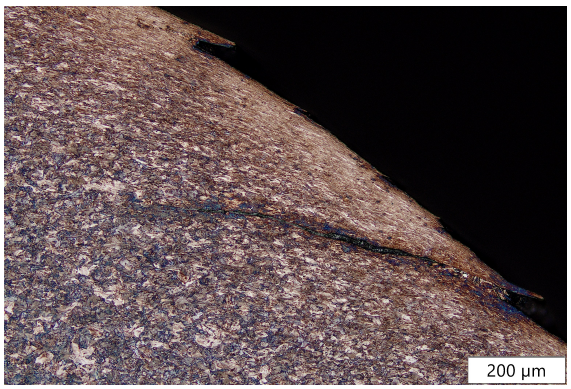

(a) Micrograph of the rail specimen subjected to $N = 50000$ load cycles, showing the identified head check, captured at 100x magnification. This specimen exhibited only a single head check with a depth $a = 394\,\mu\text{m}$.

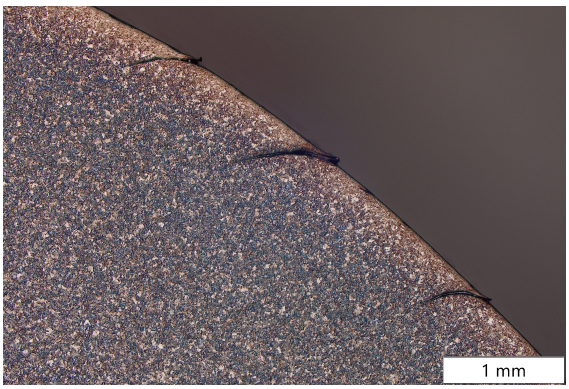

(b) Micrograph of the rail specimen subjected to $N = 300000$ load cycles, showing the identified head checks, captured at 25x magnification. This specimen exhibited three head checks, with a maximum crack depth $a = 592\,\mu\text{m}$.

Fig. 7.8: Micrographs captured using an optical microscope during the metallographic examination of the rail samples.

It was ascertained that a rising number of load cycles N does not necessarily lead to an increase in the maximum crack depth a or in the number of cracks k. This finding arises from the fact that

the specimens were obtained from different test runs at the rail-wheel test rig, each with varying loading conditions. Through thermographic analysis, it was determined that other crack parameters, such as length, angle, and crack spacing, did not exhibit significant deviations across all specimens with a load cycle count of $N \geq 75000$.

Table 7.1: Results from the metallographic examination of the investigated rail samples. The specimens are sorted by the number of load cycles N. The table provides the maximum crack depth a of the head checks and the number of head checks k.

Specimen number	Load cycles N	Maximum crack depth a [μm]	Number of cracks k
1	20000	0	0
2	50000	394	1
3	75000	777	5
4	125000	660	5
5	200000	852	4
6	300000	592	3

7.3 Results and Discussion

In Figure 7.9 the evolution of the transmission coefficient C_T in relation to maximum crack depth a is shown for the evaluated excitation frequencies f_x. These trends were identified by evaluating all measurements taken at each excitation frequency for each specimen, following the methodology outlined in the preceding subsection. However, measurements at $f_x = 1.9\,\text{MHz}$ were excluded due to the low Signal-to-Noise Ratio (SNR) at this frequency. The medians of the experimentally determined transmission coefficient distributions are denoted by dots, and vertical lines indicate the interquartile range (IQR) of the distributions of observed transmission coefficient values.

The observed high-level trends conform to the theoretically computed transmission coefficient for a single, ideal surface-breaking crack, as depicted in Figure 3.2(a). The overall pattern reveals a gradual decline in the transmission coefficient, succeeded by a sharp decrease, and ultimately leading to a saturation phase where C_T stabilizes.

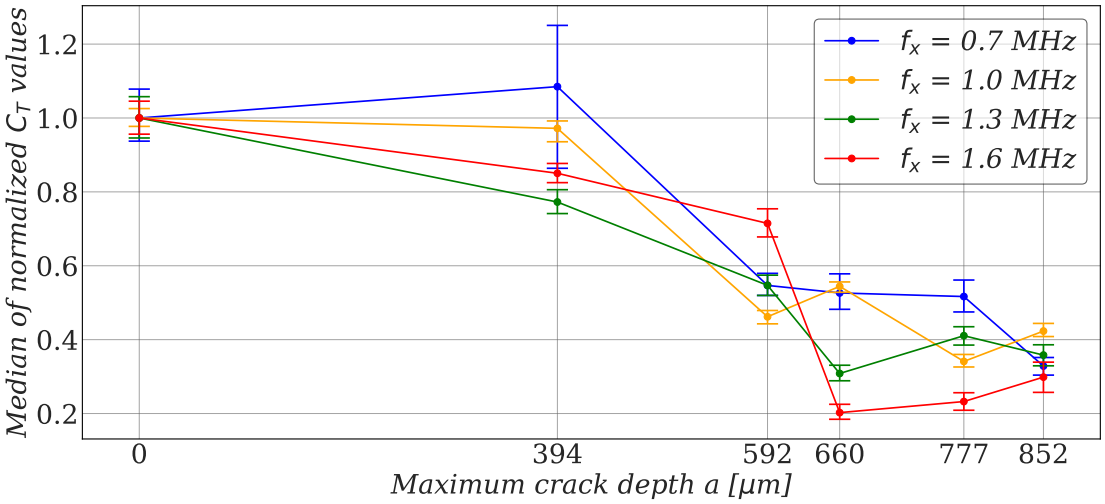

Fig. 7.9: Medians of the experimentally determined transmission coefficient distributions plotted over maximum head check depth a for the investigated excitation frequencies f_x. The interquartile range (IQR) is indicated by horizontal lines.

For excitation frequencies $f_x = 0.7\,\text{MHz}$ and $f_x = 1.0\,\text{MHz}$, the transmission coefficient maintains near-constant values up to a crack depth $a = 394\,\mu\text{m}$. This is equivalent to a ratio of crack depth to wavelength $a/\lambda \approx 0.13$ for $f_x = 1.0\,\text{MHz}$ and wave velocity $c = 2980\,\text{m/s}$. For these low excitation frequencies, the transmission coefficient starts to decrease substantially from $a = 394\,\mu\text{m}$ to $a = 592\,\mu\text{m}$. For larger values of a, a non-monotonic descending trend is observed in the medians.

For higher excitation frequencies, such as $f_x = 1.3\,\text{MHz}$ and $f_x = 1.6\,\text{MHz}$, there is a consistent decrease in the transmission coefficient, even for low a. At $a = 394\,\mu\text{m}$, the transmission coefficients at these frequencies deviate significantly from the undamaged specimen's transmission coefficients. Consequently, it is concluded that the transmission coefficient of higher f_x is more sensitive to lower crack depths a. This aligns with the studied literature, as surface waves with high f_x have a low λ. A rapid decline of the transmission coefficient is observed as a increases from $592\,\mu\text{m}$ to $660\,\mu\text{m}$, particularly at $f_x = 1.6\,\text{MHz}$. For $a > 660\,\mu\text{m}$, there is a slight tendency for the medians of the high-frequency transmission coefficients to increase.

However, the transmission coefficients obtained at $f_x = 1.6\,\text{MHz}$ deviates partially from the expected trend. From $a = 394\,\mu\text{m}$ to $a = 594\,\mu\text{m}$, a minor decrease is observed, even though a significant decrease is expected based on the theoretical solution [35]. Moreover, the reason behind the transmission coefficient leaning towards an increasing trend for $a > 660\,\mu\text{m}$ cannot be explained.

In previous studies, the effect of varying head check arrangements on C_T was explored using elastodynamic finite integration technique (EFIT) simulations. The impact of the number of head checks, referred to as k_S, was investigated in [3]. Specifically, the influence of the number of head

checks k_S was examined by simulating the transmission coefficient for $k_S = 1$ and $k_S = 3$ at two different ratios of crack depth a to wavelength λ. For comparison with the measurement results of this thesis, the ratio a/λ from the simulation was multiplied with the λ_x corresponding to a certain f_x to obtain the maximum crack depth a. Figure 7.10 compares the results obtained in [3] with the transmission coefficient values observed during the measurement. The simulated transmission coefficients, indicated by blue and orange dots for $k_S = 1$ and $k_S = 3$ respectively, are included for reference. Exponential functions were employed to fit the simulation results. The experimentally determined transmission coefficient distributions are characterized by their median and their IQR. The number of cracks k in each rail sample is provided in the top line of each diagram. Regions featuring different k values are separated by dashed vertical lines.

Overall, the measured transmission coefficients align well with the simulations. The simulation model presented in [3] is based on open cracks, whereas actual head checks are partially closed cracks. Therefore, it is expected that the measured transmission coefficients will exceed the simulated ones. This expectation is confirmed upon comparing the results from the simulation and the measurement, as shown in Figure 7.10. For the sample with $k = 1$, the medians of all transmission coefficients are greater than the simulated reference curve for $k_S = 1$. As both a and k increase, the measured transmission coefficients decrease. However, in most cases, the medians of the experimentally determined transmission coefficients remain above the simulated reference curve for $k_S = 3$. This corroborates the results obtained by measurement.

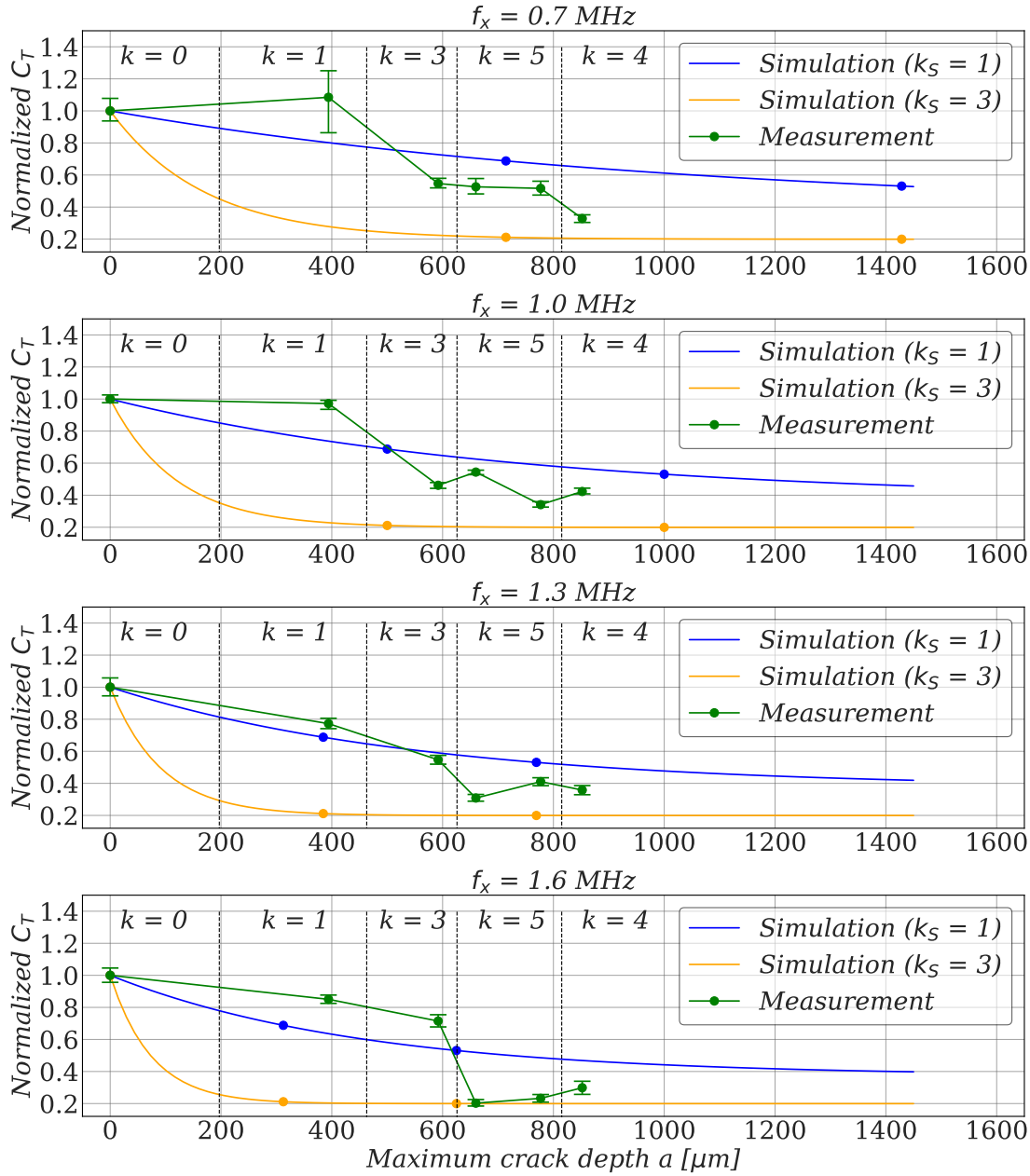

Fig. 7.10: Comparison of measured transmission coefficients with results from simulation in [3]. The simulated transmission coefficients are indicated by blue and orange dots for $k_S = 1$ and $k_S = 3$, respectively. Exponential functions were employed to fit the simulation results. The experimentally determined transmission coefficient distributions are characterized by their median and their IQR. The number of cracks k in each rail sample is provided in the top line of each diagram. Regions featuring different k values are separated by dashed vertical lines.

Up to this point, Figure 7.9 and 7.10 have only shown the medians and the IQRs of the transmission coefficients. In contrast, the distributions of observed values are displayed in Figure 7.11. Horizontal lines indicate the minimum and maximum of these distributions, while the median is depicted as a white dot. Moreover, the IQR is represented by thick vertical lines.

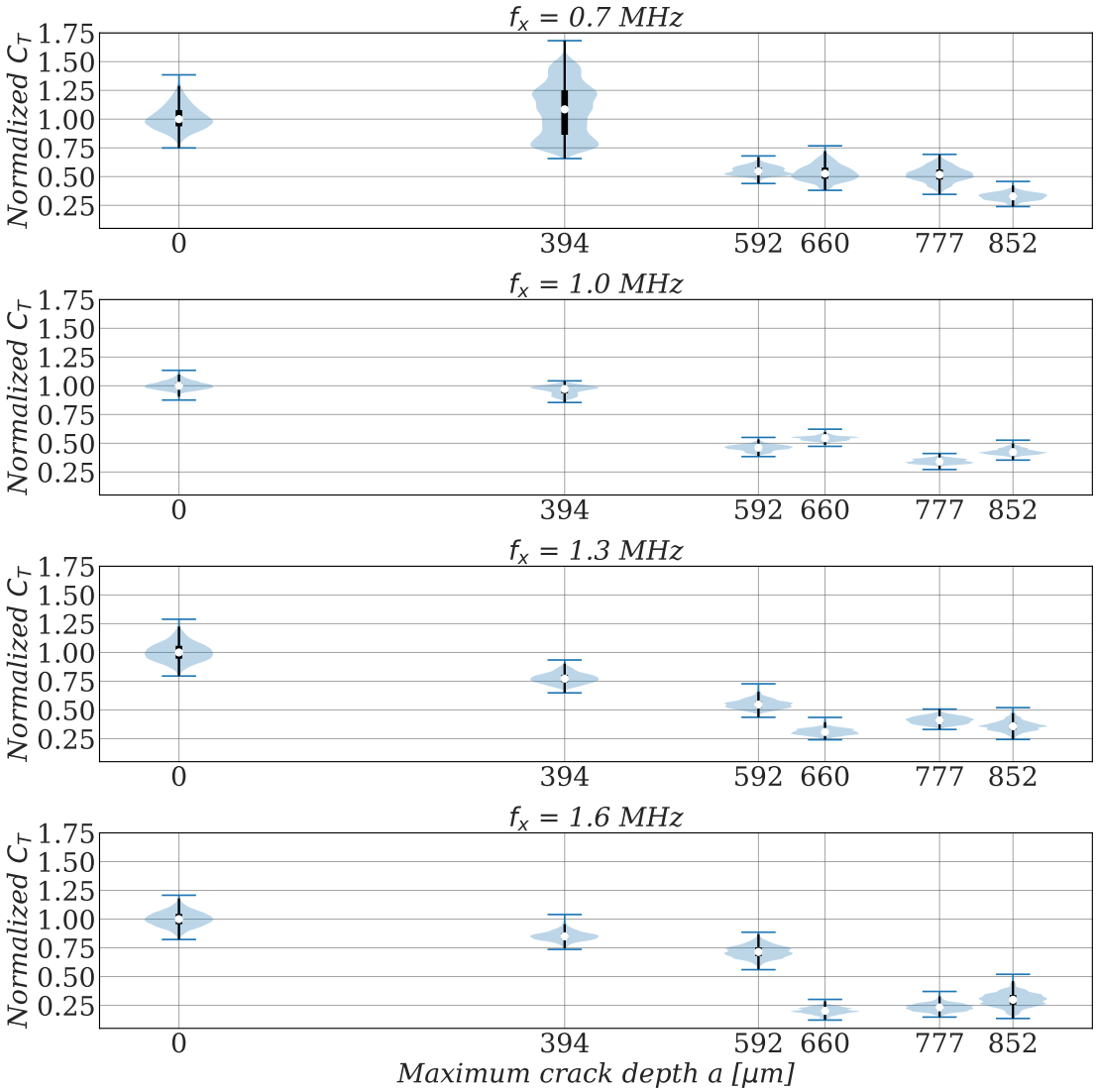

Fig. 7.11: Violin plots of the normalized transmission coefficients. The shown silhouettes represent the distributions of observed values of the transmission coefficient. Horizontal lines indicate the minimum and maximum of these distributions, while the median is depicted as a white dot. Moreover, the IQR is represented by thick vertical lines. Different widths of the experimentally determined distributions were observed: The narrowest transmission coefficient distributions emerged for $f_x = 1.0\,\mathrm{MHz}$. The reason for the substantially increased range of C_T at $f_x = 0.7\,\mathrm{MHz}$ and $a = 394\,\mu\mathrm{m}$ still remains to be found.

Most experimentally determined transmission coefficients distributions are evidently non-Gaussian. Additionally, a significant portion of these distributions of observed values exhibits a sec-

ondary peak. One can observe a significant diversity in the distribution widths, and consequently in the corresponding standard deviations σ. Specifically, the transmission coefficient distributions for the undamaged specimen are noticeably wider compared to other distributions found for the same f_x. In general, the narrowest transmission coefficient distributions were found for $f_x = 1.0\,\mathrm{MHz}$. The experimentally determined transmission coefficient distribution for $f_x = 0.7\,\mathrm{MHz}$ and $a = 394\,\mu\mathrm{m}$ was multipeaked and particularly wide. An individual crack was noticed at the measurement location on the corresponding specimen, instead of a continuous head check band. It is worth repeating that the z position of the LDV was slightly varied during the measurements for a given f_x. Apparently, some wave paths were significantly affected by the presence of the crack, while others were only slightly impacted. This effect seems to be more pronounced for SAWs with a higher wavelength λ, such as those at $f_x = 0.7\,\mathrm{MHz}$. An explanation for this observation still remains to be found. Overall, the transmission coefficient distributions with the highest standard deviation were found for $f_x = 0.7\,\mathrm{MHz}$.

According to the theoretical solution for a single crack, a rapid decrease of C_T would be expected until $a/\lambda = 0.35$ [35]. This ratio corresponds to $a \approx 800\,\mu\mathrm{m}$ for $f_x = 1.3\,\mathrm{MHz}$ and to $a \approx 650\,\mu\mathrm{m}$ for $f_x = 1.6\,\mathrm{MHz}$. The measured transmission coefficients agree well with the expectations based on the theoretical solution for an ideal surface-breaking crack for these high f_x. The experimentally determined transmission coefficient distributions decline until $a = 660\,\mu\mathrm{m}$ for these frequencies. However, the medians tend to increase slightly for $a \geq 660\,\mu\mathrm{m}$, and the distribution width also rises. Therefore, these increasing medians have less statistical significance. In fact, for $a \geq 660\,\mu\mathrm{m}$, the observed transmission coefficient distributions are partially overlapping.

At lower excitation frequencies, such as $f_x = 0.7\,\mathrm{MHz}$ and $f_x = 1.0\,\mathrm{MHz}$, there is a deviation from the theoretical solution found in [35]. This is in contrast to the higher frequencies discussed. For $f_x = 1.0\,\mathrm{MHz}$, for instance, a steep decrease of the transmission coefficient until $a \approx 1040\,\mu\mathrm{m}$ would be expected. However, already for $a \geq 592\,\mu\mathrm{m}$, the clearly decreasing trend of the transmission coefficient stops, the experimentally determined distributions start to overlap, and only a slightly decreasing non-monotonous trend is observed. Moreover, the measured transmission coefficients at the highest maximum crack depth, $a = 852\,\mu\mathrm{m}$, show nearly consistent values for all excitation frequencies f_x. This crack depth corresponds to an $a/\lambda \approx 0.20$ for $f_x = 0.7\,\mathrm{MHz}$ and to an $a/\lambda \approx 0.46$ for $f_x = 1.6\,\mathrm{MHz}$. Contrary to the observation, a significant dependence of the transmission coefficient on the excitation frequency would be expected according to the analytically computed transmission coefficient, which is depicted in Figure 3.2(a). A possible explanation for these deviations from the theoretical trend might be the varying surface roughness on the rail head. The rail samples were obtained from different test runs with varying loading conditions at the rail/wheel test rig and from different production batches; thus, significant variations in surface roughness among the specimens cannot be ruled out.

At this stage, it should be recalled that as the maximum crack depth a increases, the number of cracks k also rises. For instance, k rises from $k = 1$ to $k = 3$ as a grows from $a = 394\,\mu$m to $a = 592\,\mu$m. Similarly, from $a = 592\,\mu$m to $a = 660\,\mu$m, k increases from $k = 3$ to $k = 5$. It is concluded that the transmission coefficients of low excitation frequencies, such as $f_x = 0.7\,$MHz and $f_x = 1.0\,$MHz, are heavily influenced by overlapping head checks, as these transmission coefficients decline substantially with k rising from $k = 1$ to $k = 3$. As seen in Figure 7.11, these excitation frequencies would only offer the potential for a qualitative assessment of head check damage. For $a \geq 592\,\mu$m, the experimentally determined transmission coefficient distributions at $f_x = 0.7\,$MHz and $f_x = 1.0\,$MHz deviate substantially from the transmission coefficients for $a \leq 394\,\mu$m. Visually speaking, the transmission coefficient appears to follow a descending step function between these crack depths. Consequently, $f_x = 0.7\,$MHz and $f_x = 1.0\,$MHz do neither offer the potential for quantitative crack sizing nor can these f_x be employed for the detection of head checks with small crack depth.

For high excitation frequencies, such as $f_x = 1.3\,$MHz and $f_x = 1.6\,$MHz, a steadily decreasing trend of the transmission coefficient until $a = 592\,\mu$m is observed. This leads to the hypothesis of a linear relationship between maximum head check depth and transmission coefficient. In a first approximation, a linear regression analysis was performed, although, strictly speaking, the assumptions for the linear regression, such as normally distributed errors with constant variance, are violated. A simple linear function of the type

$$C_T = \beta_0 + \beta_1 a + \varepsilon \tag{7.2}$$

was used to model the suggested linear dependency of the transmission coefficient C_T on the maximum crack depth a. The intercept and the slope of the model function are denoted by β_0 and β_1, respectively. ε is the random error of a specific measurement [65]. The results from the linear regression analysis of the transmission coefficients at $f_x = 1.3\,$MHz and $f_x = 1.6\,$MHz are depicted in Figure 7.12. In addition to the regression lines, both the 95% confidence intervals on the regression lines' means and the 95% confidence intervals for a single observation, commonly termed prediction interval, are illustrated. Due to the large number of samples $n = 49200$ for both f_x, the 95% confidence intervals for the means nearly coincide with the regression lines. The computation of these ordinary least squares fits was performed with the *statsmodels* module [74] in *Python*. From a data-driven perspective, a different model function, such as a quadratic polynomial, may provide a better fit to the data. Nevertheless, the linear regression approach was preferred, as the theoretically computed SAW transmission coefficient at an ideal surface crack decreases almost linearly with increasing crack depth a within the corresponding range of a/λ [35].

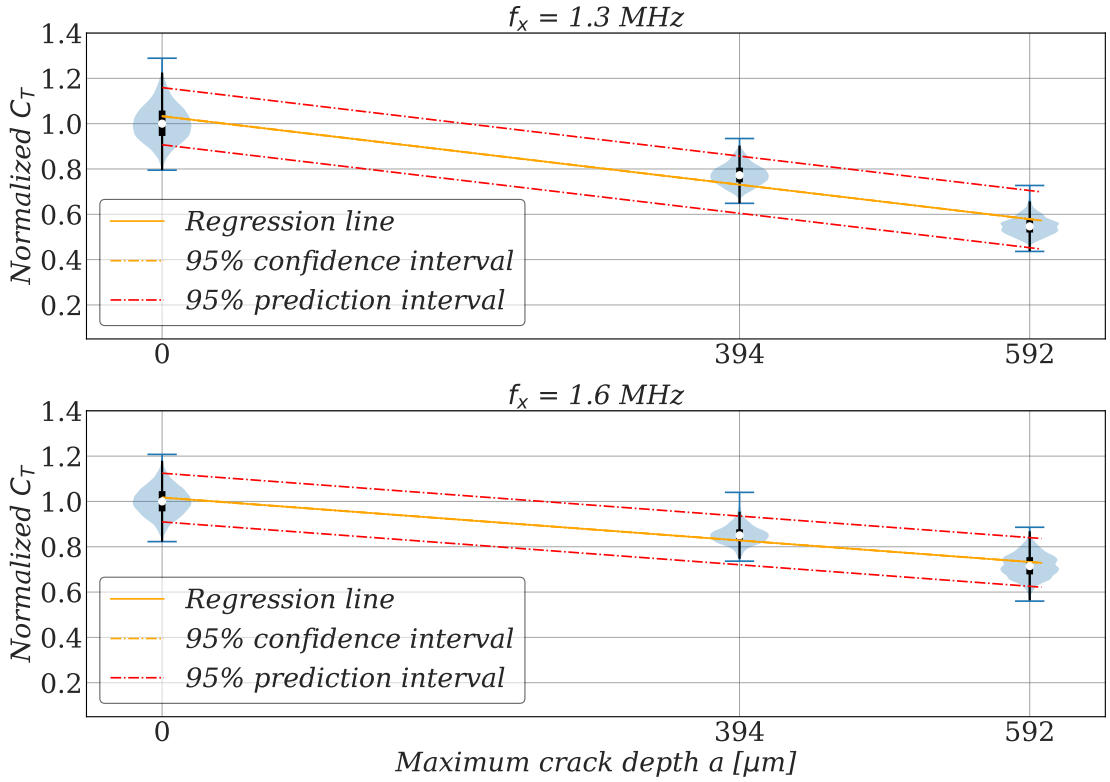

Fig. 7.12: Regression line fitted to the experimentally determined distributions of the transmission coefficients at $f_x = 1.3\,\text{MHz}$ and $f_x = 1.6\,\text{MHz}$. Only the transmission coefficients for $a \leq 592\,\mu\text{m}$ were taken into account. The 95% confidence interval does not deviate visibly from the regression line. Additionally, the 95% prediction interval is displayed.

The 95% confidence interval on the slope β_1 of the computed regression line for the excitation frequency $f_x = 1.3\,\text{MHz}$ is

$$-7.699 \times 10^{-4}\mu m^{-1} \leq \beta_1 \leq -7.646 \times 10^{-4}\mu m^{-1}.$$

At $f_x = 1.6\,\text{MHz}$, the 95% confidence interval on β_1 is given by

$$-4.825 \times 10^{-4}\mu m^{-1} \leq \beta_1 \leq -4.780 \times 10^{-4}\mu m^{-1}.$$

These intervals suggest that the regression line is gradually but significantly decreasing for both excitation frequencies. Due to this gentle slope and the wide 95% prediction interval, the maximum crack depth a cannot be determined precisely with a single measurement of the transmission coefficient. Nevertheless, a permanent installation of the piezoelectric transducers on the rail would facilitate the execution of multiple measurements in a short time. According to the law of large numbers, the uncertainty of the sample mean decreases as the number of measurements increases [73]. Therefore, measuring the transmission coefficient several times and taking the mean from these samples would theoretically offer the chance for a more precise determination of a.

Ultimately, additional laboratory experiments on rail samples with $a < 592\,\mu$m are required to prove the anticipated linear relationship between the maximum head check depth and the transmission coefficients of high excitation frequencies for $a \leq 592\,\mu$m. For values of a that exceed $a > 660\,\mu$m, it appears that a quantitative determination of a is not feasible even with the excitation frequencies $f_x = 1.3\,$MHz or $f_x = 1.6\,$MHz. This is due to the absence of a clear trend in the measured transmission coefficients.

To conclude, two potential effects that impede a quantitative assessment of high crack depths have been identified:

1. **Overlapping head checks**: After reaching a certain length, head checks start to overlap. With multiple head checks overlapping, the SAW transmission coefficient is significantly influenced by the number of cracks k. Thus, for high crack depths, a precise quantitative prediction of the maximum crack depth seems infeasible without knowing the actual number of overlapping head checks.
2. **Varying surface roughness**: A variation of the surface roughness on the rail head from one specimen to another cannot be excluded, as the samples stem from different experiments on the rail/wheel test rig. Since SAWs propagate in the near-surface area, their amplitude is very sensitive to the surface roughness. However, with regard to an in-track application, this issue is considered minor, as the surface roughness on the rail head of a given cross-section does not change significantly after some initial vehicle crossings.

These effects inhibit quantitative crack sizing altogether for $f_x = 0.7\,$MHz and $f_x = 1.0\,$MHz. Based on the experimentally determined distributions of the transmission coefficients at $f_x = 1.3\,$MHz and $f_x = 1.6\,$MHz, a quantitative assessment of the head check crack depth a is potentially feasible for depths up to $a = 590\,\mu$m. However, additional laboratory experiments are necessary to confirm this assumption. Severe head check damage with depths above $a = 660\,\mu$m can only be detected qualitatively with the employed setup.

Chapter 8
Summary, Conclusion and Future Work

In this thesis, a systematic approach has been adopted to investigate the correlation between the surface acoustic wave (SAW) transmission coefficient and the head check depth. Potential systematic measurement errors, inherent to the experimental setup, were thoroughly examined. The research conducted in this thesis has confirmed the previously observed qualitative impact of head checks on the SAW transmission coefficient. Additionally, the effects of various excitation frequencies were evaluated. It was found that the SAW transmission coefficient does not allow for a precise sizing of head checks with high crack depths. This is due to the unfavorable combination of the complex crack configuration and the undefined surface roughness of the rail. In particular, the fact that head checks start to overlap after reaching a certain length complicates a precise prediction of crack depth. Nonetheless, based on the results from this study, a quantitative assessment of the head check crack depth a with the SAW transmission coefficient seems potentially feasible up to a crack depth of $a = 590\,\mu$m with certain SAW excitation frequencies f_x, such as $f_x = 1.3\,$MHz and $f_x = 1.6\,$MHz. However, additional laboratory experiments are necessary to prove this hypothesis.

Ultimately, the undefined surface roughness could be addressed by adopting an approach that does not rely on the wave's amplitude. Possible alternative procedures could be based on non-linear ultrasonic characteristics, for example, which potentially enable the detection of surface cracks at an early stage. A model-based approach to signal processing promises the highest potential for accurate crack sizing. This approach could be based on a finite element model, for instance. Still, it remains an open question whether these methodologies facilitate a quantitative crack depth assessment given the complex crack configurations of head checks.

For the deployment within tracks, numerous challenges related to the measurement equipment must be overcome given the prevailing harsh environment. A signal generation and measurement device specifically designed for in-track implementation is required to drive the piezoelectric transducers. Investigations into the aging of the used adhesive have to be conducted, and methods to assess its condition have to be developed. For example, gauging the reflections of bulk waves could offer a possible approach for examining the condition of the adhesive, as the amplitude of

bulk waves does not degrade with rail head damage. Additionally, robust housings for the transducers need to be designed.

The insights from this thesis and the non-destructive testing method using SAWs have wider applications. Beyond railways, the SAW transmission coefficient is promising for assessing cracks in mechanical components with well-defined surfaces, like wheelset axles or turbine blades. This technique allows for scanning large areas with a single measurement. Furthermore, this thesis has demonstrated the capability of surface acoustic waves to detect surface breaking cracks at an early stage.

List of Figures

List of Tables

References

[1] R. Lewis and U. Olofsson, eds. *Wheel-rail interface handbook*. Woodhead publishing in mechanical engineering. Boca Raton, Fla. and Oxford u. a.: CRC Press and Woodhead, 2009. ISBN: 978-1-84569-412-8.

[2] Eric Magel et al. "Rolling contact fatigue, wear and broken rail derailments". In: *Wear* 366-367 (2016), pp. 249–257. ISSN: 00431648. DOI: 10.1016/j.wear.2016.06.009.

[3] Claudia Gruber et al. "Use of Surface Acoustic Waves for Crack Detection on Railway Track Components—Laboratory Tests". In: *Applied Sciences* 12.13 (2022), p. 6334. DOI: 10.3390/app12136334.

[4] René Heyder and Marcel Brehmer. "Empirical studies of head check propagation on the DB network". In: *Wear* 314.1 (2014). Proceedings of the 9th International Conference on Contact Mechanics and Wear of Rail / Wheel Systems, Chengdu, 2012, pp. 36–43. ISSN: 0043-1648. DOI: https://doi.org/10.1016/j.wear.2013.11.035.

[5] R.W. Ngigi et al. "Modern techniques for condition monitoring of railway vehicle dynamics". In: *Journal of Physics: Conference Series* 364 (May 2012). DOI: 10.1088/1742-6596/364/1/012016.

[6] Fan Yichao. *Analysis of surface defects using the ultrasonic Rayleigh surface wave: A step towards an accurate, fast and reliable NDT technique for surface defects*. Saarbrücken: VDM Verlag Dr. Müller, 2009. ISBN: 978-3-639-17460-1.

[7] Roberto Longo et al. "A method for crack sizing using Laser Doppler Vibrometer measurements of Surface Acoustic Waves". In: *Ultrasonics* 50.1 (2010), pp. 76–80.

[8] Bernard Masserey and Edoardo Mazza. "Ultrasonic sizing of short surface cracks". In: *Ultrasonics* 46.3 (2007), pp. 195–204.

[9] Josef Krautkrämer and Herbert Krautkrämer. *Werkstoffprüfung mit Ultraschall*. Berlin [u.a.] : Springer, 1961. URL: https://permalink.obvsg.at/mul/AC06631797.

[10] Australian Rail Track Corporation LTD. *Rail Defects Handbook: Engineering Practices Manual Civil Engineering*. 2006. URL: https://extranet.artc.com.au/docs/eng/track-civil/guidelines/rail/RC2400.pdf (visited on 09/08/2023).

[11] Xiangyu Duan et al. "Estimating the Axial Load of In-Service Continuously Welded Rail Under the Influences of Rail Wear and Temperature". In: *IEEE Access* PP (Oct. 2019), pp. 1–1. DOI: 10.1109/ACCESS.2019.2945609.

[12] Anika Dey, Hans-Martin Thomas, and Rainer Pohl. "The important role of eddy current testing in railway track maintenance". In: *17th World Conference on Non-Destructive Testing (Proceedings)*. Paper 393. International Committee for Non-Destructive Testing. 2008, pp. 1–4.

[13] Milica Mićić et al. “Inspection of RCF rail defects – Review of NDT methods”. In: *Mechanical Systems and Signal Processing* 182 (2023), p. 109568. ISSN: 08883270. DOI: 10.1016/j.ymssp.2022.109568.

[14] Hans-Jürgen Bargel and Günter Schulze. *Werkstoffkunde*. Berlin, Heidelberg: Springer Berlin Heidelberg, 2012. ISBN: 978-3-642-17716-3. DOI: 10.1007/978-3-642-17717-0.

[15] Sandeep Kumar Dwivedi, Manish Vishwakarma, and Prof.Akhilesh Soni. “Advances and Researches on Non Destructive Testing: A Review”. In: *Materials Today: Proceedings* 5.2 (2018), pp. 3690–3698. ISSN: 22147853. DOI: 10.1016/j.matpr.2017.11.620.

[16] Jingmang Xu et al. “Study on acoustic emission properties and crack growth rate identification of rail steels under different fatigue loading conditions”. In: *International Journal of Fatigue* 172 (2023), p. 107638. ISSN: 01421123. DOI: 10.1016/j.ijfatigue.2023.107638.

[17] Christoph Tuschl, Beate Oswald-Tranta, and Sven Eck. “Inductive Thermography as Non-Destructive Testing for Railway Rails”. In: *Applied Sciences* 11.3 (2021), p. 1003. DOI: 10.3390/app11031003.

[18] Peng Xu et al. “Study on high-speed rail defect detection methods based on ECT, MFL testing and ACFM”. In: *Measurement* 206 (2023), p. 112213. ISSN: 02632241. DOI: 10.1016/j.measurement.2022.112213.

[19] Volker Deutsch, Michael Platte, and Manfred Vogt. *Ultraschallprüfung: Grundlagen und industrielle Anwendungen*. Berlin: Springer, 1997. ISBN: 3-540-62072-9.

[20] KARL DEUTSCH Pruef- und Messgeraetebau GmbH + Co KG. *Basic Knowledge about Ultrasonic Testing*. URL: https://www.karldeutsch.de/ndt-knowledge/basic-knowledge/basic-knowledge-about-ultrasonic-testing/?lang=en#toggle-id-1-closed (visited on 09/04/2023).

[21] Arash Amini et al. “Wayside detection of faults in railway axle bearings using time spectral kurtosis analysis on high frequency acoustic emission signals”. In: *Advances in Mechanical Engineering* 8 (Nov. 2016). DOI: 10.1177/1687814016676000.

[22] Plasser & Theurer, Export von Bahnbaumaschinen, Gesellschaft m.b.H. *Measuring work: Measuring technology*. URL: https://www.plassertheurer.com/en/machine/measuring-work/overview (visited on 09/05/2023).

[23] Vossloh AG. *Rail Monitoring*. 2023. URL: https://www.vossloh.com/de/produkte-und-loesungen/produktfinder/produkt_21188.php (visited on 05/09/2023).

[24] RailTechnology GmbH. *RM-RDD (ACFM) Rail Defect Detection: Rail Surface crack detection trolley based on ACFM technology*. URL: https://www.railmeasurement.com/rm-rdd-rail-defect-detection/ (visited on 09/05/2023).

[25] D-RAIL. *PREDICTIVE RAILWAY MAINTENANCE: REAL TIME INFRASTRUCTURE MONITORING*. 2021. URL: https://www.d-rail.com/ (visited on 09/05/2023).

[26] voestalpine Railway Systems GmbH. *Diagnostic & Monitoring Technologies for Infrastructure*. 2023. URL: https://www.voestalpine.com/railway-systems/en/products/diagnostic-and-monitoring-infrastructure/ (visited on 09/07/2023).

[27] Joseph L. Rose. *Ultrasonic guided waves in solid media*. New York, NY: Cambridge University Press, 2014. ISBN: 978-1-107-04895-9. DOI: 10.1017/CBO9781107273610.

[28] I. A. Viktorov. *Rayleigh and Lamb waves: Physical theory and applications*. Ultrasonic technology. New York: Springer Science + Business Media, 2013. ISBN: 978-1-4899-5683-5.

[29] Bernard Masserey. "Ultrasonic surface crack characterization using Rayleigh waves". PhD thesis. ETH Zurich, 2006. DOI: 10.3929/ETHZ-A-005207086.

[30] Simon Jones. "Ground Vibration from Underground Railways: How Simplifying Assumptions Limit Prediction Accuracy". PhD thesis. University of Cambridge, 2010. DOI: 10.17863/CAM.13982.

[31] Masahiko Hirao, Yosuke Miura, and Hidekazu Fukuoka. "Reflection and Transmission of Rayleigh Surface Wave at a Surface Crack". In: *Japanese Journal of Applied Physics* 21.S3 (1982), p. 45. ISSN: 0021-4922. DOI: 10.7567/JJAPS.21S3.45.

[32] Lei Xu et al. "Model-driven fatigue crack characterization and growth prediction: A two-step, 3-D fatigue damage modeling framework for structural health monitoring". In: *International Journal of Mechanical Sciences* 195 (2021), p. 106226. ISSN: 00207403. DOI: 10.1016/j.ijmecsci.2020.106226.

[33] Kyung-Young Jhang et al., eds. *Measurement of nonlinear ultrasonic characteristics*. Springer eBook Collection. Singapore: Springer Nature Singapore and Imprint Springer, 2020. ISBN: 978-981-15-1460-9. DOI: 10.1007/978-981-15-1461-6.

[34] Tribikram Kundu. *Mechanics of elastic waves and ultrasonic nondestructive evaluation*. First edition. Boca Raton, London, and New York: CRC Press/Taylor & Francis Group, 2019. ISBN: 978-1-138-03594-2.

[35] Y. C. Angel and J. D. Achenbach. "Reflection and transmission of obliquely incident Rayleigh waves by a surface-breaking crack". In: *The Journal of the Acoustical Society of America* 75.2 (1984), pp. 313–319. ISSN: 0001-4966. DOI: 10.1121/1.390473.

[36] Tribikram Kundu, ed. *Nonlinear Ultrasonic and Vibro-Acoustical Techniques for Nondestructive Evaluation*. Springer eBook Collection. Cham: Springer International Publishing, 2019. ISBN: 978-3-319-94474-6. DOI: 10.1007/978-3-319-94476-0.

[37] Daniel T. Zeitvogel et al. "Characterization of stress corrosion cracking in carbon steel using nonlinear Rayleigh surface waves". In: *NDT & E International* 62 (2014), pp. 144–152. ISSN: 09638695. DOI: 10.1016/j.ndteint.2013.12.005.

[38] B. P. Lathi and Roger A. Green. *Essentials of Digital Signal Processing*. Cambridge et al.: Cambridge University Press, 2014. ISBN: 978-1-107-05932-0.

[39] Alan V. Oppenheim, John R. Buck, and Ronald W. Schafer. *Discrete-time signal processing*. 2. ed., internat. ed. Prentice Hall signal processing series. Upper Saddle River, NJ: Prentice-Hall Internat, 1999. ISBN: 0-13-754920-2.

[40] Richard G. Lyons. *Understanding digital signal processing*. 2nd ed. Upper Saddle River, NJ: Prentice Hall PTR, 2004. ISBN: 0-13-108989-7.

[41] N. Deichmann. *Einführung in die Zeitreihenanalyse*. Zürich, 2012. URL: https://n.ethz.ch/~deichman/skript1.pdf.

[42] Martin Werner. *Digitale Signalverarbeitung mit MATLAB: Grundkurs mit 16 ausführlichen Versuchen ; mit 76 Tabellen ; [mit Online-Service*. 5., durchges. und aktualisierte Aufl. Studium Nachrichtentechnik. Wiesbaden: Vieweg + Teubner, 2012. ISBN: 3834814733.

[43] James V. Candy. *Model-based signal processing*. Adaptive and learning systems for signal processing, communications, and control. Hoboken, N.J: IEEE Press, 2010. ISBN: 978-0-471-23632-0.

[44] Frank R. Kschischang. *The Hilbert Transform*. Toronto, 2015. URL: https://www.comm.utoronto.ca/~frank/notes/hilbert.pdf.

[45] Florian Bleibinhaus. *Signal Processing*. Leoben, 2022.

[46] Martin Meyer. *Signalverarbeitung: Analoge und digitale Signale, Systeme und Filter ; mit 20 Tabellen*. 4., überarb. und aktualisierte Aufl. Studium Technik. Wiesbaden: Vieweg, 2006. ISBN: 3834802433.

[47] James V. Candy. *Signal processing: The model-based approach*. McGraw-Hill series in electrical engineering Communications and signal processing. New York, NY: McGraw-Hill, 1986. ISBN: 978-0070097254.

[48] Christian Dürager. "Model-Based Damage Featrue Extraction For Structural-Health Monitoring Applications". Dissertation. Saarbrücken: Universitat des Saarlandes, 2018.

[49] Donald W. Marquardt. "An Algorithm for Least-Squares Estimation of Nonlinear Parameters". In: *Journal of the Society for Industrial and Applied Mathematics* 11.2 (1963), pp. 431–441. ISSN: 0368-4245. DOI: 10.1137/0111030.

[50] Julius O. Smith. *Introduction to digital filters: with audio applications*. 2. print. W3K Publishing, 2008. ISBN: 978-0974560717. URL: https://www.dsprelated.com/freebooks/filters/.

[51] F. Gustafsson. "Determining the initial states in forward-backward filtering". In: *IEEE Transactions on Signal Processing* 44.4 (1996), pp. 988–992. DOI: 10.1109/78.492552.

[52] C Ziomek and P Corredoura. "Digital i/q demodulator". In: *Proceedings Particle Accelerator Conference*. Vol. 4. IEEE. 1995, pp. 2663–2665.

[53] Ignasi Corbella et al. “A Novel Digital IQ Demodulation for Interferometric Radiometers”. In: *Remote Sensing* 13.6 (2021), p. 1156.

[54] Digilent Inc. *Analog Discovery 2: 100MS/s USB Oscilloscope, Logic Analyzer and Variable Power Supply*. 2023. URL: https://digilent.com/shop/analog-discovery-2-100ms-s-usb-oscilloscope-logic-analyzer-and-variable-power-supply/ (visited on 09/21/2023).

[55] Reinhard Klambauer and Maximilian Kiss. *TOF-Messbox Manual*. Sept. 21, 2023.

[56] William N. Sharpe, ed. *Springer handbook of experimental solid mechanics: With 50 tables*. Springer handbooks. New York: Springer, 2008. ISBN: 978-0-387-26883-5.

[57] PI Ceramic GmbH. *Piezoelektrische Aktoren: BAUELEMENTE , TECHNOLOGIE , ANSTEUERUNG*. URL: https://www.piceramic.de/fileadmin/user_upload/pi_ceramic/files/catalog_CAT/PI_CAT125D_R2_Piezokeramische_Materialien_und_Bauelemente.pdf (visited on 09/21/2023).

[58] Hottinger Brüel & Kjaer GmbH. *Z70: Cold Curing Superglue for Experimental Tests, and for Sensors Without High Accuracy Requirements*. URL: https://www.hbm.com/en/2962/z70-a-single-component-cold-curing-adhesive/ (visited on 09/27/2023).

[59] Kun Chen et al. “Laser-Generated Surface Acoustic Wave Technique for Crack Monitoring – A Review”. In: *International Journal of Automation Technology* 7.2 (2013), pp. 211–220. ISSN: 1881-7629. DOI: 10.20965/ijat.2013.p0211.

[60] Faeez Masurkar, Javad Rostami, and Peter Tse. “Design of an innovative and self-adaptive-smart algorithm to investigate the structural integrity of a rail track using Rayleigh waves emitted and sensed by a fully non-contact laser transduction system”. In: *Applied Acoustics* 166 (2020), p. 107354. ISSN: 0003682X. DOI: 10.1016/j.apacoust.2020.107354.

[61] Herbert A. Sturges. “The Choice of a Class Interval”. In: *Journal of the American Statistical Association* 21.153 (1926), pp. 65–66. ISSN: 0162-1459. DOI: 10.1080/01621459.1926.10502161.

[62] Alexander M. Mood, Franklin A. Graybill, and Duane C. Boes. *Introduction to the theory of statistics*. 3. ed., international student ed. McGraw-Hill international editions Statistics series. Tokyo and Düsseldorf: McGraw-Hill, 1974. ISBN: 0-07-042864-6.

[63] Jerrold H. Zar. *Biostatistical analysis*. 5. ed. Upper Saddle River, NJ: Prentice Hall, 2010. ISBN: 978-0-13-100846-5.

[64] Gregory W. Corder and Dale I. Foreman. *Nonparametric statistics: A step-by-step approach*. 2. ed. Hoboken, New Jersey: Wiley, 2014. ISBN: 978-1-118-84031-3.

[65] Douglas C. Montgomery, Elizabeth A. Peck, and G. Geoffrey Vining. *Introduction to Linear Regression Analysis*. 5. ed. Wiley series in probability and statistics. Hoboken, NJ: Wiley, 2012. ISBN: 978-0-470-54281-1.

[66] Norbert Gaffke. *Kurzskript zur Vorlesung "Schätzen und Testen": Lineare Regression*. 2011.

[67] Roland Schmidt. "Future Distributed Geomonitoring - Analysis Methods, Algorithms & Technologies". PhD thesis. Montanuniversitaet Leoben, Department Product Engineering, Chair of Automation, 2020.

[68] voestalpine Railway Systems GmbH. *60E1 (UIC60, SBBVI): Vignolschienen, Flat Bottom Rails*. URL: https://www.voestalpine.com/highperformancemetals/argentina/app/uploads/sites/23/2019/08/voestalpine-60E1.pdf (visited on 10/11/2023).

[69] R. Stock and R. Pippan. "Rail grade dependent damage behaviour – Characteristics and damage formation hypothesis". In: *Wear* 314.1-2 (2014), pp. 44–50. ISSN: 00431648. DOI: 10.1016/j.wear.2013.11.029.

[70] Brian R. Martin. *Statistics for physical sciences: An introduction*. 1. ed. Waltham, Mass., Amsterdam, and Heidelberg: Academic Press and Elsevier, 2012.

[71] Eloísa Díaz-Francés and Francisco J. Rubio. "On the existence of a normal approximation to the distribution of the ratio of two independent normal random variables". In: *Statistical Papers* 54.2 (2013), pp. 309–323. ISSN: 0932-5026. DOI: 10.1007/s00362-012-0429-2.

[72] Jack Hayya, Donald Armstrong, and Nicolas Gressis. "A Note on the Ratio of Two Normally Distributed Variables". In: *Management Science* 21.11 (1975), pp. 1338–1341. ISSN: 0025-1909. DOI: 10.1287/mnsc.21.11.1338.

[73] Ludwig Fahrmeir et al. *Statistik: Der Weg zur Datenanalyse*. 5., verb. Aufl. Springer-Lehrbuch. Berlin and Heidelberg: Springer, 2004. ISBN: 3540212329.

[74] Skipper Seabold and Josef Perktold. "statsmodels: Econometric and statistical modeling with python". In: *9th Python in Science Conference*. 2010.